

POLITECNICO DI TORINO

Department of Electronics and Telecommunications

Master's Degree in Nanotechnologies for ICTs

Master's Degree Thesis

Realization of neuromorphic systems for the detection, transduction and classification of bio-electronic signals



Supervisor:

Prof. Cocuzza Matteo

Co-Supervisors:

Dr. Marasso Simone Luigi

Dr. Battistoni Silvia

Prof. Erokhin Victor

Candidate:

Ferrucci Luciano

Academic Year: 2021-2022

Abstract

This thesis work is the result of a partnership between ChiLab-Materials and Microsystems Laboratory (Politecnico di Torino) in Chivasso and the Institute of Materials for Electronics and Magnetism (IMEM) at the National Research Council (CNR) in Parma.

In the first part, the fabrication process was done, by realizing the devices through standard cleanroom procedures, such as metal deposition, etching and photolithography. The devices layout was improved, so that the total number of devices per single die passed from 8 to 16. Three different channel sizes were considered: the channel width was fixed to $250\ \mu\text{m}$, $500\ \mu\text{m}$ and $2000\ \mu\text{m}$ respectively, while the length was progressively varied ($10\ \mu\text{m}$, $50\ \mu\text{m}$, $100\ \mu\text{m}$ and $200\ \mu\text{m}$). This choice was important to evaluate the behaviour of memristors with different channel aspect ratio. After that, the attention was focused on the inkjet printing process, chosen for the deposition of the active material (PANI) on the devices channel. The inkjet printer used here relies on a piezoelectric actuation principle: the droplet ejection is obtained by stimulating the nozzle with a voltage signal. The process improvement included different aspects. Firstly, the ink synthesis was optimized. Different concentrations were investigated to improve both the printability and the conductive properties. At this point, the inkjet printer parameters were optimized, starting from the voltage signal waveform definition up to the spot parameters. The inkjet printing conditions varied according to the channels sizes and the pattern dimensions to be printed, since the polymeric ink quantity needed was different. Furthermore, important role was played by the final drying step of the printed pattern. Two solutions were considered: a short, fast drying procedure and a long, slow one. In the first case, the variability among the devices was greater, affecting negatively the final printed pattern, which showed a non-homogeneous and uniform volume. In the second case, instead, the variability among the devices was evidently reduced, with a much better volume uniformity and printed pattern repeatability.

In the second part of the activity, the electrical characterization of organic memristors was carried out at CNR-IMEM in Parma. The measurements were done in liquid electrolyte (HCl 1M), since the resistive switching mechanism of these devices is associated with the redox reaction. A comparison between short-dried and long-dried devices was proposed. In fact,

short-drying procedure impacted negatively on the performances, since the variability among devices with same channel aspect ratio was evident. On the opposite, long-drying procedure lead to much better results, with much less variability and more repeatability for twin devices. The electrical characterization tests included the analysis of the hysteresis curves at different working frequency (scan rate), followed by the extraction of the minimum and maximum values of conductance. In the best cases, these devices showed a stable behaviour, with a constant gap separating minimum and maximum conduction values. The geometry factor of devices channels is relevant here, since channel conduction is directly proportional with the channel aspect ratio. To show the dependence of the resistance on applied voltage and time, the kinetics in voltage and time were investigated. The synaptic weight variation was evaluated as function of the applied voltage pulse amplitude and time width. The higher and longer the pulse signal, the larger the synaptic weight variation, confirming the non-linear behaviour of these devices. To prove the reliability and stability of organic memristors, endurance tests were executed on the best performing devices (in both short and long dry procedure cases): the best devices are stable for 2000 writing cycles at least, promising for neuromorphic applications. Finally, neuromorphic properties in organic memristors were analysed, in particular Long-Term Potentiation (LTP) and Long-Term Depression (LTD). Here, devices with different aspect ratio, for both drying procedures, were considered. In general, the results showed a good response: on the one hand, an increase of the synaptic weight variation with the increase of the number of positive voltage pulses (potentiation) was observed. On the other hand, the increase of the number of negative voltage pulses (depression) corresponded to a decrease of the synaptic weight variation.

Keywords: Inkjet printing, Organic memristors, PANI, Neuromorphic, Artificial Intelligence, Neural Networks, Bio-electronics

Contents

List of Figures	v
List of Tables	xi
1 Introduction	1
2 Memristors	3
2.1 Theoretical background	3
2.2 State of the art	6
2.2.1 Resistive memristors	8
2.2.2 Spintronic memristors	9
2.2.3 Ferroelectric memristors	10
2.2.4 Organic memristors	11
2.2.5 Applications	13
2.2.6 Introduction to PANI-based memristors	16
2.3 Inkjet printing technologies	20
2.3.1 Thermal actuation	21
2.3.2 Electrostatic actuation	22
2.3.3 Acoustic actuation	23
2.3.4 Piezoelectric actuation	23
2.3.5 Applications	24

2.4	Jet-Lab4 inkjet system	26
2.5	Inkjet printer settings	28
2.5.1	The back-pressure	28
2.5.2	The driving voltage signal waveform	30
2.5.3	Spot parameters	34
3	Materials and fabrication processes	35
3.1	Fabrication procedure	36
3.2	Inkjet printing optimization	38
3.2.1	The nozzle clogging: a resolute approach	38
3.2.2	Ink characterization and optimization	39
3.2.3	Devices layout and printing optimization	46
3.2.4	Morphological analysis	53
4	Results and discussion	56
4.1	Electrical characterization	57
4.1.1	Experimental setup	57
4.1.2	Hysteresis	59
4.1.3	Kinetics in voltage and time	70
4.1.4	Endurance	73
4.1.5	Neuromorphic properties: definitions	75
4.1.6	Neuromorphic properties: the synaptic weight variation	76
4.1.7	Neuromorphic properties: LTP and LTD	80
5	Conclusions and future perspectives	83
	References	86

List of Figures

2.1	The four fundamental two-terminal circuit elements [1].	4
2.2	On the left: i - v plot of an ideal memristor, where the hysteresis loop can be observed. The non-linear behaviour of such device is furtherly confirmed in the q - ϕ plot on the right [2].	6
2.3	HP memristor.	7
2.4	ECM mechanism. The red bubbles are the active metal atoms, the yellow ones are the electrolyte atoms and the grey ones the inert metal atoms. Adapted from [3].	8
2.5	PCM mechanism (TE=Top Electrode, BE=Bottom Electrode) [4].	9
2.6	MTJ working principle. In (A), the blue bubbles are the minority electrons (whose spin moment is opposite to the material magnetization) and the red ones are the majority electrons (whose spin moment is parallel to the material magnetization) that tunneled the oxide layer. Here the device is in a antiparallel configuration, a maximum resistance value is detected. Once the current overcomes the critical value, the switching occurs due to the spin transfer torque of spin-polarized majority electrons (B): the configuration becomes parallel and a minimum resistance value is detected. Adapted from [4].	10
2.7	Example of a ferroelectric memristor device. It has dual channels at the upper and lower sides of the ZnO layer, which are controlled separately by the top gate and the bottom gate, respectively. The bottom FET (Field-Effect Transistor) has the gate (SRO layer) and a ferroelectric layer constituting a FeFET (Ferroelectric FET) that shows a memory-like behaviour [5].	11
2.8	Pictures of the different resistive switching mechanisms for organic memristors [6].	13

2.9	The main memristors application fields.	13
2.10	Memristor synaptic bridge circuit [7].	14
2.11	Memristor crossbar array scheme: the white bars are metallic nanowires while the black cylinders correspond to memristive devices [8].	15
2.12	PANI redox and doping schemes [9].	16
2.13	Single layer perceptron scheme [10].	17
2.14	Double layer perceptron scheme: neurons are highlighted by circles and are characterized by differential summator and activation function. Enumeration of memristive links ($Mn_{ij}(+/-)$) includes the n -th layer, associated with the i -th input and the j -th output neurons. A sign defines whether this partial weight is positive or not [10].	18
2.15	Scheme of inkjet printing process executed on a patterned PDMS substrate. Adapted from [11].	20
2.16	Scheme of CIJ (on the left) and DOD Inkjet (on the right). Adapted from [12].	21
2.17	Thermal inkjet working principle [13].	22
2.18	Electrostatic inkjet scheme [14].	22
2.19	Acoustic inkjet scheme. Adapted from [15].	23
2.20	Piezoelectric inkjet printhead sketch [16].	24
2.21	Jetlab printing system picture, courtesy of [17].	27
2.22	Inkjet printer nozzle.	27
2.23	Droplet ejection from the nozzle, snapshot taken by the inkjet printer lateral camera.	28
2.24	Positive back-pressure result: a big droplet ejected from the nozzle, snapshot taken by the lateral camera.	29
2.25	Negative back-pressure working principle, sketch [17].	30
2.26	Plot of a unipolar signal waveform [18].	31
2.27	Plot of a bipolar signal waveform [18].	32
2.28	Satellites formation, snapshot taken by inkjet printer lateral camera.	32

2.29	Another example of a bipolar waveform signal.	33
2.30	Inkjet printed drops on substrate, highlighting the spot parameters. Adapted from [11].	34
3.1	Scheme of the device fabrication process.	37
3.2	On the left, 5x5 inch (1 inch=25.4 mm) UV mask of one of the geometries of interest, snapshot taken by CleWin software. On the right, a zoom on a single die. The violet parts are the ones subjected to the laser writing process or, in other words, the ones to be removed during the development step.	37
3.3	Interdigitated devices used for the inkjet printing optimization, snapshot taken by CleWin software. The green rectangles are the patterns to be printed and the darker green ones refer to the gold electrodes.	40
3.4	The three signal waveforms used for the ink optimization tests. The black line refers to the signal used for 100 $\mu\text{g/ml}$ of ink concentration. The red and blue lines refer to 250 and 500 $\mu\text{g/ml}$ of ink concentration, respectively.	41
3.5	FESEM pictures of tested interdigitated devices, PANI ink concentration of 100 $\mu\text{g/ml}$. 5 printed layers. On the left, the single device. On the top-right, a zoom on the channel. On the bottom-right, PANI aggregate.	42
3.6	FESEM pictures of tested interdigitated devices, PANI ink concentration of 250 $\mu\text{g/ml}$. 5 printed layers. On the left, the single device. On the top-right, a zoom on the channel. On the bottom-right, PANI aggregate.	43
3.7	FESEM pictures of tested interdigitated devices, PANI ink concentration of 500 $\mu\text{g/ml}$, 2 printed layers. On the left, the single device. On the right, a zoom on the channel.	43
3.8	FESEM pictures of tested interdigitated devices, PANI ink concentration of 500 $\mu\text{g/ml}$, 5 printed layers. On the left, the single device. On the top-right, a zoom on the channel. On the bottom-right, PANI aggregate.	44
3.9	Resistance as function of the ink concentration. Inset plot of the same graph in semi logarithmic scale. The printed layers are 5 in all the three cases.	44
3.10	Resistance as function of number of the printed PANI layers. PANI ink concentration of 500 $\mu\text{g/ml}$	45

3.11	Devices layout of a single die, snapshot taken from CleWin software. The violet parts refer to gold electrodes, while the green ones refer to the inkjet printed pattern.	47
3.12	The final devices. Notice that, after the fabrication process steps, a additional spin-coated resist is deposited in order to prevent them from undesired damages. This is the reason why the devices show a red surface. Before inkjet printing, the resist must be removed by washing the dies with acetone and isopropanol. . . .	48
3.13	PANI ink droplets measurement from a rectangular array printed on paper. Picture taken from optical microscope.	49
3.14	Examples of bad results, because of not optimal choice of inkjet printer parameters. Pictures taken from optical microscope.	50
3.15	Plot of the voltage signals for inkjet printing of the final devices, compared with the one used for the ink optimization test (concentration of $500 \mu g/ml$). The red line refers to the signal used for $w250$; the blue one to $w500$; the dashed-dot green one to $w2000$ and the dashed black one to the ink optimization test. . . .	51
3.16	The best patterning results, after the inkjet printing optimization tests. Pictures taken from optical microscope.	52
3.17	Comparison between short and long dry procedures, $w2000$ geometry. Pictures taken from optical microscope.	53
3.18	Printed area as function of the channel aspect ratio, comparison between short dry procedure (in black) and long dry one (in red). The graph is reported in logarithmic scale.	54
4.1	Experimental setup of the electrical characterization tests.	58
4.2	Drain and Source contacts positions on the square metal pads (violet colour refers to gold). The green rectangles refer to <i>PDMS</i> chambers, while the blue ones refer to <i>HCl</i> . Snapshot adapted from CleWin software.	58
4.3	Example of a $I_{DS}-V_{DS}$ curve. Short dried device, $W \times L=250 \times 10$. Scan rate at 50 mV/s.	59
4.4	Example of a I_G-V_{DS} curve. Short dried device, $W \times L=250 \times 10$. Scan rate at 50 mV/s.	60

4.5	Example of a $I_{diff}-V_{DS}$ curve. Short dried device, $W \times L = 250 \times 10 \mu m$. Scan rate at 50 mV/s.	61
4.6	$W \times L = 250 \times 10 \mu m$. Scan rate at 200 mV/s.	62
4.7	Example of a $I_{diff}-V_{DS}$ curve at different scan rates. Short dried device, $W \times L = 250 \times 10 \mu m$	64
4.8	Example of a I_G-V_{DS} curve at different scan rates. Short dried device, $W \times L = 250 \times 10 \mu m$	64
4.9	Example of G_{min} and G_{max} at different scan rates. Short dried device, $W \times L = 250 \times 10 \mu m$	65
4.10	$I_{diff}-V_{DS}$ curves of devices with channel geometry $W \times L = 250 \times 10 \mu m$, at scan rate of 200 mV. Short dry procedure case.	66
4.11	G_{max} mean values extracted from the hysteresis curves, as function of the channel aspect ratio $\frac{W}{L}$. Short dry vs long dry procedure. Scan rate at 200 mV/s. Main graph in semi logarithmic scale, inset graph in logarithmic scale.	67
4.12	$I_{diff} - V_{DS}$ hysteresis curves, comparison among long dried devices.	68
4.13	G_{min} and G_{max} at different scan rates, comparison among long dried devices with the highest aspect ratio.	69
4.14	G_{min} and G_{max} at different scan rates, $W \times L = 10 \times 500 \mu m$ long vs short dry case.	69
4.15	Kinetics in voltage, V_{DS} pulses train signal plot.	70
4.16	Kinetics in voltage, example of I_{diff} plot. On the top-left side, a inset graph of the input V_{DS} pulses. Short dried device, $W \times L = 250 \times 10$	71
4.17	Kinetics in time.	72
4.18	Endurance test results: on the left-hand side, I_{ON} and I_{OFF} current contribution vs the number of writing cycles in semi logarithmic scale. On the right-hand side, I_{ON} and I_{OFF} normal distributions are reported.	74
4.19	Kinetics in voltage, $\frac{\Delta G}{G}$ vs V_{DS} pulse amplitude plot. Comparison among devices with same aspect ratio (in this case $W \times L = 500 \times 10 \mu m$).	76
4.20	Kinetics in voltage, $\frac{\Delta G}{G}$ vs V_{DS} pulse amplitude plot. Comparison among long dried devices.	78

4.21	Kinetics in time, $\frac{\Delta G}{G}$ vs V_{DS} pulse width plot. Comparison among shortly dried devices with same aspect ratio (in this case $W \times L = 500 \times 10 \mu m$).	79
4.22	Kinetics in time, $\frac{\Delta G}{G}$ vs V_{DS} pulse amplitude plot. Comparison among long dried devices. $V_{DS} = 0.7$ V.	79
4.23	V_{DS} pulses adopted for the measurements.	80
4.24	On the left-hand side, LTP plot comparing the performances of short dried devices. On the right-hand side, LTD plot of the same compared devices.	81
4.25	On the left-hand side, LTP plot comparing the performances of different devices. On the right-hand side, LTD plot of the same compared devices.	82

List of Tables

3.1	Inkjet printer parameters settings for the three tested ink concentrations.	40
3.2	Resistance R values as function of the ink concentration.	45
3.3	Resistance R values as function of number of the printed PANI layers. PANI ink concentration of $500 \mu g/ml$	45
3.4	Spot parameters optimization tests. The best results are the ones in the highlighted rows.	48
3.5	Voltage signal waveform parameters used for the printing on the final devices, in combination with the best spot parameters tests.	51
3.6	Printed area A values for $w250$ geometry, a comparison between short dry and long dry procedures. In both cases, the number of devices under test is 12 per each aspect ratio (the number of chips corresponds to 3).	55
3.7	Printed area A values for $w500$ geometry, a comparison between short dry and long dry procedures. In both cases, the number of devices under test is 12 per each aspect ratio (the number of chips corresponds to 3).	55
3.8	Printed area A values for $w2000$ geometry, a comparison between short dry and long dry procedures. In both cases, the number of devices under test is 12 per each aspect ratio (the number of chips corresponds to 3).	55
4.1	$\frac{I_{ON}}{I_{OFF}}$ ratio comparison.	74

Chapter 1

Introduction

The activity presented in this thesis is the result of a partnership between ChiLab-Materials and Microsystems Laboratory (Politecnico di Torino) in Chivasso and the Institute of Materials for Electronics and Magnetism (IMEM) at the National Research Council (CNR) in Parma.

In particular, the thesis work is divided in two main parts: on the one hand, the fabrication process and its optimization were executed at ChiLab. On the other hand, the electrical characterization of organic memristors was carried out at CNR-IMEM.

These devices, differently from the past, have a novelty: the active material, which is a polymer, is deposited through a inkjet printing process. The latter has many advantages, such as low costs, low material waste and high process throughput. In chapter 2, a theoretical overview about memristors is reported, with the introduction of the current state of the art. Here, the main memristor typologies are presented and their working principle described, as well as their possible application ranges. In particular, one focuses on the organic memristors, with the description of the polymeric material adopted in this work, its properties, pros and cons. Afterwards, inkjet printing technologies are proposed. The current state of the art is presented, with the explanation of the different principal actuation mechanisms for the ink droplet ejection. After that, several examples of applications taken from literature are reported, in order to show the great potentialities and the wide range of possibilities of this additive manufacturing technique. At this point, the description of the inkjet printer used at Chilab for this work is done. The inkjet printer parameters are defined, indicating how to set correctly them for an exhaustive printing result.

In chapter 3, the fabrication process flow is presented. Then, the inkjet printing optimization process, with the optimization of the polymeric ink and their results description. The chapter goes on through the discussion of the printing parameters optimization process, showing the

corresponding results. Here, two different approaches, concerning the final drying of the printed pattern on the channel devices, are investigated.

In chapter 4, the results of the thesis activity are discussed, related to the electrical characterization tests performed on the devices in Parma. In this respect, a comparison between the results obtained from the two drying procedures is done. The long dry procedure show more precise and reliable results than the short dry one, since this latter affected significantly the final pattern, in terms of polymer volume distribution. Moreover, tests about the neuromorphic behaviour and properties of organic memristive devices are introduced and their results discussed for both drying procedures. Here, good results were achieved, demonstrating the potentialities of these devices as artificial synapses.

Finally, in chapter 5, the main results are summarized, followed by proposals of further improvements of these devices for future applications.

Chapter 2

Memristors

In this chapter, memristors are described by starting from their theoretical definition. After that, the different memristor typologies and the current state of the art are reported, focusing on organic memristors, as protagonists of this thesis activity. Then, the inkjet printing technologies are illustrated, with examples coming from the literature. Finally the inkjet printer used in this work is presented, followed by the definition of its parameters.

2.1 Theoretical background

In the passive circuit theory, a set of three constitutive relationships between electromagnetic quantities can be found:

1. voltage v and current i are related to each other through the resistance R : $dv = Rdi$;
2. electrical charge q and voltage v are related to each other through the capacitance C :
 $dq = Cdv$;
3. flux linkage ϕ and electrical current i are related to each other through the inductance L :
 $d\phi = Ldi$.

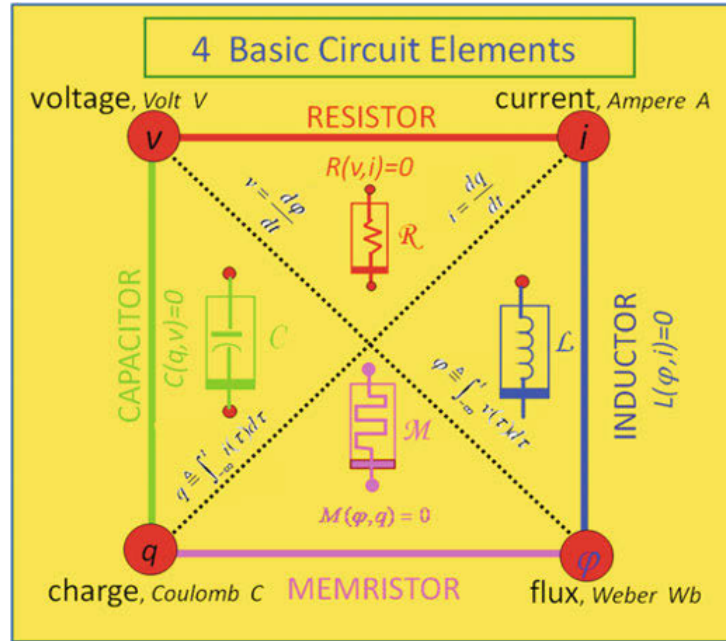


Fig. 2.1 The four fundamental two-terminal circuit elements [1].

However, Leon Chua proposed in 1971 [19] a fourth constitutive relationship between the flux linkage ϕ and the electrical charge q (Fig. 2.1). This "missing circuit element" is similar to a resistor but shows a non-linear resistance behaviour, with a memory effect: for this reason, Chua called it *memristor*¹. The generic formalism is the one as follows:

$$\frac{dw}{dt} = f(w, v) \quad (2.1)$$

$$i = G(w, v)v \quad (2.2)$$

where w is the internal state variable of the device, v the voltage, i the current and G the conductance. A memristor can be seen as an "analog" memory, since the internal state w can be found from the device conductance [20].

Memristors can be distinguished in three great categories, from the theoretical standpoint: ideal, generic and extended [21]. Ideal memristors are those ones characterized by a pinched hysteresis curve in the origin of the $i - v$ plot and the resistance value is equal to zero when the voltage drop is null. Generic memristors are those ones whose current is dependent on a generic internal state variable and on the voltage drop. Extended memristors follow the same definition of generic ones but the resistance value is different from zero when the voltage drop is null: this means that

¹Contraction of *memory-resistor*.

the hysteresis line is not pinched in the origin of the $i - v$ curve.

To prove analitically the memristor concept, one starts by defining the flux linkage ϕ and the electrical charge q as time-domain integrals of the memristor voltage v (Eq. 2.3) and current i (Eq. 2.4):

$$\phi(t) = \int_{-\infty}^t v(\tau) d\tau \quad (2.3)$$

$$q(t) = \int_{-\infty}^t i(\tau) d\tau \quad (2.4)$$

The memristor concept is defined by the so-called *memristance function* as the derivative of the flux with respect to the charge:

$$M(q) = \frac{d\phi}{dq} \quad (2.5)$$

Memristors can be defined as charge controlled (or current controlled) and flux controlled. Concerning the first one, the voltage drop v across the device reads:

$$v(t) = M(q(t))i(t) \quad (2.6)$$

where $M(q)$ comes from Eq. 2.5 and, comparing Eq. 2.6 with the Ohm's law, $M(q)$ has the dimensions of a resistance (*memristance*). For the second definition, instead, the current flowing through the device reads:

$$i(t) = W(\phi(t))v(t) \quad (2.7)$$

where

$$W(\phi) = \frac{dq(\phi)}{d\phi} \quad (2.8)$$

comparing Eq. 2.7 with the Ohm's law, $W(\phi)$ has the dimensions of a conductance (*memductance*). One can observe how the memristance is dependent on the flux and charge. The latter ones are the result of the time dependent integration of the voltage and current respectively. Even though the memristor is behaving as a common resistor, its resistance value is function of the complete history of voltage and current values [1, 22]: in other words, this dependence proves the memory effect existing in these devices. In Fig. 2.2 the behaviour of an ideal memristor can be observed, with the hysteresis loop showing the non-linear trend of the current.

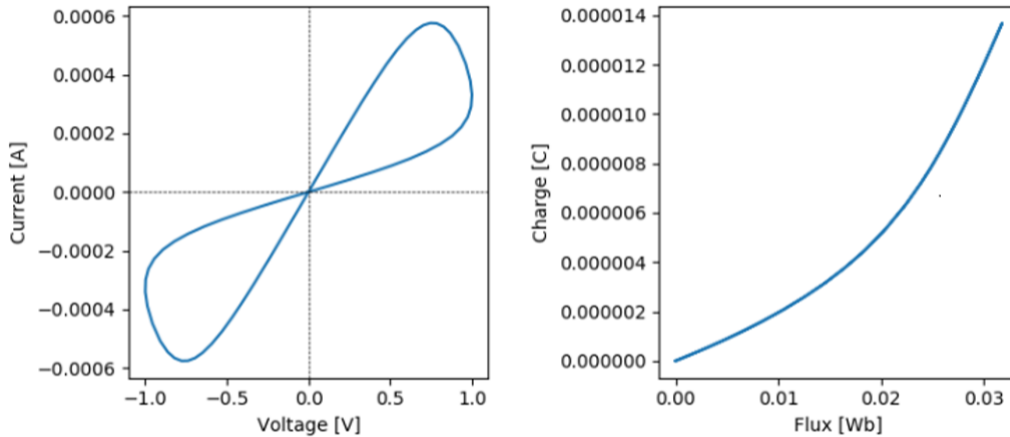


Fig. 2.2 On the left: i - v plot of an ideal memristor, where the hysteresis loop can be observed. The non-linear behaviour of such device is furtherly confirmed in the q - ϕ plot on the right [2].

2.2 State of the art

What Chua discovered and proposed was only theoretical. After 37 years, Williams and others from HP labs [23, 24] presented a memristive device, finding a link between memristor and resistive switching. The device structure was characterized by a thin layer of TiO_2 between two electrodes, made of Pt , creating a sandwich structure (Fig. 2.3a). The HP memristor working principle was believed to rely on the creation of oxygen vacancies in the TiO_2 layer, forming TiO_{2-x} . They are obtained from the application of a positive electric field that, once reaches a certain threshold value (corresponding to the breakdown field one), starts to drift the vacancies along its direction. This leads to an anionic migration and a conduction channel between the two electrodes. On the contrary, when a negative electric field starts to be applied, oxygen vacancies are pulled out of the oxide, reducing the conduction within the device: in other words, the TiO_2 film becomes insulating again. Instead, after the switching (by either positive or negative electric field), if the field is removed and becomes null, there is not anionic migration of oxygen vacancies: this proves how the memristor has memory of the last electric field value applied, with a hysteresis loop in the i - v characteristics (Fig. 2.3b). This physical mechanism is called Valence Change switching Mechanism (VCM).

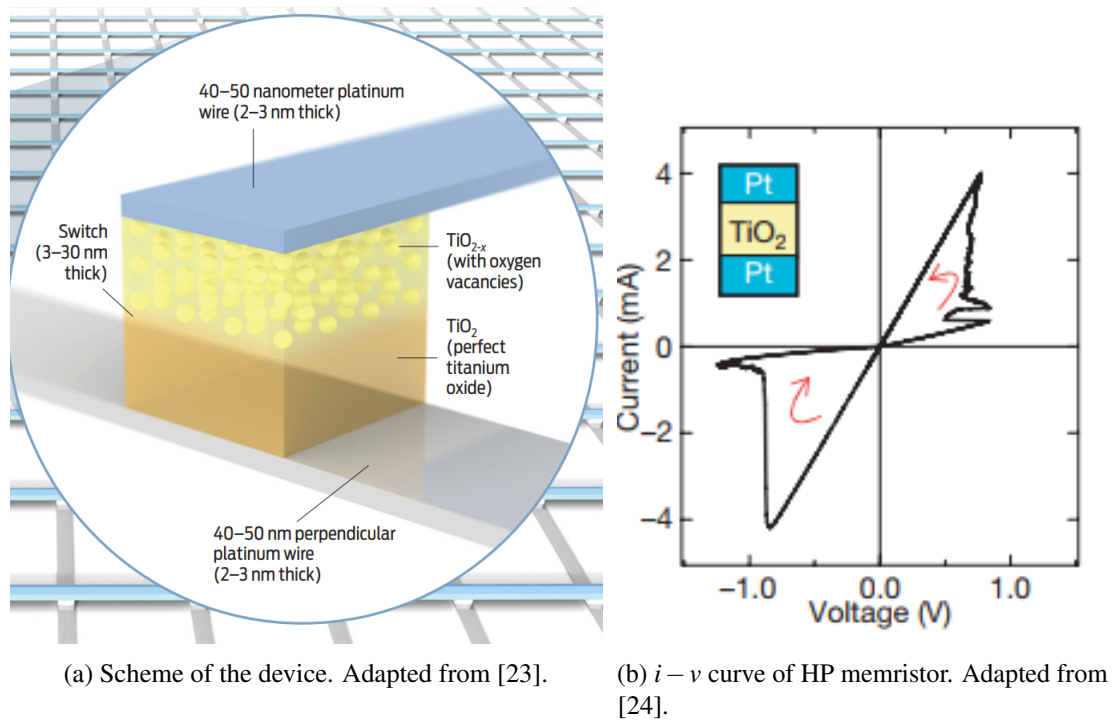


Fig. 2.3 HP memristor.

This first example opened the doors to many other proposals. In fact, memristors can be distinguished in four great families, according to the materials used for their fabrication:

- Resistive memristors;
- Spintronic memristors;
- Ferroelectric memristors;
- Organic memristors.

2.2.1 Resistive memristors

The device proposed by HP labs is part of this first category. In literature, many other materials, based on the same physical mechanism, are proposed: from binary transition metal oxides (HfO_2 , ZnO , Nb_2O_5 , Ta_2O_5 , MoO , WO , MnO , NiO , and CuO) to perovskites (like $SrTiO_3$, $Ba_{0.7}Sr_{0.3}TiO_3$, $SrZrO_3$, and $BiFeO_3$) and transparent conducting oxides, such as SnO_2 and indium tin oxide (ITO) [3]. Similarly, there are memristors based on a Electro-Chemical switching Mechanism (ECM): here, the switching is based on the creation of a conductive filament, starting from the inert electrode (made of Pt , Au or W) throughout the insulator material which acts as a solid electrolyte (Fig. 2.4). The motion of dissolved metal cations from the interface of the electro-chemically active electrode (made of Ag , Cu) into the insulator region is responsible for the conductive path [3]. The application perspectives in these cases are promising: from analog to digital, from memory to neuromorphic. However, different challenges have to be still solved. In this respect, a deeper understanding of the switching mechanisms, followed by their robust and reliable modeling, are needed. In addition to this, one has to take into account the heat dissipation during the filament formation, which is impossible to prevent, especially scaling at few nm sizes [3, 25].

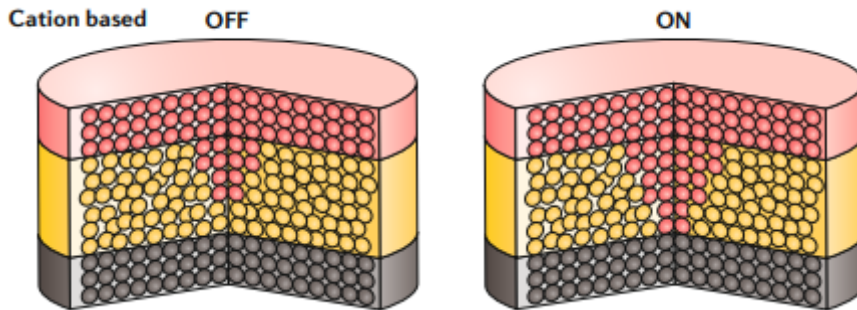


Fig. 2.4 ECM mechanism. The red bubbles are the active metal atoms, the yellow ones are the electrolyte atoms and the grey ones the inert metal atoms. Adapted from [3].

There exist materials whose switching mechanism is based on a reversible phase transition (Phase-Change Mechanism, PCM). During their working, they pass from an amorphous to a crystalline phase, from a high to a low resistance state, respectively. The amorphous phase state is the one in which the material has a disordered structure and behaves like an insulator. The crystalline phase state is the one in which the material has an ordered structure and behaves like a semiconductor. In particular, when a large and low current pulse is applied, the temperature goes towards the crystallization one (typically $400^{\circ}C$). In this way, their resistance value is reduced.

Vice versa, when a narrow and high current pulse flows through them, heating them above the melting point (typically 600°C), the material is switched from the crystalline to the amorphous phase: thus, the resistance value here increases (Fig. 2.5). Materials commonly used here are, for instance, Ag-doped and In-doped *SbTe* [4]. The tunability of the crystallization velocity allows the analogue programming of the conductance, with interesting applications in both storing memory and in-memory computing. The main issue is given by the long time needed to switch from amorphous to crystalline and so the large power consumption [26].

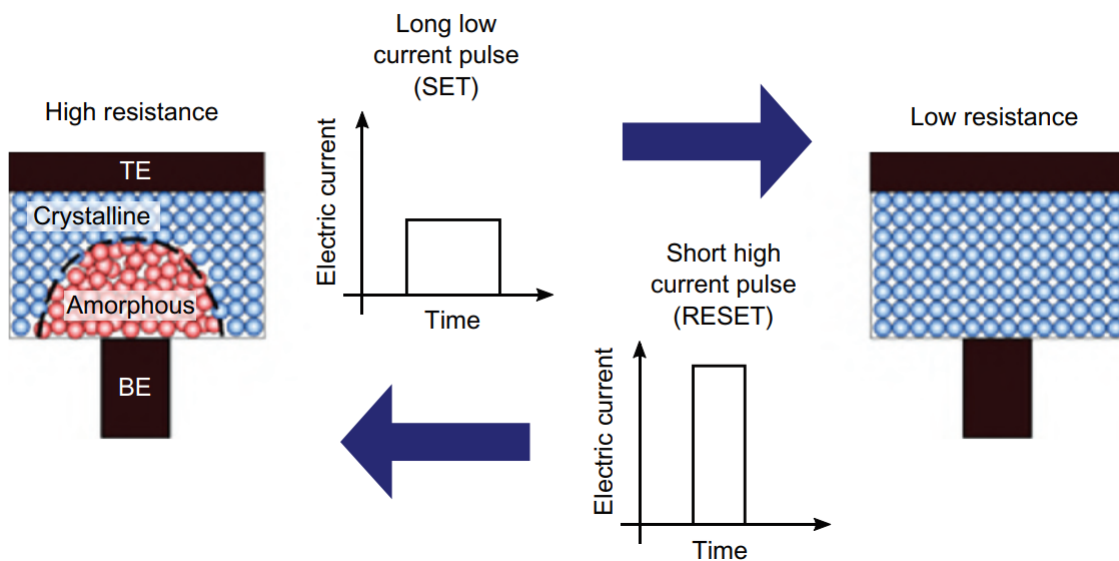


Fig. 2.5 PCM mechanism (TE=Top Electrode, BE=Bottom Electrode) [4].

2.2.2 Spintronic memristors

Spintronic memristor changes its resistance by varying the direction of the spin of the electrons. Magnetic-Tunnel-Junction (MTJ) has been used in commercial recording heads to detect magnetic flux. It is the fundamental device cell for spin torque magnetic random access memory and has also been suggested for logic devices. A material typically adopted here is, for example, *CoFeB*, creating a sandwiched structure in which the two ferromagnetic layers are separated by a thin film of oxide, like *MgO* [4, 26]. In a spintronic device, the electron spin changes the magnetization state of the device. The magnetization state of the device is thus dependent upon the cumulative effects of electron spin excitations: when the current reaches a certain critical value, the material magnetization starts to rotate, inducing the change of its orientation. It is the so-called spin transfer torque. MTJ can be switched between a low resistance value and

a high resistance value using the spin-polarized current induced between two ferromagnetic layers: one has a fixed magnetization (pinned layer), while in the other one can be switched (free layer, see Fig. 2.6). If the resistance of this spintronic device is determined by its magnetization state, a spintronic memristor whose resistance is depending on the integral effects of its current profile is obtained. The potential applications are multi-bit data storage and logic, novel sensing systems, low power consuming computing architectures and cyber security, thanks also to their compatibility with CMOS technology. The main issue is represented by the small resistance ON/OFF ratio [5, 27].

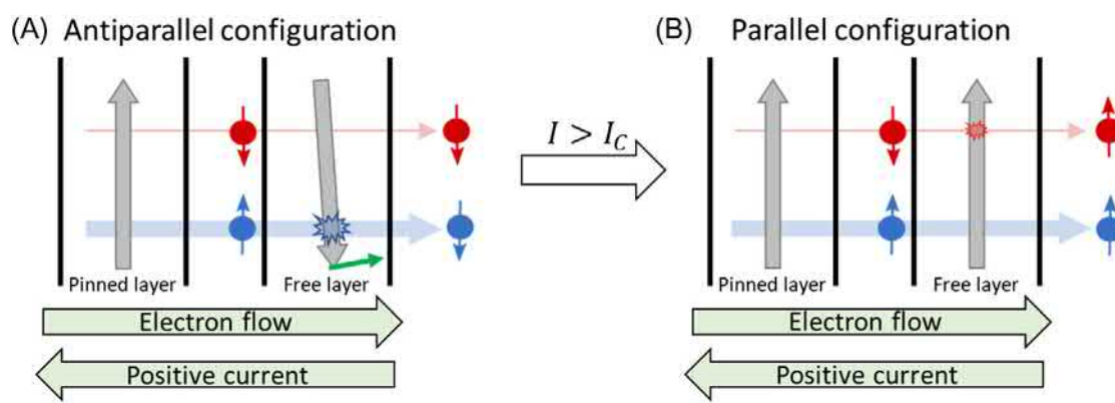


Fig. 2.6 MTJ working principle. In (A), the blue bubbles are the minority electrons (whose spin moment is opposite to the material magnetization) and the red ones are the majority electrons (whose spin moment is parallel to the material magnetization) that tunneled the oxide layer. Here the device is in a antiparallel configuration, a maximum resistance value is detected. Once the current overcomes the critical value, the switching occurs due to the spin transfer torque of spin-polarized majority electrons (B): the configuration becomes parallel and a minimum resistance value is detected. Adapted from [4].

2.2.3 Ferroelectric memristors

Ferroelectricity is a particular property for which some materials have a spontaneous electric polarization that can be reversed as a result of the application of an external electric field. The ferroelectric memristor is characterized by a thin ferroelectric barrier between two metallic electrodes (Fig. 2.7). These two opposite polarization states can be used to represent binary logic '0' and '1' values. This leads to the arise of the Ferroelectric Random Access Memory (FeRAM). Due to their nonvolatility and low power consumption [28], ferroelectric materials have been proposed in automobile equipment, ID/smart card, Radio Frequency Identification (RFID) and other embedded memory applications. The disadvantage is due to the scarce compatibility with CMOS technology, followed by a slow switching [5, 29].

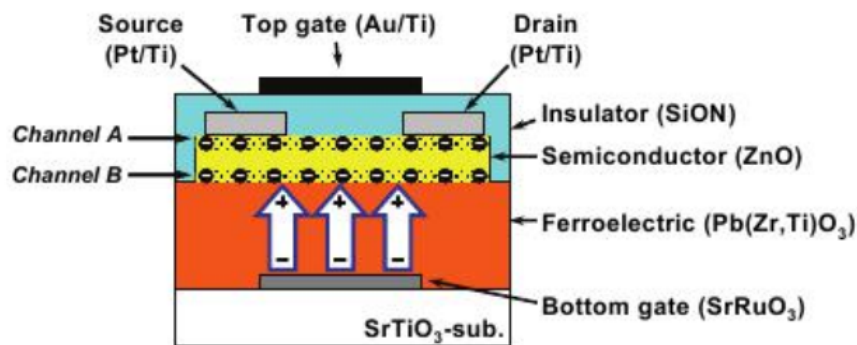


Fig. 2.7 Example of a ferroelectric memristor device. It has dual channels at the upper and lower sides of the ZnO layer, which are controlled separately by the top gate and the bottom gate, respectively. The bottom FET (Field-Effect Transistor) has the gate (SrO layer) and a ferroelectric layer constituting a FeFET (Ferroelectric FET) that shows a memory-like behaviour [5].

2.2.4 Organic memristors

Organic memristor involve the use of materials such as small molecules, conjugated and nonconjugated polymers, biomolecules, polymer complexes with chemically tethered 2D materials or nanoparticles. Moreover, several examples of devices can be found in literature, whose active layer is based on composite materials based on blends of polymers or polymers with small organic molecules, nanoparticles, ionic materials, 2D materials and so forth. In particular, concerning polymers, different switching mechanisms can be distinguished (Fig. 2.8) [6]:

- **Charge transfer:** in systems composed by donor and acceptor groups, electronic charges can be transferred from donor to acceptor moieties when a electric field is applied. As a consequence, donors are full of holes and acceptors are full of electrons. Partially filled HOMO (Highest Occupied Molecular Orbitals) levels and LUMO (Lowest Unoccupied Molecular Orbitals) ones induce the enhancement of the free charge carriers concentration, so that a switching from a high resistance state to a low one can occur.
- **Charge trapping/detrapping:** quantum dots, metal and semiconductor nanoparticles can be used as "trapping" centers for the charge carriers, which are injected from the electrodes. Applying an electric field on the polymeric layer increase the number of trapped charges and so the hopping probability from one conductive state to another, passing from a high to low resistance state.

- Conformal reconfiguration: considering for instance a PVK-PF molecule, the application of an external electric field results in a spontaneous rotation and rearrangement of the carbazole group of the molecule. This improves the charge delocalization in the $\pi - \pi$ conjugated ring system and so a higher conduction is expected.
- Pyrolysis and carbonization: thermochemical pyrolysis allows to form carbon wires inside a insulating film. As a result, the transport properties of electric charges is improved, because of the conduction paths provided by carbon wires, and the resistive switching occurs.
- Ion migration and filamentary conduction: basically, it is the same mechanism already described in subsection 2.2.1, with the creation of a conductive filament from a active electrode to a inert one and the motion of ions (positive or negative, depending on the adopted material).
- Solid-state electrochemical redox (reduction-oxidation) reaction: polymers like PEDOT:PSS (poly3,4-ethylene dioxythiophene: polystyrene sulfonate) and PANI (polyaniline) show a evident variation of their conductivity according to their redox state: devices based on this mechanism exploit three electrodes rather than two. In fact, the gate is used to control the redox reaction, by means of driving ions from the electrolyte to the polymer, leading to the resistive switching [30].

Organic memristors applications include interesting perspectives in neuromorphic computing, information storage and processing. Their advantages include low energy consumption, high uniformity, reliability, low-cost production, followed by a high integration density and biocompatibility [31, 32]. Organic memristive devices are still growing and subject to study, because different aspect have to be furtherly analyzed and considered. In fact, one of this is the integration with CMOS technology constraints such as the temperature conditions in Back-End Of the Line (BEOL) processes. Another important aspect is the lack of accurate models of the different kind of switching mechanisms, which may help their optimization process [30].

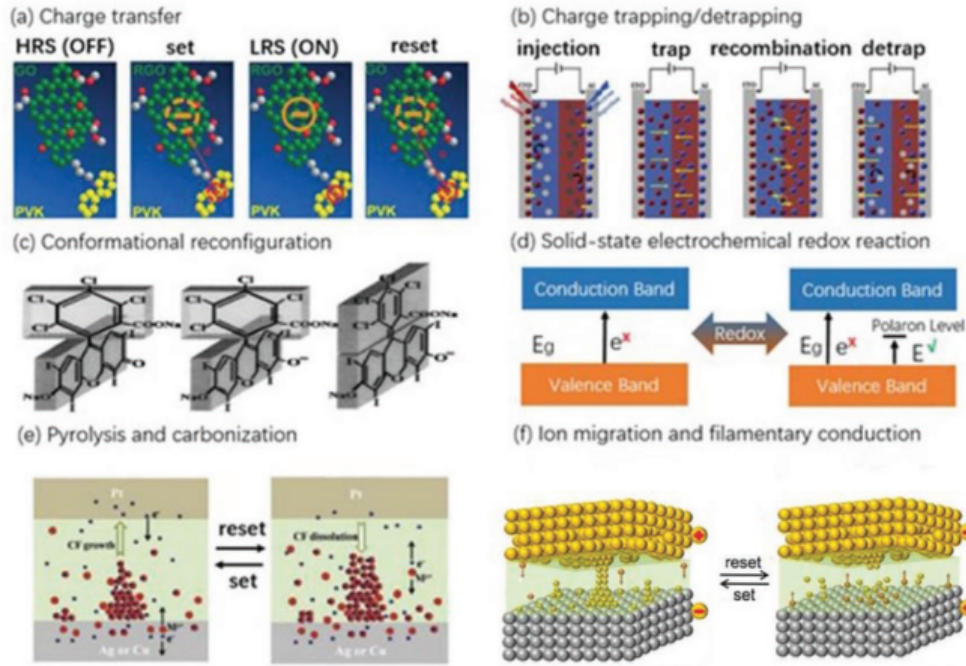


Fig. 2.8 Pictures of the different resistive switching mechanisms for organic memristors [6].

2.2.5 Applications

In the last years, memristors reached a high level of interest and several studies were reported (Fig. 2.9). Great promising applications are suggested in the realization of RAMs, thanks to their non-volatility, low power consumption, followed by scalability and compatibility with CMOS systems. Digital in-memory computing proposals can be found in literature, such as logic gates [33, 34], which can be combined in order to implement digital circuits like Full-Adders [35, 36], and digital electronic architectures like FPGAs for instance [37, 38].

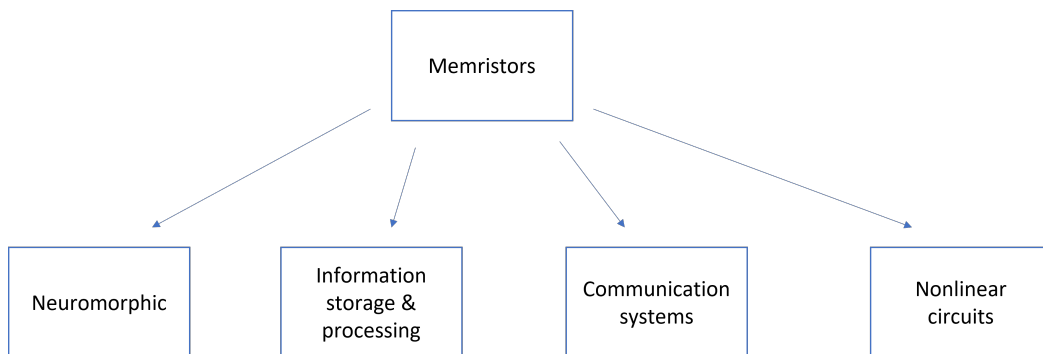


Fig. 2.9 The main memristors application fields.

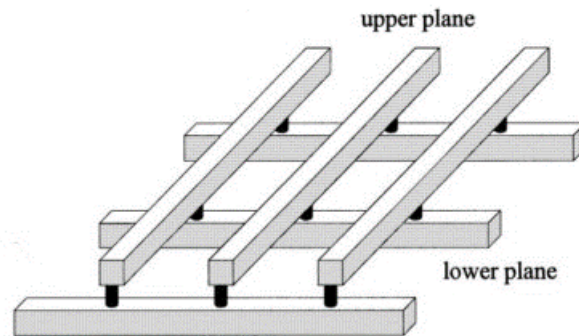


Fig. 2.11 Memristor crossbar array scheme: the white bars are metallic nanowires while the black cylinders correspond to memristive devices [8].

Associative memories based on memristors have been proposed, able to map the input pattern to an output one according to the similarities found in the input pattern with respect to the pattern stored in the memory [51, 52]. Good results have been obtained by realizing memristor-based architectures for image recognition and edge detection: the latter refers to the identification of relevant variation of a digital image, which can be the object outline. Basically, the light intensity of the original picture is applied as voltage to points on a memristor grid. The resulted temporal resistance variations across the grid are then shown in the frames. Therefore, once the system can be set, the edge detected image can be recovered through the resistance measurement of each grid element [53, 54].

2.2.6 Introduction to PANI-based memristors

In the respect of this thesis work, it is needed to focus on organic memristors, whose resistive switching mechanism relies on a redox reaction. In particular, the devices introduced in this discussion are realized by using PANI.

Concerning the latter one, it can assume different forms, going from a completely reduced (leucoemeraldine, yellowish) to a semioxidate state (emeraldine state). This latter can assume two forms depending on the external pH: emeraldine base in case of $\text{pH} > 4$, while emeraldine salt in case of lower pH values. In this case of study, the starting point is the emeraldine base (with a blue colour), because of its higher processability. However, to achieve this goal, the polymer needs to be doped. Doping procedure can be done in different ways, but here it is executed by simply dipping the polymer in an acid solution², in particular HCl 1M. Basically, the polymer chain undergoes to protonation, leaving a hole in it, while the Cl^- ions get closer to the chain: emeraldine base gets a green colour, turning into emeraldine salt form (Fig. 2.12) [9, 10].

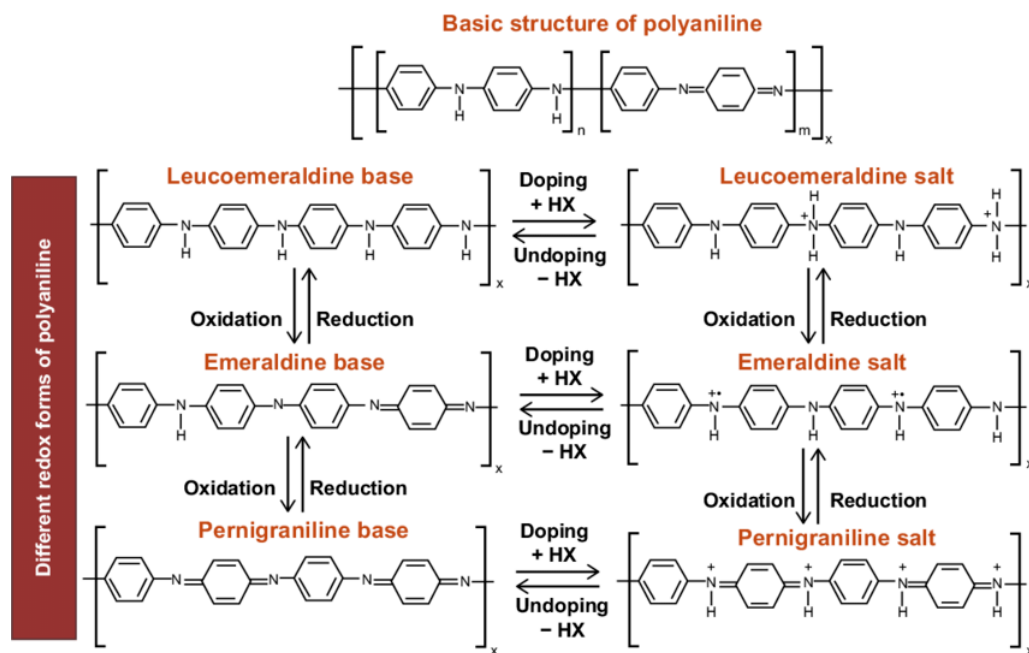


Fig. 2.12 PANI redox and doping schemes [9].

PANI-based devices were proposed for biosensing applications, since this conducting polymer is able to bind with biomolecules and tune their bio-catalytic properties [56]. Moreover, specially

²The choice of the electrolyte is important here, since the ions properties have a key role for the electrical performances and response of organic electrochemical devices [55].

prepared PANI layers show biocompatibility with neuronal cells, allowing the cellular growth without alterations, if compared to the same growth executed on a glass substrate [57]. Its capability of changing its resistance value according to the redox state can be exploited for neuromorphic and brain-inspired computing. In fact, tests were carried out by combining organic memristors into a single and double layer perceptron, respectively. A perceptron is an artificial neural network used to solve simple tasks like invariant pattern recognition, linear approximation, prediction and so forth. A single layer perceptron is composed by a circuit in which memristive devices act as artificial synapses. Their internal conductance acts as synaptic weight, since it can be adjusted by proper stimulation with voltage input signals. All the relative currents (modulated by memristive conductance values) are summed up and a single output current is obtained (Fig. 2.13).

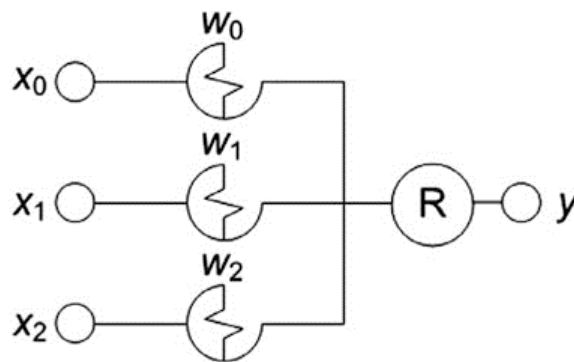


Fig. 2.13 Single layer perceptron scheme [10].

Unfortunately, single layer perceptrons have the limitation of being suitable only for linearly separable objects. Therefore, in order to classify also not linearly separable objects, a double layer perceptron is necessary. For what concerns the latter one, there are the inputs and neurons connected together through synaptic weights, each of them implemented with two memristors (Fig. 2.14). This system was used to execute two actions: on the one hand, reading the voltages during the information processing. On the other hand, it imparts voltages to the selected memristive devices during the training procedure [10].

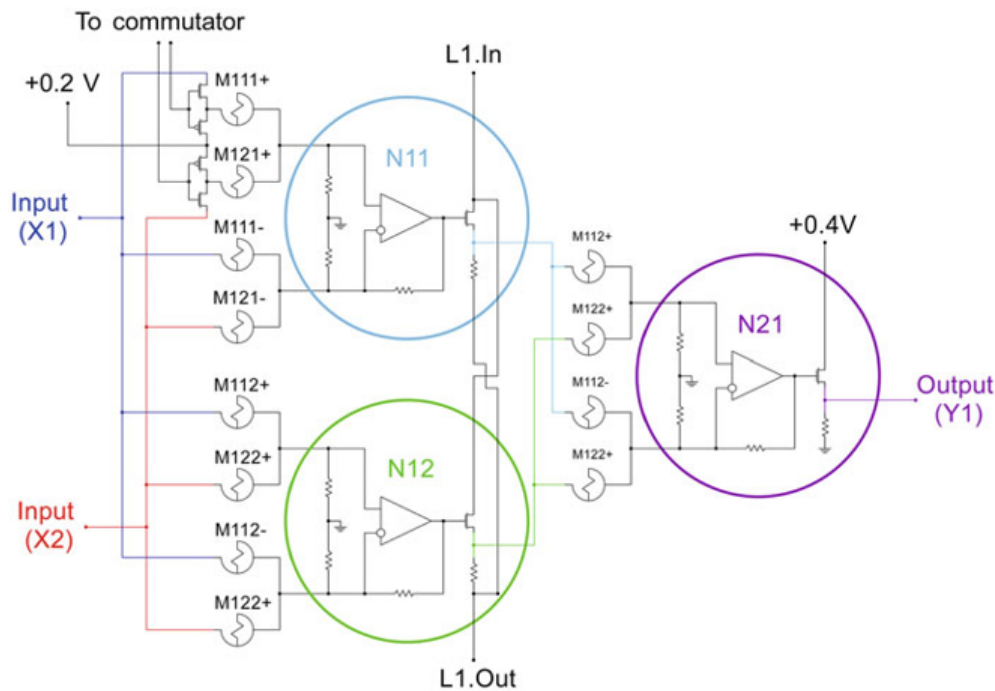


Fig. 2.14 Double layer perceptron scheme: neurons are highlighted by circles and are characterized by differential summator and activation function. Enumeration of memristive links ($Mn_{ij}(+/-)$) includes the n -th layer, associated with the i -th input and the j -th output neurons. A sign defines whether this partial weight is positive or not [10].

These devices were suggested also for logic gates: their output signal is analog and it depends on the time required for a suitable charge to be applied to the inputs, showing a learning property. The memristive property of the gates allows to provide analog outputs that vary according to the charge-dependent nonvolatile memristive state. Moreover, they can be combined together, in order to realized more complicated circuits such as an Half-Adder or a Full-Adder [58]. The advantage of organic memristors relies on their "analog" behaviour, which allows to go closer and closer to what actually happens in biological neurons. This leads to a lower required energy for the correct device operations, if compared to inorganic devices. The latter ones, even though faster than the organic devices, do not show an analog output, but a digital one. The high switching rate provided by them is detrimental for neuromorphic systems, since the switching kinetics in those devices is uncontrollable [10].

From the fabrication standpoint, PANI-based memristors are compatible with standard micro-electronic technology, through common fabrication steps such as photolithography, etching and so on, in order to realize the devices layout. After that, the polymer deposition on the device channel is needed. There exist many additive manufacturing techniques that can be adopted to deposit PANI [59, 60]. However, the thickness of the deposited polymeric layer in these devices

has a primary role [10]: on the one hand it has to be thin enough because of the ions diffusion in the solid-phase material during the redox reaction. On the other hand, it has to be thick enough to get reasonable current values during the electrical measurements. So far, PANI was deposited on the device channel by using a modified version of the Langmuir-Schaefer technique.

The latter consists of the polymeric solution spreading at the interface between air and water, so that the molecules in the monolayer get expanded. After that, the polymeric monolayer is compressed with barriers and moved onto solid supports. Instead, the modified version includes some additional steps. Once the monolayer is compressed, the barriers are stopped and a grid, whose cells sizes correspond to the ones of the sample, is positioned on the monolayer. The sample gets in touch with the monolayer in each cell, with the removal of the water drop by an air jetting after each monolayer transfer. This separation with the grid is needed, in order to cover homogeneously the sample surface with the deposited layer. Otherwise, every touching would result in not only the direct contact of the PANI monolayer with the sample, but also the the water drop on the sample surface. This would imply the transfer of a uncontrollable structure and a non-homogeneously deposited film. This technique provides few *nm* thick monolayers and a homogeneous multi-layer film. However, it requires time and only one device per session can be submitted, something not suitable for a wider scale production.

For this reason, the organic memristors discussed in this thesis are fabricated by depositing PANI through a inkjet printing process. As well explained and reported in section 2.3, this additive technique allows to deposit a material on more than one samples in a single session, reducing fabrication time, increasing the process throughput and reducing the costs, without affecting the devices performance.

2.3 Inkjet printing technologies

Inkjet printing technologies have become really convenient and advantageous in industrial applications, since they provide low material waste and less fabrication costs, good repetitivity and a huge range of possible application fields (see subsection 2.3.5). However, resolutions below the μm range are difficult to be achieved. Two approaches are distinguishable to overcome this issue [11]:

1. a "top-down" approach, in which micro-structures are used for the patterning formation during the printing process (Fig. 2.15);
2. a "bottom-up" approach, with the optimization of the ink synthesis and the improvement of specific physical and/or chemical properties of the ink.

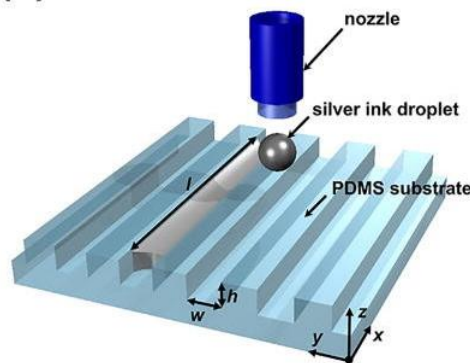


Fig. 2.15 Scheme of inkjet printing process executed on a patterned PDMS substrate. Adapted from [11].

In principle, two main types of inkjet printing exist: Continuous InkJet (CIJ) and the Drop-On-Demand (DOD) one, as schematically represented in Fig. 2.16. The first one, as already suggested by the name itself, consists of a continuous jetting of ink. Basically, the CIJ printer is characterized by a pump, which carries fluid from the reservoir to the nozzle. The latter ejects a continuous flow of droplets, resulting from the vibration of a piezoelectric crystal: in fact, an electric field introduces a charge and the so charged droplets go through a deflection field, which establishes the drop landing. Those ones which are not printed are collected, so that there is no waste of ink and they can be reused in new printing sessions. On the one hand, CIJ is suitable for volatile solvents-based inks for example, providing fast drying and improving the adhesion on the substrate involved in the process. On the other hand, it has a limited resolution and the use of

volatile solvents-based inks gets this technology detrimental and polluting for the environment [61].

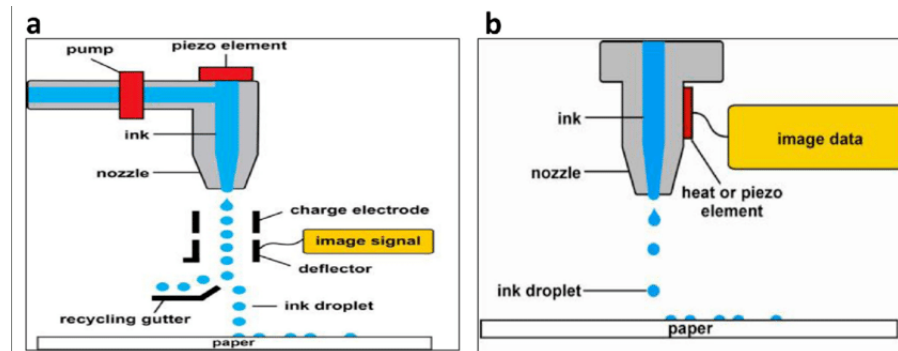


Fig. 2.16 Scheme of CIJ (on the left) and DOD Inkjet (on the right). Adapted from [12].

The DOD inkjet printing, generally, includes the drops generation only when required, as a result of a pressure pulse. It is possible to distinguish different classes of DOD inkjet printers, based on different working principles. The most relevant ones rely on:

- thermal actuation principle;
- electrostatic actuation principle;
- acoustic actuation principle;
- piezoelectric actuation principle.

2.3.1 Thermal actuation

Thermal inkjet printers (Fig. 2.17) are the most common ones: here, ink droplets are the result of a fast heating of a resistive element (which reaches temperatures about 350°C-400°C) in the ink chamber. This leads to the vaporization of a thin ink film above the heater, creating a bubble and consequently a pressure pulse, which results in the formation of a drop ejected from the nozzle. Ejection is followed by the refilling of the void left by the droplet, repeating the process step. Very small diameter sizes of the drop are achievable, as well as high density of nozzle in the printer. However, the fluid types range is not so large, since in this actuation principle the vapourization of the ink is required and, in case of a not well-prepared solution, the high temperature regime can lead to a hard coating on the resistive element that may affect the performances and the lifetime of the printhead itself [13, 61, 62].

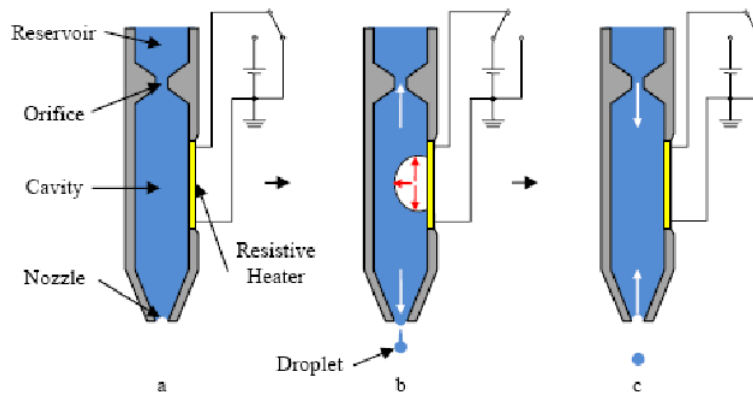


Fig. 2.17 Thermal inkjet working principle [13].

2.3.2 Electrostatic actuation

For electrostatic inkjet systems (see Fig. 2.18), the working principle consists of a drop ejection from an orifice by applying an electrostatic field between the orifice and an electrode. The field imparts an electrostatic force, attracting to its surface free charges present in the ink so that, once this force becomes greater than the ink surface tension, a droplet is generated. Advantages coming from this type of printer are the feasibility of denser fluids and high resolutions that are independent on the nozzle sizes. Limitations are the high costs and the need of a conductive ink for an exhaustive outcome [14, 61].

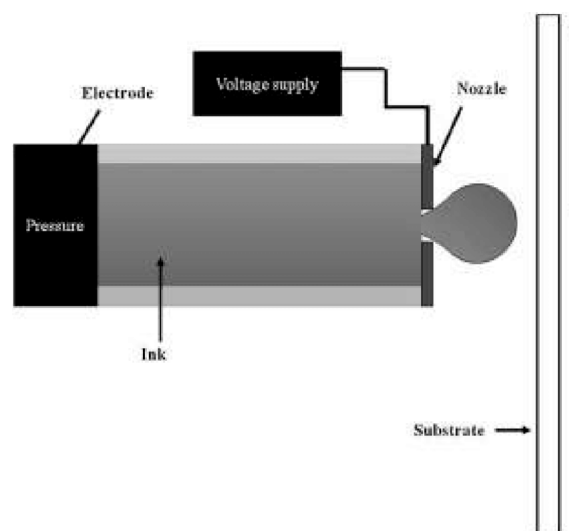


Fig. 2.18 Electrostatic inkjet scheme [14].

2.3.3 Acoustic actuation

Acoustic inkjet printing (Fig. 2.19) is a technique that does not involve the use of nozzles, allowing to overcome the main limitation of DOD inkjet printing technology related to the dependence of the droplet diameter sizes on the nozzle dimensions. In this case, ink droplets can be obtained by focusing acoustic waves at high frequency range (from 5 to 300 MHz) on the liquid ink surface, through a proper lens. Very small droplets are achievable, whose diameter goes from 5 to 300 μm . Drawbacks are the great variability of diameter sizes of the drops and the impossible deposition of different inks within the short period on the same area, because of the larger amount of time required for the activation of the interested chemical reactions [11, 15].

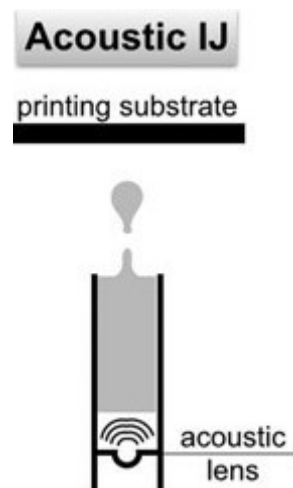


Fig. 2.19 Acoustic inkjet scheme. Adapted from [15].

2.3.4 Piezoelectric actuation

In this kind of inkjet printers, the nozzle is characterized by a piezoelectric crystal, such as lead zirconium titanate. The application of an electric field (and so a voltage drop between the electrodes constituting the piezoelectric actuator surrounding the reservoir walls) introduces a distortion, creating a pressure pulse wave that causes the droplet ejection from the nozzle (Fig. 2.20). It is one of the most chosen inkjet printing techniques for promising and emerging industrial applications, as well as within the R&D field, because it does not imply any restriction on the ink type to be tested and guarantees a long printhead lifetime (differently from the case of thermal inkjet). However, its issues are the droplet size dependence on the nozzle diameter

(disadvantageous if compared with acoustic and electrostatic inkjet printing cases) and the costs associated with the piezoelectric actuator [11, 16, 61, 62].

Furthermore, this actuation principle is the one used in this thesis work (see section 2.4). In this respect, the parameters defining the pulsed voltage signal typically used as stimulus for the piezoelectric actuator must be properly set to optimize the printing process and the final result [11, 63]: in section 2.5. Those parameters are better described and their proper choice for the waveform definition is reported.

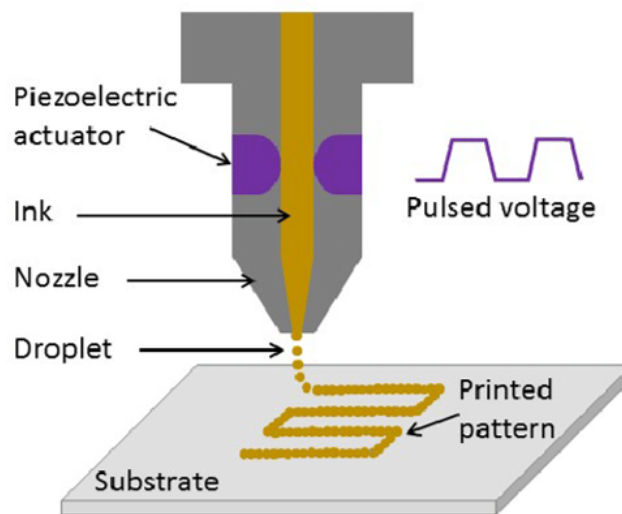


Fig. 2.20 Piezoelectric inkjet printhead sketch [16].

2.3.5 Applications

Inkjet printing technology, as aforementioned, has found many interesting application opportunities, both at the industrial and research level. The fundamental aspect and the starting point is the material on which the ink is based: nowadays, the progress in the synthesis of more and more printable inks is going on [61].

Optoelectronic applications, such as photodiodes, solar cells, light-emitting diodes and transparent electrodes are suggested in literature [64], thanks to photosensitive material-based inks. The study of functional material properties lead to great progress in the ink preparation: conductive inks based on synthesized nanoparticles made of gold, silver and copper allow the use of inkjet printing in microelectronics, especially for packaging and MEMS (Micro-Electro-Mechanical Systems) [65]. Quack and others [66] reported a successful Through Silicon Vias (TSV) and

thermocompression bonding by inkjet printing of gold nanoparticles in a single process step, with TSV radii size from 25 to 50 μm , opening the doors to the heterogeneous integration of different technologies, such as CMOS, MEMS and Silicon Photonics, optimizing the costs. Xu and others [67] formulated a graphene/PANI ink to produce thin film electrodes, getting good results in terms of pattern geometry and position, electrical conductivity and film thickness.

Inkjet printing is subjected to deep interest in flexible electronics, as in the case introduced by Kim and others [68]: Single-Wall Carbon NanoTubes (SWCNTs) based inks are proposed for the direct printing of ambipolar transistors and a new class of circuits composed by them. A CNTs-based ink has also been adopted for the direct printing of electrodes in a digital microfluidic circuit on a paper substrate [69], showing potentialities in that field. Promising perspectives are suggested in sensing application, from wearable electronic devices [70–72] to electrochemical sensors [73], gas sensors [74–77], mechanical sensors [78–81] and radio-frequency systems such as antennas [11, 82, 83]. Inkjet printing technologies has been tested for data storage applications and so memory systems, by preparing ink solutions based on resistive materials [84–93], allowing the creation of resistive switching devices like the ones proposed in this thesis activity. Applications in the biological field can be found in literature, such as the printing of bio-materials like proteins, enzymes and living cells: however, there are still challenges to be solved. Researchers are trying to understand, for instance, the denaturation mechanism of proteins during the printing process, since the development of bio-materials is influenced by the chemical properties and the temperature range in which they can work properly [13, 15, 94]. Examples can be also found within the medical field, in particular for tissue engineering, regenerative medicine and medical devices realization, as well as in the composites synthesis for pharmaceutical purposes [95, 96]

2.4 Jet-Lab4 inkjet system

Concerning this thesis work, the inkjet printing system available at Chilab is a Jetlab 4 DOD, by MicroFab Technologies Inc.®(Fig. 2.21). It is composed by a single-nozzle printhead that can move along a horizontal platform, whose area is $30 \times 30 \text{ cm}^2$. The orifice diameter of the nozzle (Fig. 2.22) is $50 \mu\text{m}$ and has electrodes in order to apply the pulsed voltage drop signal needed for the piezoelectric actuation. Moreover, the inkjet printer is driven by a specific software (*jetlab4.exe*), provided by the manufacturer. The main printing settings can be set from this driving software the script containing the additional instructions to print the pattern, can be loaded as a *.txt* file generated from another pre-installed software (*gds2jetlab.exe*), or provided externally by the user. *gds2jetlab.exe* allows to convert a *.gds* file into a *.txt* file, readable by the printer controlling software. The *.gds* file is taken from CleWin®software, where the UV mask of the device can be designed. It is important for the lithography process, which is part of the device fabrication flow (see chapter 3).

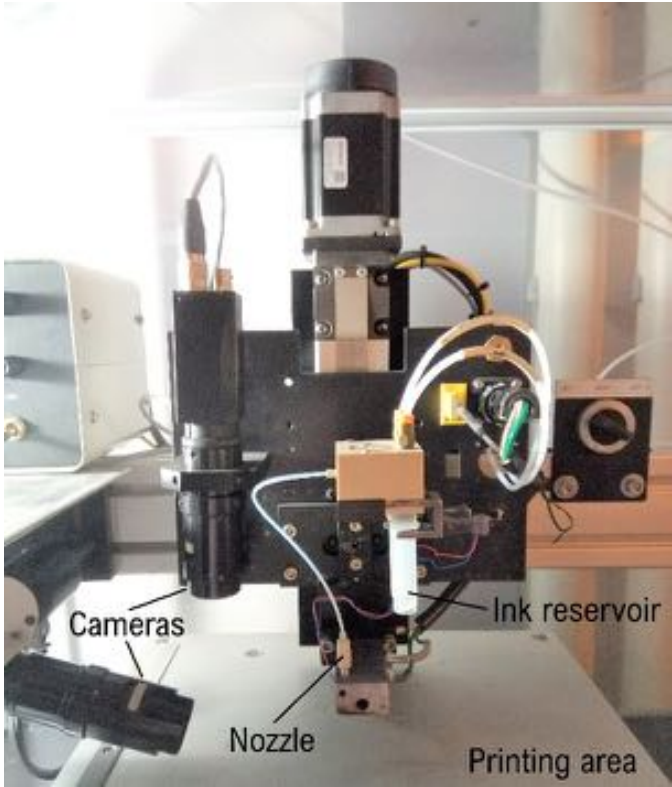
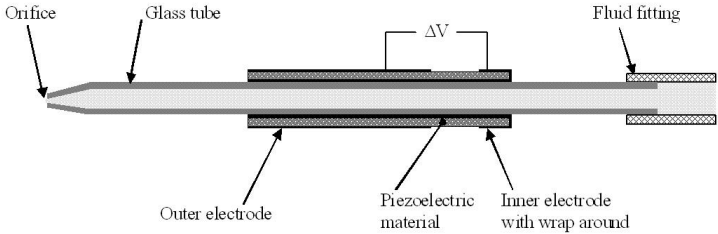


Fig. 2.21 Jetlab printing system picture, courtesy of [17].



(a) Photo, a courtesy of [17].



(b) Schematic representation, from MicroFab website [97].

Fig. 2.22 Inkjet printer nozzle.

2.5 Inkjet printer settings

For a correct and optimal inkjet printing, the most important parameters controlling the dimensions of the droplet, its formation and stability have to be set. They are the back-pressure and the voltage signal waveform applied to the piezoelectric actuator. In particular, the signal waveform includes the voltage amplitude, time constants and frequency. The ejection can be observed by a laterally positioned camera (Fig. 2.23).

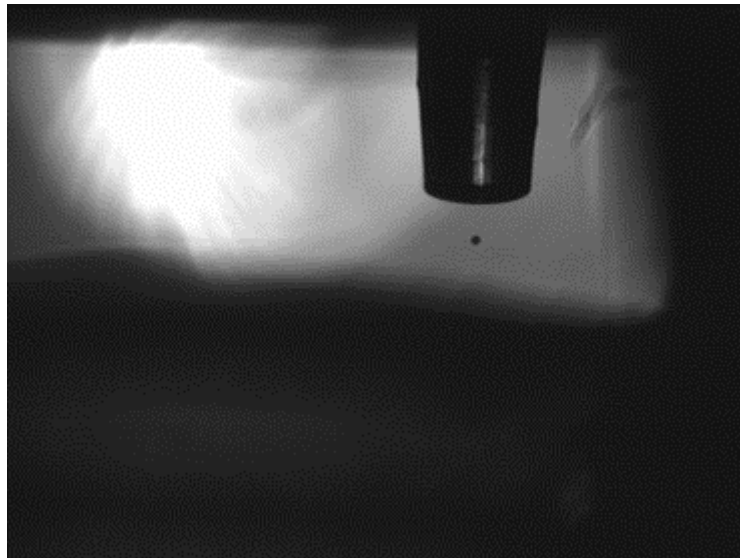


Fig. 2.23 Droplet ejection from the nozzle, snapshot taken by the inkjet printer lateral camera.

2.5.1 The back-pressure

A pressure pump is provided with the inkjet printer, in order to keep the ink reservoir under pressure, called *back-pressure*. The latter can be visualized, in the front panel of the printer, in psi^3 and it is manually configurable. A positive value of back-pressure is associated with a force pushing the ink surface, transporting it towards the nozzle through a fluidic channel. As a result, once the air is removed, huge droplets are ejected from the nozzle (Fig. 2.24), meaning that the fluidic channel is full of ink.

³pound per square inch, 1 psi=6.805 · 10⁻² atm=6.895 kPa



Fig. 2.24 Positive back-pressure result: a big droplet ejected from the nozzle, snapshot taken by the lateral camera.

To prevent the droplet from being ejected spontaneously during the printing session, a negative back-pressure is needed, as graphically represented in Fig. 2.25. The negative back-pressure is an effective strategy to avoid the waste of ink, since a too large ink volume ejection may lead to the uncontrollable formation of several droplets. Moreover, it allows to define more precisely the pulse width, as well as the time intervals to get smaller and smaller drops [18]. The higher the ink viscosity, the larger should be the back-pressure, in order to prevent ink leakages from the orifice because of their greater weight.

Typically, for the PANI-based ink used in this work, the optimal values are approximately in the range of -20 psi and -6 psi. For values larger than -6 psi, the ink flows from the nozzle due to its own weight influence. For values smaller than -20 psi, the ink starts to be held in the reservoir, without drop jetting.

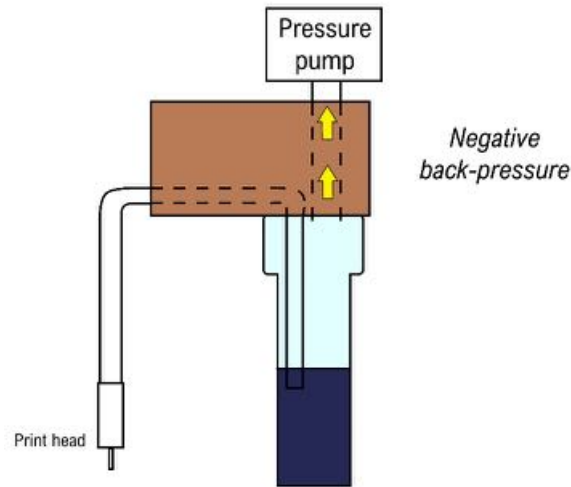


Fig. 2.25 Negative back-pressure working principle, sketch [17].

2.5.2 The driving voltage signal waveform

The voltage signal waveform is a fundamental element for the piezoelectric actuator of the printer. It is furtherly important for the jetting stability and the size and quality of the droplets.

Whatever waveform can be designed: the simplest one able to form ink drops is the unipolar waveform, in other words an on/off pulsed signal (Fig. 2.26). It enables the piezoelectric actuator to move and return subsequently to rest. The parameters of the driving waveform can be manually chosen and changed, in particular:

- positive voltage amplitude, called *dwel voltage*, imparting the piezoactuator contraction;
- *rise time*, defining the time interval in which the piezoactuator contraction occurs and so the fluid expands;
- *fall time*, defining the time interval in which the piezoactuator expansion occurs and so the fluid contracts;
- *dwel time*, used to compensate the pressure wave generated by the contraction.

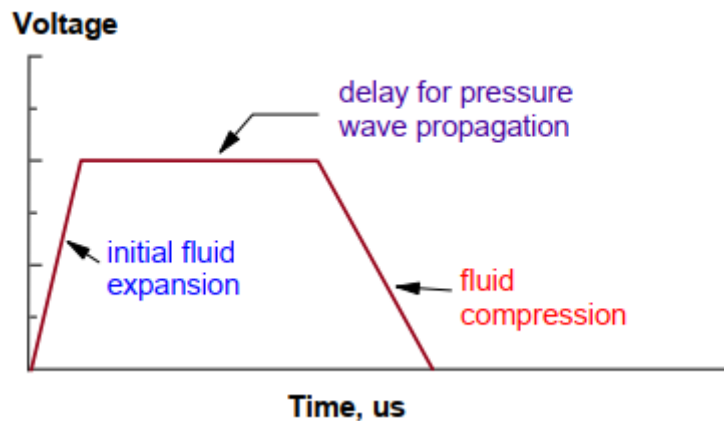


Fig. 2.26 Plot of a unipolar signal waveform [18].

In the respect of the thesis work presented here, the driving waveform adopted is a bipolar wave (Fig. 2.27). The latter is characterized by other parameters, to be added to the previously defined ones, such as:

- negative voltage amplitude, called *echo voltage*, imparting the piezoactuator expansion;
- *echo time*, used to compensate the pressure wave generated by the contraction.

Therefore, a bipolar wave is more advantageous and feasible than a unipolar one. In fact, the echo voltage component has the role of canceling residual oscillations remaining in the chamber after the ink drop ejection (due to the dwell voltage component).

In other words, the droplet formation is more stable if stimulated with a bipolar wave rather than a unipolar one.

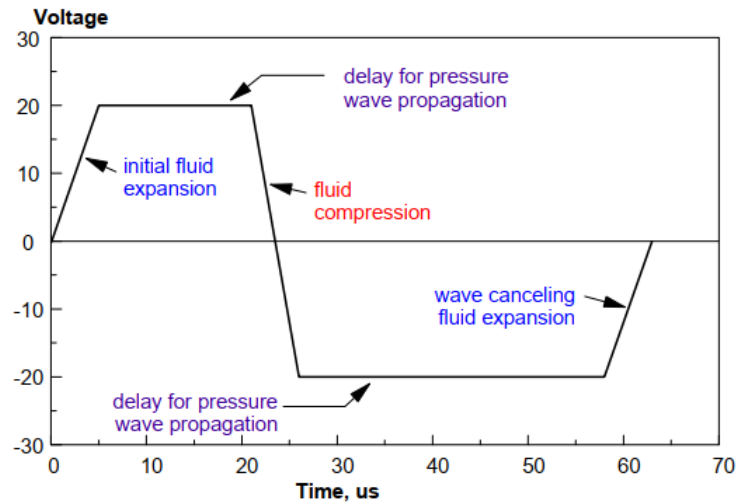


Fig. 2.27 Plot of a bipolar signal waveform [18].

In the perspective of printing microelectronic devices, the pulse amplitude and width must be properly chosen in order to get the lowest drops volume. This ensures a better printing resolution. In fact, the larger the amplitude, the larger the droplets, followed by an increase of the ejection velocity [18, 98]. Moreover, the presence of satellites is more probable for those values (Fig. 2.28). Satellites are undesired drops: they might result from the application of the voltage waveform in low viscous fluids. In that case, the pressure waves are still propagating in the nozzle after the drop formation: satellites could be generated if larger amplitude have enough residual energy.

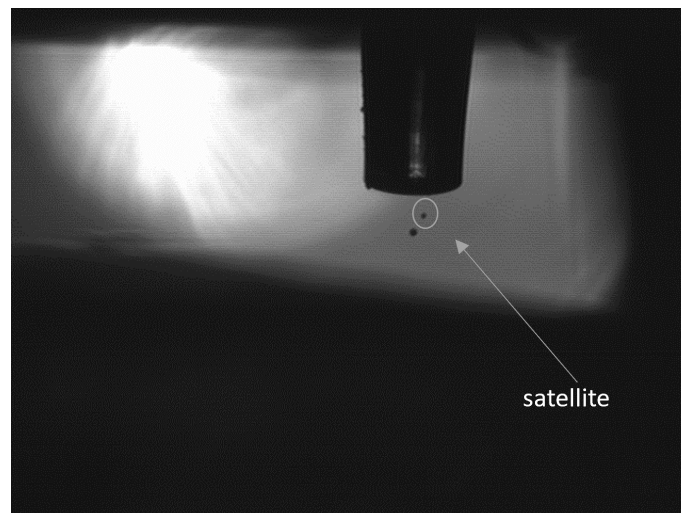


Fig. 2.28 Satellites formation, snapshot taken by inkjet printer lateral camera.

Basically, the best bipolar waveform signal is composed by the same positive and negative voltage amplitude value and the echo time is twice the dwell one [18]. However, this is not always true, since modification during the optimization process may occur.

Moreover, as suggested in the next chapter, the negative and positive wavefront defining the bipolar wave can be switched (i.e. the "dwell" wavefront is negative, the "echo" one is positive, see Fig. 2.29), because they can provide better results in terms of droplet quality and sizes [11]. The rise and fall time are typically set equal and their value is proportional to the voltage amplitude values: indeed, the larger the voltage amplitude the larger would be the rise and fall time. In the context of this work, the typical values are 3-4 μs . Anyway, to prevent undesired effects such as the aforementioned satellites and to obtain smaller and smaller droplets, those values should be as small as possible [98].

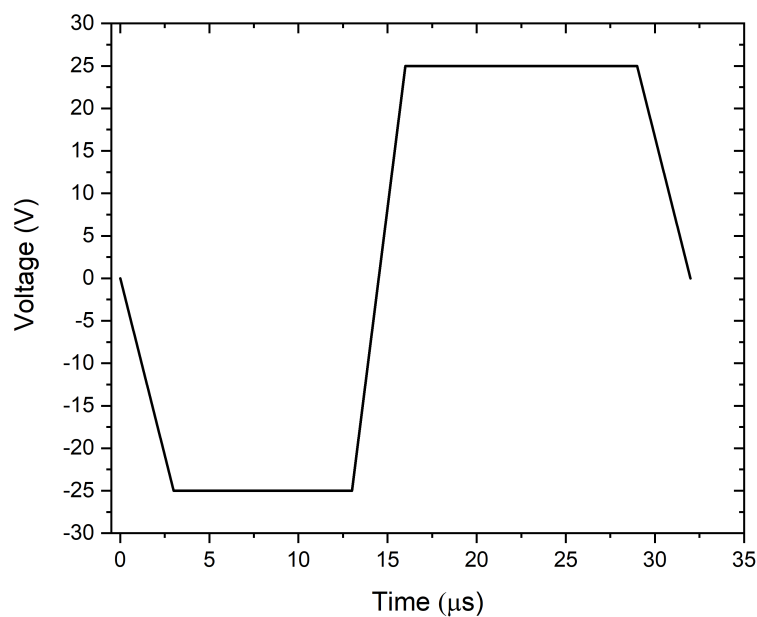


Fig. 2.29 Another example of a bipolar waveform signal.

The frequency is another important parameter, it can be in the order of 1000 Hz or even more, increasing the droplet ejection speed. There is not a rule of thumb in this case, the choice is dependent on the adopted ink solution.

2.5.3 Spot parameters

Other important parameters are related to the droplet disposal, manually inserted or modified by the user in the controlling software:

- *spot spacing*, i.e. the distance between the center of two neighbour drops (Fig. 2.30);
- *spot margin*, i.e. the distance between the droplet center and the edge of the pad (the single die layout);
- *fly velocity*, i.e. the velocity reached by the droplet in the path defined between the nozzle end and the sample surface.

The spot spacing is chosen accordingly with the single droplet sizes: the larger the droplet, the larger the spot spacing. On the contrary, if the signal waveform parameters are designed in such a way that the droplet dimensions are smaller, the spacing should be reduced, otherwise the resulting pattern would be not uniform, characterized by parts of the sample not covered by the ink. Similarly, the spot margin is chosen according to the drop sizes: there is not a specific rule, the only solution is a "trial and error" approach. In any case, a too large spot margin may lead to the misalignment of the printed pattern on the surface.

The fly velocity value is related to the frequency of the ejection. If these two are not chosen properly and there is a mismatch, the printing outcome quality is seriously influenced.

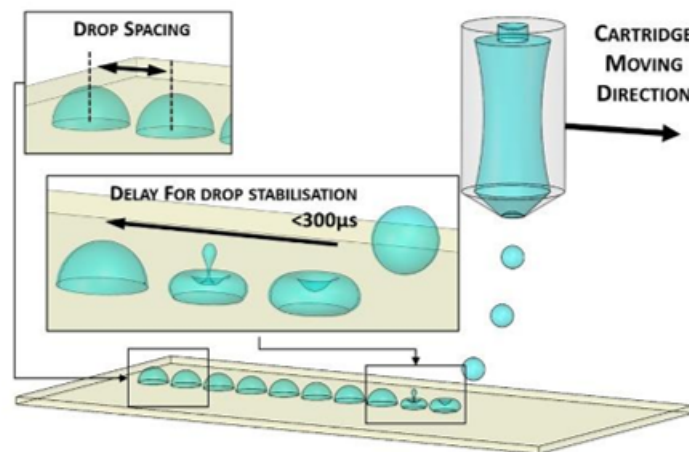


Fig. 2.30 Inkjet printed drops on substrate, highlighting the spot parameters. Adapted from [11].

Chapter 3

Materials and fabrication processes

In this chapter, the fabrication process is presented, including the ink optimization tests and the optimization procedure of the inkjet printer parameters. Finally, a morphological analysis of the printed patterns is reported, comparing two drying procedures.

3.1 Fabrication procedure

In order to realize memristors, the process adopted is the standard one in microelectronics (Fig. 3.1), carried out in the cleanroom facility at Chilab:

- a) a silicon wafer is heated up to 120°C for 2 min to remove humidity (due to the exposure to the atmosphere). The wafer is 575 μm thick, with 1 μm of silicon dioxide (SiO_2) on top of it;
- b) deposition of 10 nm of titanium, as adhesion layer with the silicon oxide substrate, by evaporation;
- c) deposition of 100 nm of gold by evaporation. It is the metal chosen for the device electrodes;
- d) spin-coating of AZ1518 positive photoresist, followed by a baking at 110°C for 1 min to dry it;
- e) lithography process, by UV exposure of the wafers into a MICROTECH®Laser Writer LW405A. The laser writing is carried out by inserting in the control software the *.gds* file of the UV mask with the desired geometry (Fig. 3.2). The latter defines the pattern for the laser light exposure: as discussed in the next section, the considered geometries are 3, where the aspect ratio of the electrodes was varied;
- f) photoresist development, into a baker filled with 300 ml of water and 100 ml of AZ400K developer for 40 s about. To stop the development, the wafer is immersed into another baker, filled with deionized water;
- g) gold wet etching for 1 min and 35 s, in a glass crystallizer, with TechniEtch™ACI2 solution (an Iodine based Gold etchant [99]). Instead, titanium wet etching executed for 10 seconds in a plastic crystallizer with a HF-based solution ((proportion Hf 38% : H_2O_2 : $\text{DI-H}_2\text{O}$ = 1 : 1 : 20)). After that, the remaining photoresist is removed by washing wafers with acetone and isopropanol;
- h) wafer dicing into single dies, executed through a laser cutting by Microla s.r.l. ;
- i) PANI inkjet printing process, as reported in section 3.2.

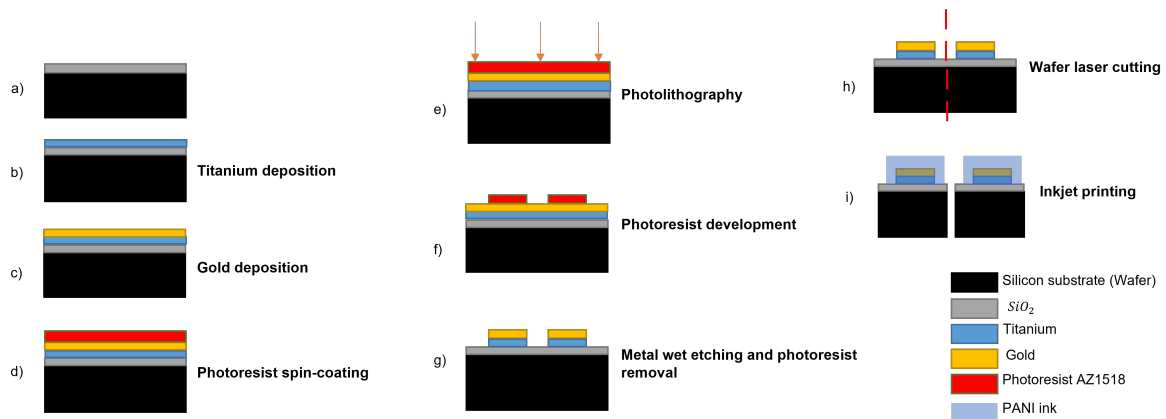


Fig. 3.1 Scheme of the device fabrication process.

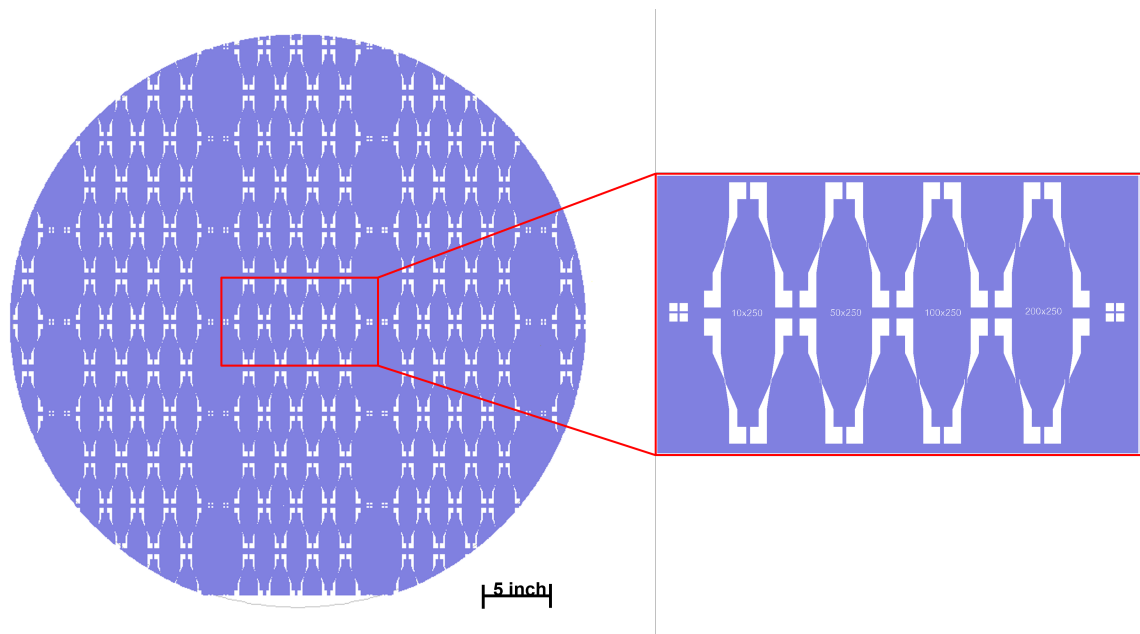


Fig. 3.2 On the left, 5x5 inch (1 inch=25.4 mm) UV mask of one of the geometries of interest, snapshot taken by CleWin software. On the right, a zoom on a single die. The violet parts are the ones subjected to the laser writing process or, in other words, the ones to be removed during the development step.

3.2 Inkjet printing optimization

In this section, the optimization of the inkjet printing process is discussed. Different key points were investigated and considered. First, the clogging problem and how to fix it. Then, the ink synthesis optimization was done, followed by the optimization of the inkjet printer setting parameters for the final devices. Their layout was optimized, so that the number of devices per chip could be enhanced.

3.2.1 The nozzle clogging: a resolute approach

A relevant problem arising from the inkjet printing process is the clogging of the nozzle: it happens when residual or precipitate in the ink solution is present and is deposited at the nozzle end. This is the reason why a cleaning procedure is strictly required, so that the inkjet printing is not interrupted and the quality of the results is not affected. The cleaning of both nozzle and fluidic channel are carried out manually, by disconnecting the nozzle from the printer and exploiting:

- a syringe;
- an adaptor used to connect the syringe to the nozzle;
- bakets for the waste and the solvent used for the cleaning, which is DiMethyl Sulfoxide (DMSO, the same in which PANI powder is dissolved for the synthesis of a printable ink solution).

Basically, the operation includes the flushing and back-flushing of DMSO through the nozzle, until it flows out by simply imposing a small pressure on the fluid. If everything is executed correctly, the cleaned orifice can be checked out at the optical microscope.

The ink preparation has been optimized to avoid the presence of precipitate in the solution aiming at minimizing the clogging issue. The optimized ink preparation protocol is reported in the following:

1. dissolution of PANI 100 KDa in DMSO;
2. filtering with PTFE (PolyTetraFluoroEthylene)-based filter pores size of 0.22 μm .

3.2.2 Ink characterization and optimization

PANI ink synthesis has to be considered as the starting line, since it influences dramatically the final results, in terms of both printing quality (the correct patterning, the drop ejection stability and so on) and device performances (ink conductivity). Thus, three different concentrations were tested, in order to verify the best one from the printability and device behaviour standpoint:

- concentration of $100 \mu\text{g}/\text{ml}$ ($100 \mu\text{g}$ of PANI per ml of DMSO);
- concentration of $250 \mu\text{g}/\text{ml}$ ($250 \mu\text{g}$ of PANI per ml of DMSO);
- concentration of $500 \mu\text{g}/\text{ml}$ ($500 \mu\text{g}$ of PANI per ml of DMSO).

Concentrations higher than $500 \mu\text{g}/\text{ml}$ resulted in the clogging of the nozzle and were therefore avoided.

The different inks were loaded into the inkjet printer. In order to assess the conductivity of the different inks, a preliminary test has been performed exploiting a different set of electrodes. These electrodes were fabricated following the protocol described in 3.1 and featured an interdigitated geometry, with a channel length and width corresponding to $L = 10 \mu\text{m}$ and $W = 9590 \mu\text{m}$ respectively, as shown in Fig. 3.3. The interdigitated geometry allowed performing electrical measurement also for the inks characterized by higher resistivity. In addition, plenty of these devices were already available at ChiLab.

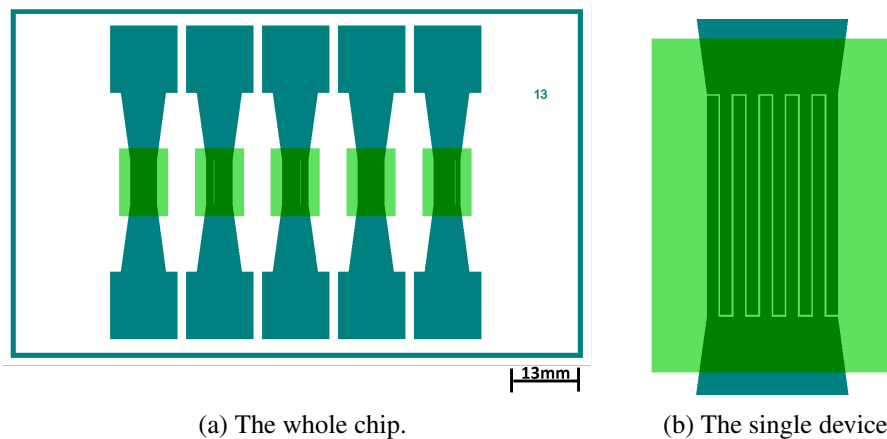


Fig. 3.3 Interdigitated devices used for the inkjet printing optimization, snapshot taken by CleWin software. The green rectangles are the patterns to be printed and the darker green ones refer to the gold electrodes.

The inkjet printing tests were executed starting from the lowest concentration to the highest one, followed by the subsequent electrical characterization of the devices.

After several preliminary attempts, the final inkjet printer parameters chosen for the ink concentrations are the ones reported in Table 3.1, while the voltage signals waveform are shown in Fig. 3.4.

Concentration ($\mu\text{g}/\text{ml}$)	100	250	500
Back-pressure (psi)	-6	-6	-8
Dwell Voltage (V)	-27	-30	-34
Echo Voltage (V)	27	30	34
Rise time (μs)	3	3	3
Fall time (μs)	3	3	3
Dwell time (μs)	10	10	10
Echo time (μs)	13	13	13
Spot margin (μm)	1	1	1
Spot spacing (μm)	40	30	50
Fly velocity (mm/s)	25	25	25

Table 3.1 Inkjet printer parameters settings for the three tested ink concentrations.

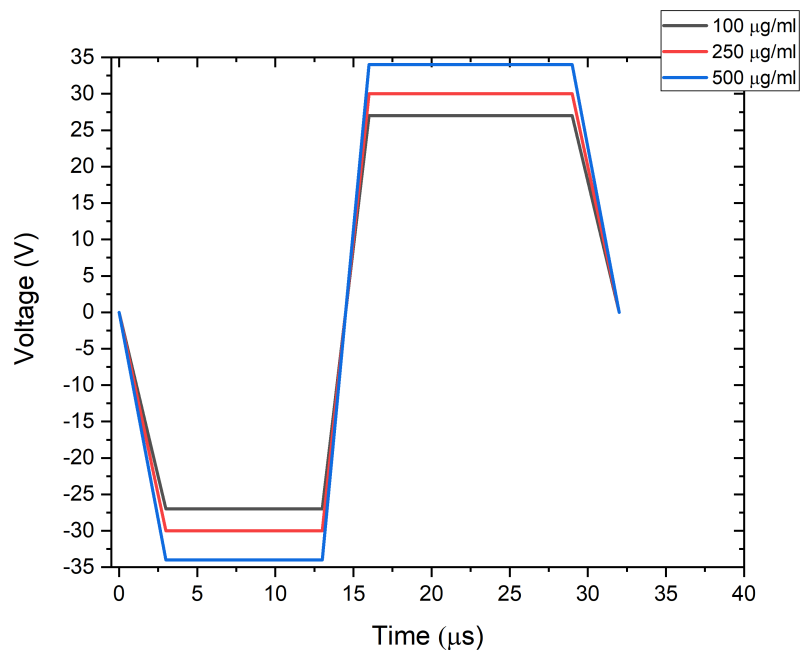


Fig. 3.4 The three signal waveforms used for the ink optimization tests. The black line refers to the signal used for 100 $\mu\text{g}/\text{ml}$ of ink concentration. The red and blue lines refer to 250 and 500 $\mu\text{g}/\text{ml}$ of ink concentration, respectively.

Five layers of PANI were printed, because the low concentration in the ink solution corresponds to a lower conductivity, and so a higher resistance within the devices channel. Moreover, the reason of this choice is also given by the possible increase of the so-called *percolative path*⁴: this latter is influenced by several parameters, here the most relevant ones are the concentration of PANI in DMSO and the number of layers per each device. A Field Emission Scanning Electron Microscope (FESEM) session was executed to investigate the morphology and distribution of the polymer printed on the channels (see Fig. 3.5, 3.6, 3.7 and 3.8): it was interesting to observe how the increase of polymer concentration in the ink solution corresponds to a greater presence of aggregates. In addition to this, for a given polymeric ink concentration, the higher the number of printed layers, the larger the percolative path and so the higher the channel conductivity. This is confirmed by the printing test executed with the concentration of 500 $\mu\text{g}/\text{ml}$, in which two and five PANI layers were printed on 20 interdigitated devices respectively (5 devices per single chip, so the total number of dies corresponds to 4 per each case). After that, in order to

⁴According to the percolation theory [100], when two conductive elements get in contact, an electron transfer can be observed. Therefore, if the conductive elements succession occurs continuously, a path allowing the electrical conduction can be evaluated.

prevent any contamination of the samples, their electrical characterization was carried out in cleanroom: to do this, the channel must be active, i.e. in a highly conductive state (low resistance state). As already explained in chapter 2, this can be achieved by PANI doping. This is done by immersing PANI in HCl 1 M solution for 2 minutes about, in order to pass from emeraldine base configuration to emeraldine salt one. After drying the samples, the channels resistance can be extracted from the $i-v$ characteristics. They were measured with a Keysight B2912A Source-Measure unit multimeter (see Table 3.2 and 3.3), sweeping the input voltage in the range of $[-0.5 \text{ } 0.5]$ V. The mean values of resistance as a function of ink concentration is shown in Fig. 3.9, the error bars represent the standard deviation obtained from a minimum of 19 devices, with an exponential decaying trend (linear trend in semi logarithmic scale). As shown in Fig. 3.10, the channel resistance decreases as the number of PANI layers increases. Therefore, the best solution is, in terms of conductivity, a ink concentration of $500 \mu\text{g/ml}$ with 5 printed PANI layers, needed for appreciable electrical performances.

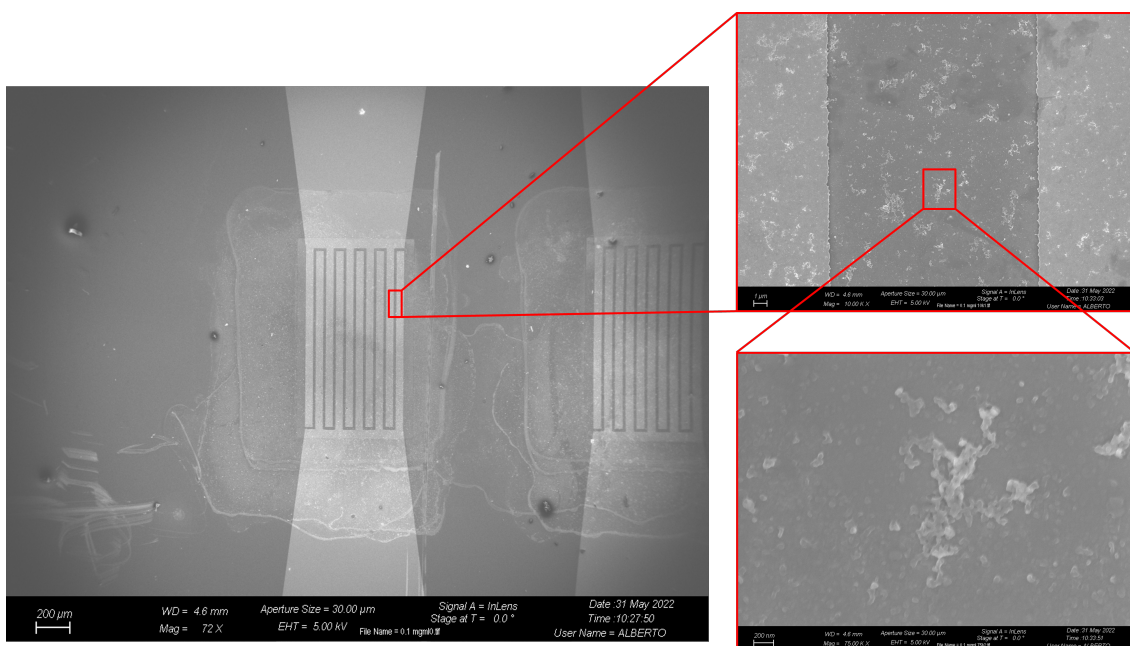


Fig. 3.5 FESEM pictures of tested interdigitated devices, PANI ink concentration of $100 \mu\text{g/ml}$. 5 printed layers. On the left, the single device. On the top-right, a zoom on the channel. On the bottom-right, PANI aggregate.

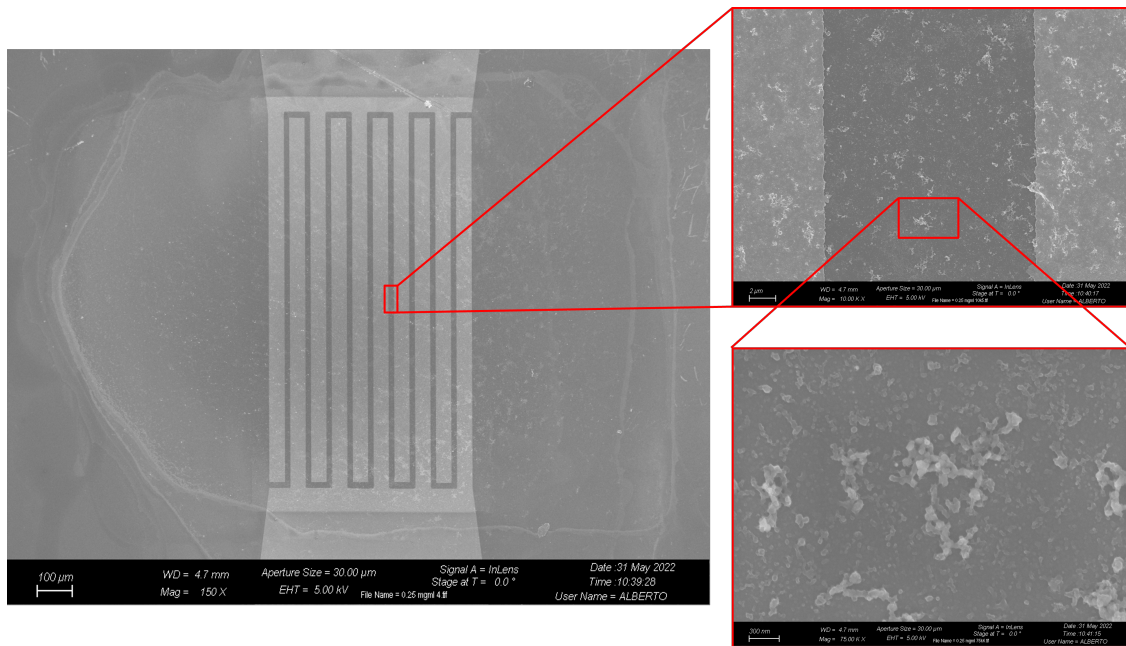


Fig. 3.6 FESEM pictures of tested interdigitated devices, PANI ink concentration of $250 \mu\text{g/ml}$. 5 printed layers. On the left, the single device. On the top-right, a zoom on the channel. On the bottom-right, PANI aggregate.

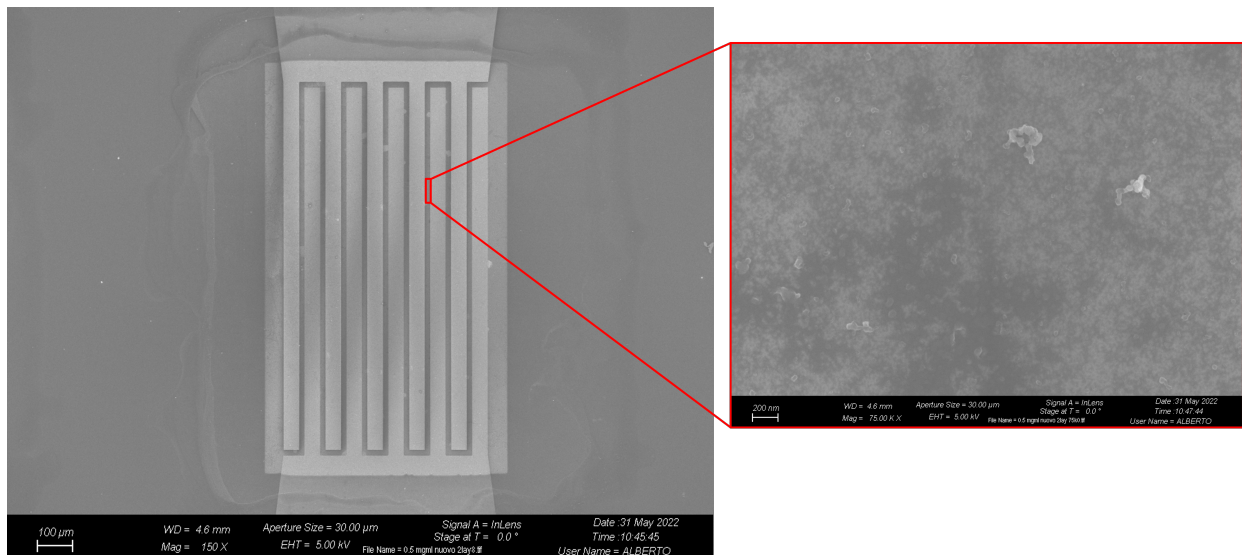


Fig. 3.7 FESEM pictures of tested interdigitated devices, PANI ink concentration of $500 \mu\text{g/ml}$, 2 printed layers. On the left, the single device. On the right, a zoom on the channel.

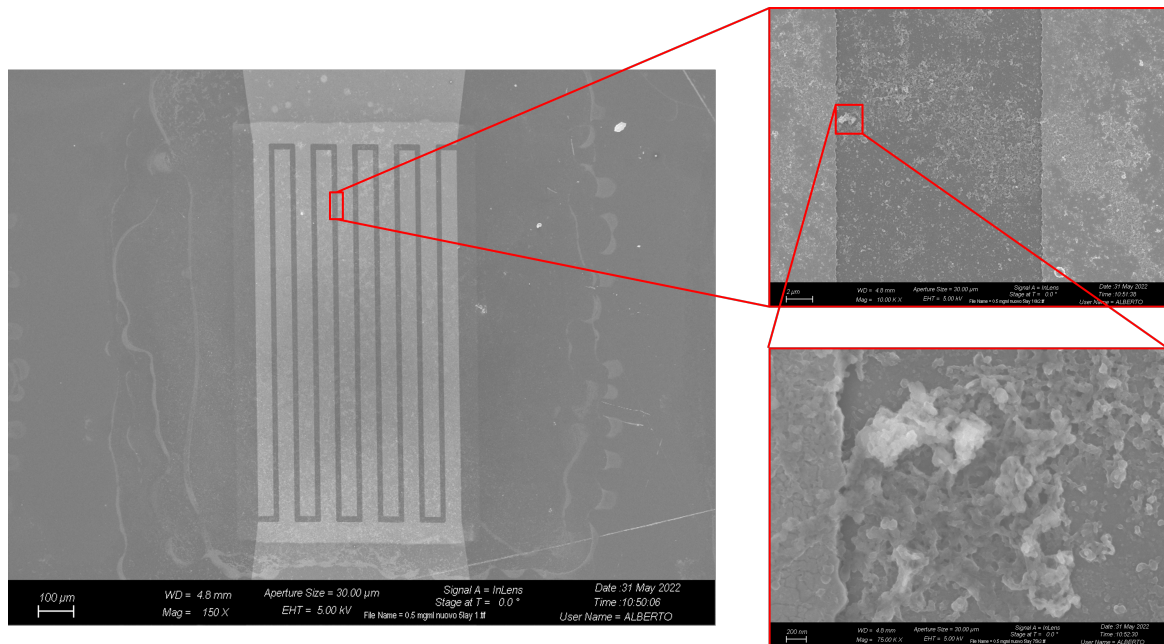


Fig. 3.8 FESEM pictures of tested interdigitated devices, PANI ink concentration of $500 \mu\text{g/ml}$, 5 printed layers. On the left, the single device. On the top-right, a zoom on the channel. On the bottom-right, PANI aggregate.

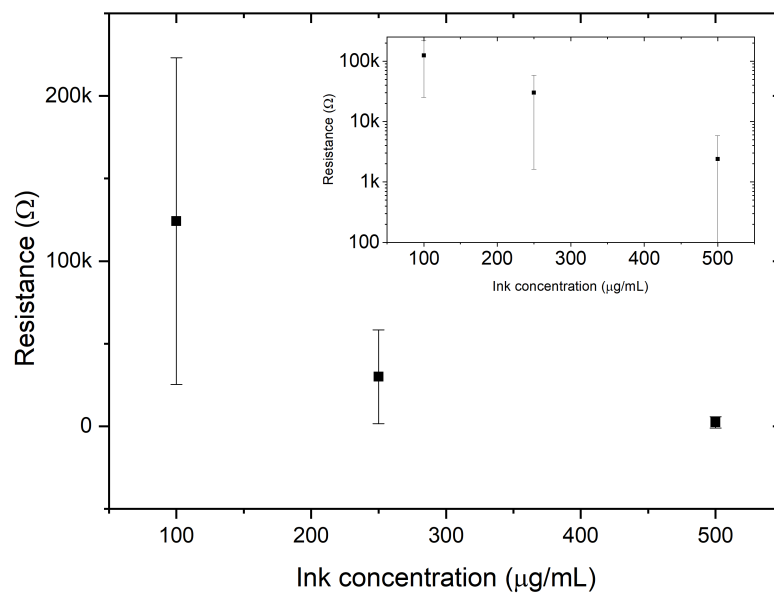
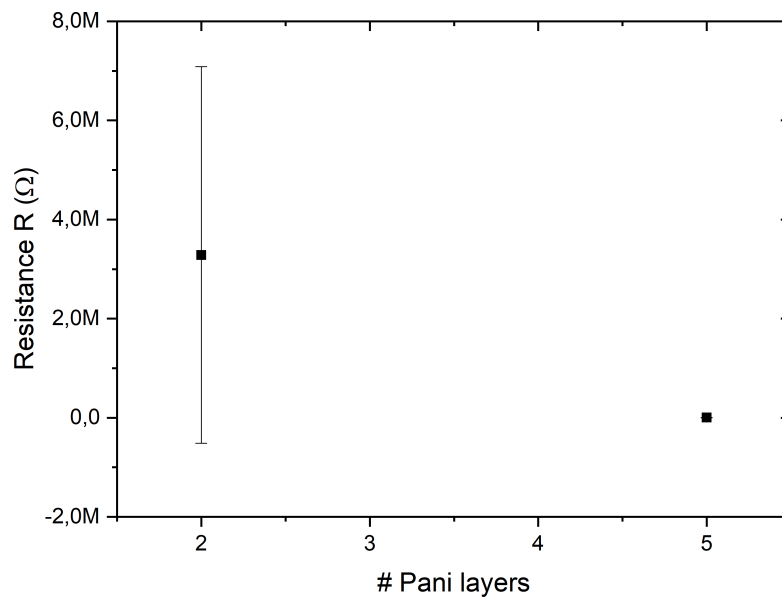


Fig. 3.9 Resistance as function of the ink concentration. Inset plot of the same graph in semi logarithmic scale. The printed layers are 5 in all the three cases.

Concentration ($\mu\text{g}/\text{ml}$)	100	250	500
R mean value (Ω)	$124,16 \cdot 10^3$	$29,99 \cdot 10^3$	$2,41 \cdot 10^3$
R standard deviation (Ω)	$98,92 \cdot 10^3$	$28,36 \cdot 10^3$	$3,42 \cdot 10^3$

Table 3.2 Resistance R values as function of the ink concentration.Fig. 3.10 Resistance as function of number of the printed PANI layers. PANI ink concentration of $500 \mu\text{g}/\text{ml}$.

# PANI layers	2	5
R mean value (Ω)	$2,66 \cdot 10^6$	$2,41 \cdot 10^3$
R standard deviation (Ω)	$221,52 \cdot 10^3$	$3,42 \cdot 10^3$

Table 3.3 Resistance R values as function of number of the printed PANI layers. PANI ink concentration of $500 \mu\text{g}/\text{ml}$.

3.2.3 Devices layout and printing optimization

Using the ink solution with PANI concentration of $500 \mu\text{g}/\text{ml}$, the inkjet printing can be executed on the final devices. As aforementioned, the chip layout was optimized, in order to obtain a greater number of devices on each chip and increase the throughput of the printing procedure itself. Furthermore, the accuracy of the data analysis resulting from the electrical characterization tests can be improved (see section 4.1 for the related description).

In Fig. 3.11, the "old" layout version and "new" one can be appreciated per each channel geometry configuration. The channel width W is fixed and the channel length L in each of the three configurations is changed:

- $W=250 \mu\text{m}$, $L=[10; 50; 100; 200] \mu\text{m}$, aspect ratio $\frac{W}{L}=[25; 5; 2.5; 1.25]$. From now on, for simplicity, they will be called here $w250$;
- $W=500 \mu\text{m}$, $L=[10; 50; 100; 200] \mu\text{m}$, aspect ratio $\frac{W}{L}=[50; 10; 5; 2.5]$. From now on, for simplicity, they will be called here $w500$;
- $W=2000 \mu\text{m}$, $L=[10; 50; 100; 200] \mu\text{m}$, aspect ratio $\frac{W}{L}=[200; 40; 20; 10]$. From now on, for simplicity, they will be called here $w2000$.

As a result, after the layout modification, the number of devices per single die is doubled, passing from 8 to 16 (Fig. 3.12). The devices, for simplicity, will be referred to numbers: for instance, devices with channel length $L=10 \mu\text{m}$ and width $W=[250; 500; 2000] \mu\text{m}$ will be called as *device 1-2-3-4*, while the ones with $L=50 \mu\text{m}$ and width $W=[250; 500; 2000] \mu\text{m}$ as *device 5-6-7-8*, $L=100 \mu\text{m}$ and width $W=[250; 500; 2000] \mu\text{m}$ as *device 9-10-11-12* and $L=200 \mu\text{m}$ and width $W=[250; 500; 2000] \mu\text{m}$ as *device 13-14-15-16*. On the same flow, the chips involved under study will be referred to numbers (i.e. *chip 1-2-3* and so on).

To optimize the inkjet printer parameters, in order to get a final exhaustive outcome, several attempts were done. The most significant spot parameters were changed, as summarized in Table 3.4. The old version of the geometries of interest, as well as the interdigitated devices, were exploited for the optimization of the printing parameters. The choice of spot parameters was done by considering the diameter sizes of the single drop, which can be measured as shown in Fig. 3.13. Non-optimized parameters resulted in not well defined and uniform patterns and in a more probable formation of satellites (Fig. 3.14).

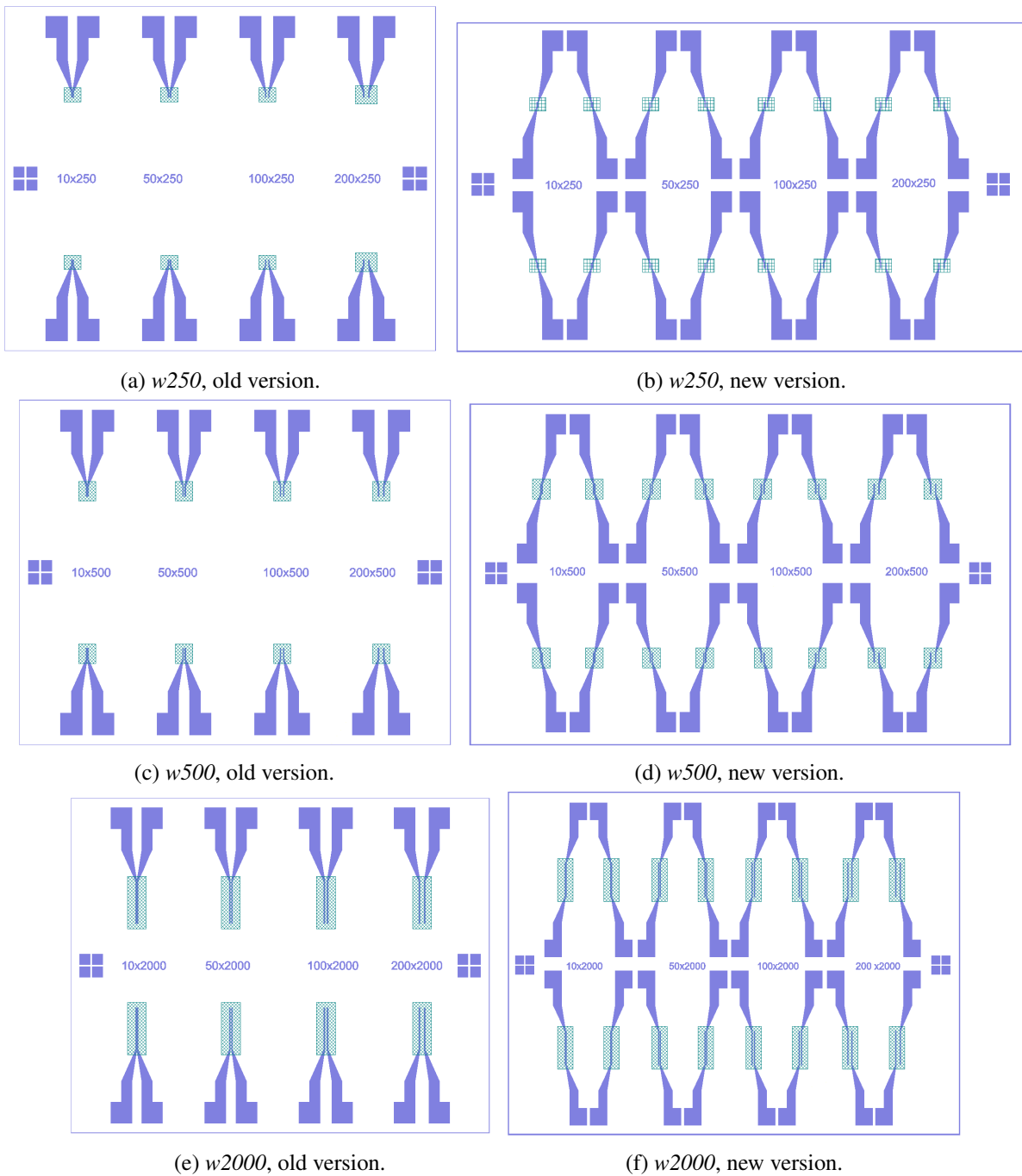


Fig. 3.11 Devices layout of a single die, snapshot taken from CleWin software. The violet parts refer to gold electrodes, while the green ones refer to the inkjet printed pattern.

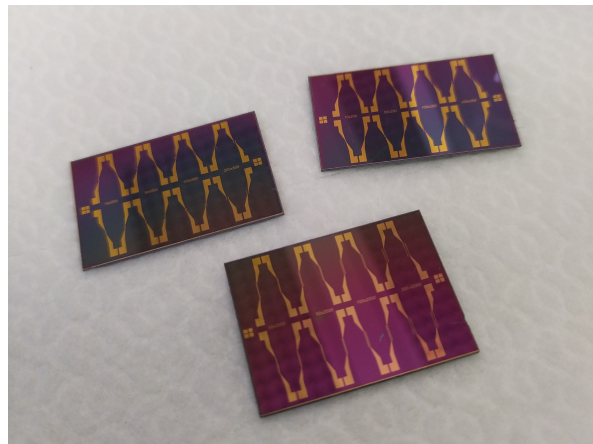


Fig. 3.12 The final devices. Notice that, after the fabrication process steps, a additional spin-coated resist is deposited in order to prevent them from undesired damages. This is the reason why the devices show a red surface. Before inkjet printing, the resist must be removed by washing the dies with acetone and isopropanol.

Test #	Spot margin (μm)	Spot spacing (μm)	Fly velocity (mm/s)	Results
1	50	120	25	Not uniform
2	50	100	35	Not uniform
3	50	75	15	Not uniform
4	25	75	25	Not uniform
5	25	50	25	Not uniform
6	1	50	25	Not uniform
7	1	50	25	Uniform
8	1	40	25	Not uniform
9	1	37.5	25	Not uniform
10	1	35	25	Uniform
11	1	32.5	25	Not uniform
12	1	30	25	Not uniform
13	1	27.5	25	Uniform
14	1	25	25	Not uniform

Table 3.4 Spot parameters optimization tests. The best results are the ones in the highlighted rows.

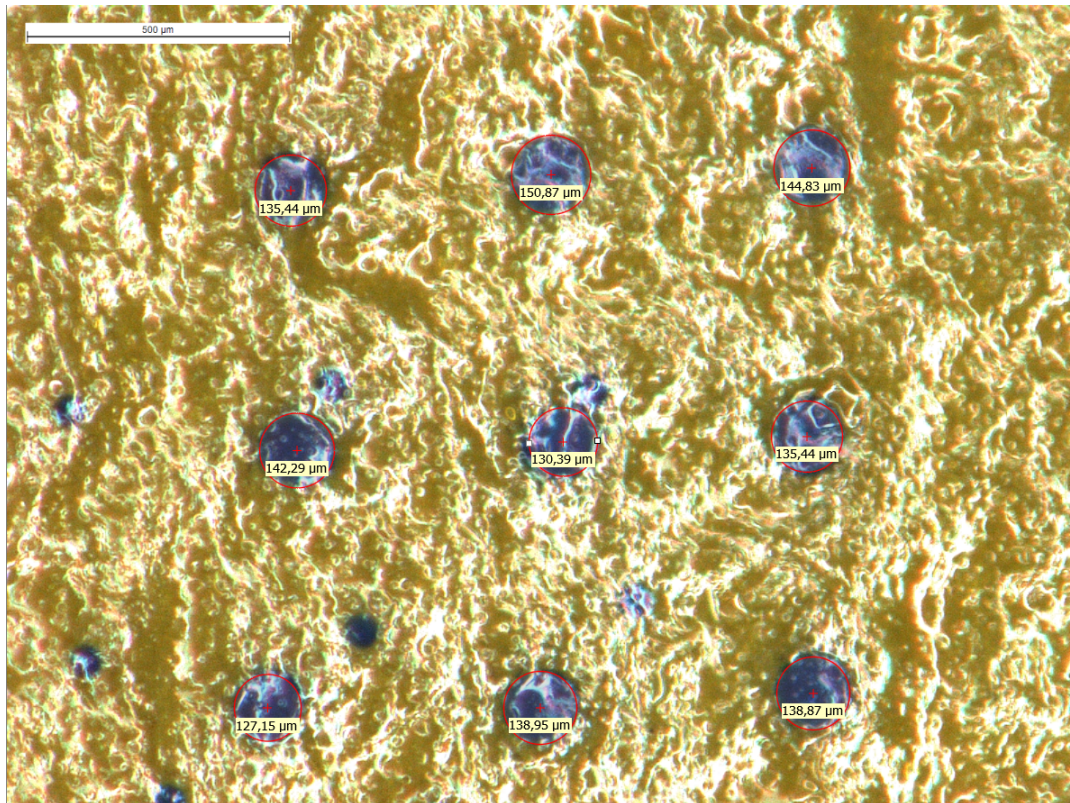
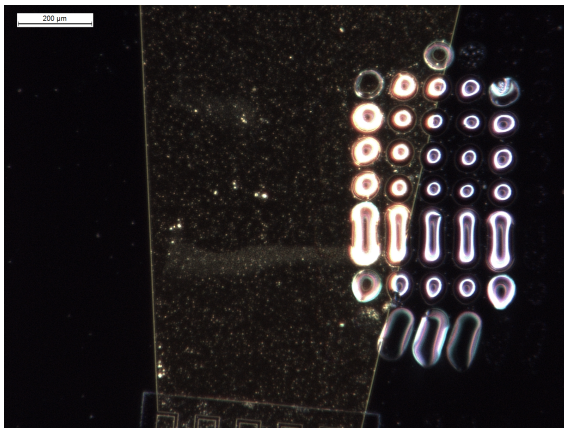
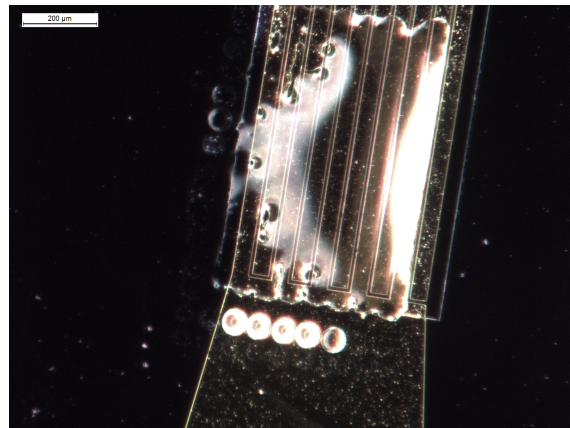


Fig. 3.13 PANI ink droplets measurement from a rectangular array printed on paper. Picture taken from optical microscope.

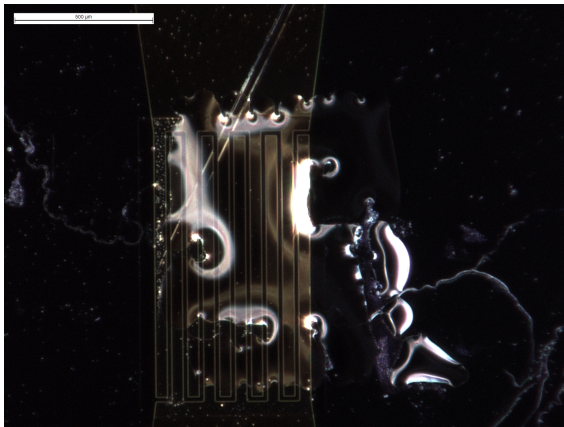
At this point, the signal waveform parameters have to be chosen properly, according to the geometry of interest, together with the spot parameters. Also here, a good trade-off had to be found, relying on a "trial and error" approach. In Table 3.5, the final signal parameters, used for the 3 geometries, are reported together with the spot ones. A graphical comparison of the bipolar waves is shown in Fig. 3.15. At the end of this optimization procedure, a good patterning was achieved (Fig. 3.16), without satellites and misalignment, so that the devices channel is covered completely and uniformly by the polymeric ink.



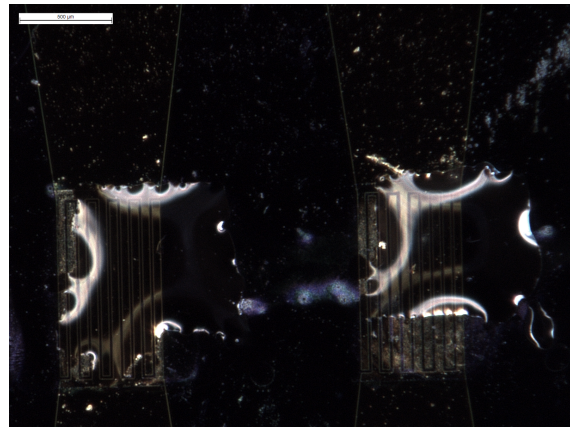
(a) Not uniform and completely misaligned pattern. Back-pressure, spot margin and spacing need to be improved.



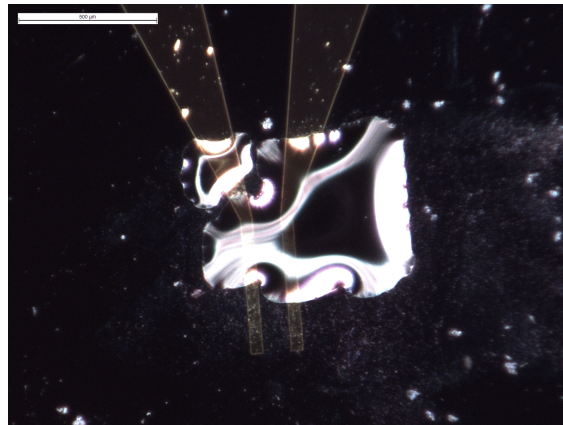
(b) Not perfectly uniform layer and well defined pattern.



(c) Not uniform layer and well defined pattern, likely due to a too large spot spacing.



(d) Not well defined pattern, wrong spot spacing and margin.



(e) Not uniform layer and imprecise pattern, due to a not optimal spot spacing.

Fig. 3.14 Examples of bad results, because of not optimal choice of inkjet printer parameters. Pictures taken from optical microscope.

Geometry	w250	w500	w2000
Spot parameters test #	10	13	7
Back-pressure (psi)	-10	-14	-6
Dwell Voltage (V)	25	26	26
Echo Voltage (V)	-25	-26	-25
Rise time (μs)	3	3	3
Fall time (μs)	3	3	3
Dwell time (μs)	11	10	15
Echo time (μs)	14	13	15

Table 3.5 Voltage signal waveform parameters used for the printing on the final devices, in combination with the best spot parameters tests.

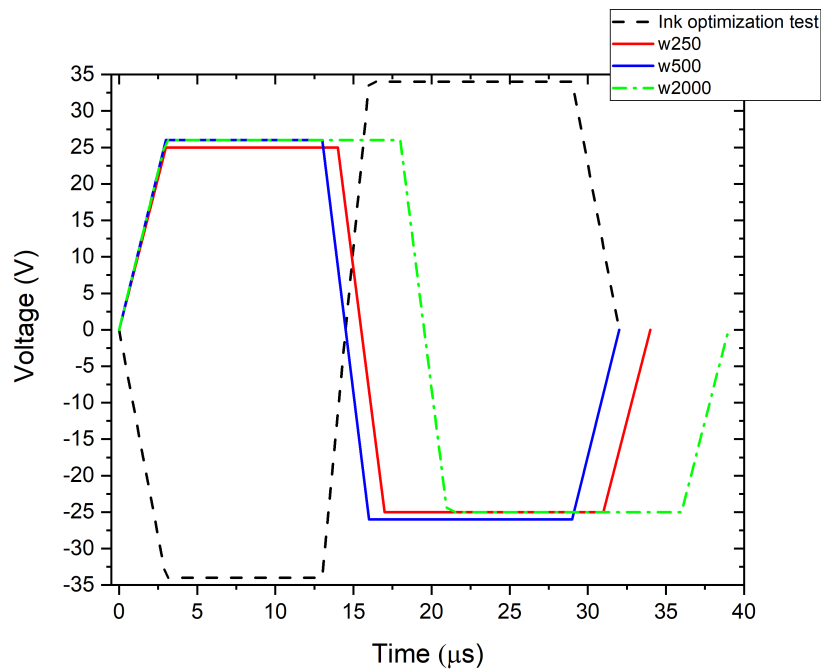


Fig. 3.15 Plot of the voltage signals for inkjet printing of the final devices, compared with the one used for the ink optimization test (concentration of $500 \mu g/ml$). The red line refers to the signal used for w250; the blue one to w500; the dashed-dot green one to w2000 and the dashed black one to the ink optimization test.

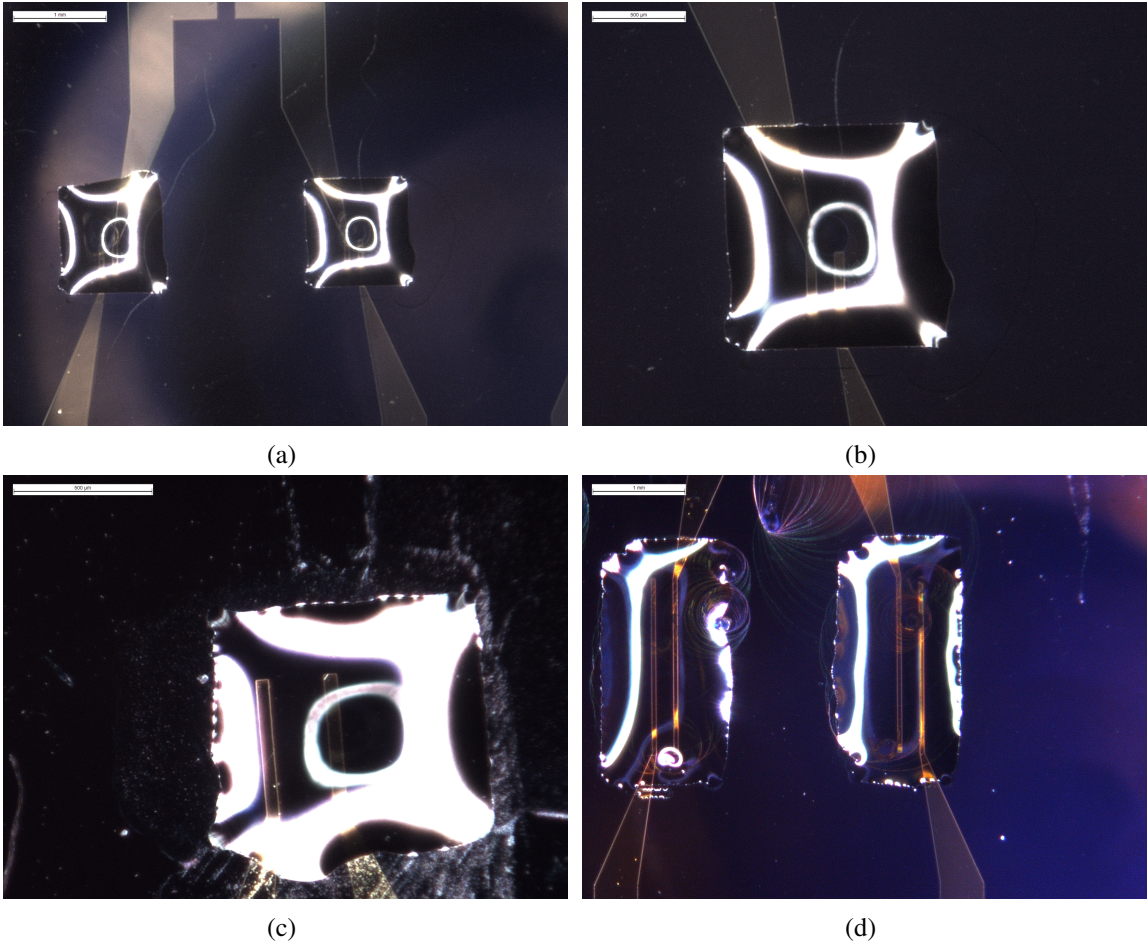


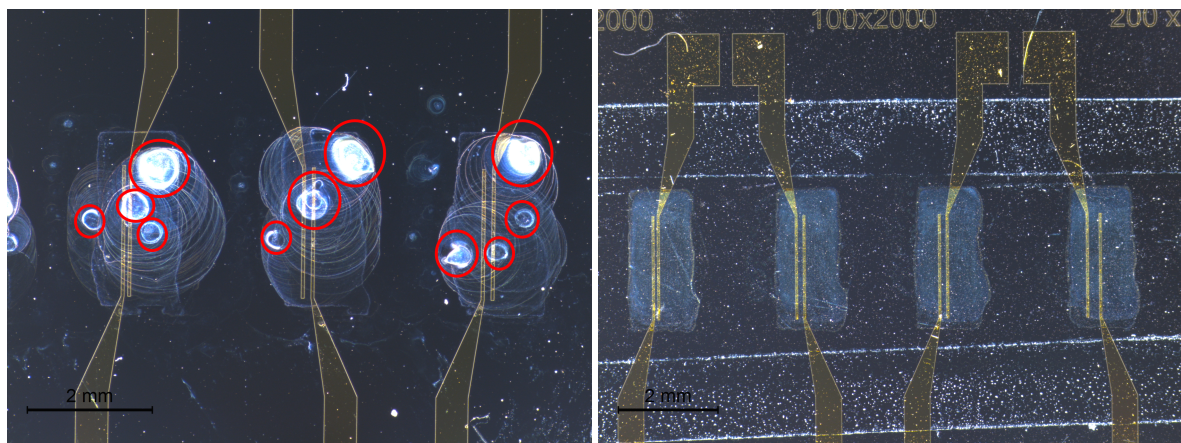
Fig. 3.16 The best patterning results, after the inkjet printing optimization tests. Pictures taken from optical microscope.

3.2.4 Morphological analysis

A further investigation was done in terms of the printed pattern drying. In this respect, two approaches were selected:

- a short drying procedure, where the samples were heated up to 80°C. The choice of the temperature is due to the following reasons. Firstly, PANI does not show significant weight losses at temperatures up to 120°C about, without affecting the polymer properties themselves [101]. Secondly, one has to consider the high boiling point of DMSO (at 189°C [102]), which requires time for the solvent evaporation;
- a long drying procedure, where the samples were left to dry at the ambient temperature (typically 25°C).

As shown in Fig. 3.17, one can observe how the printing results are dramatically influenced by the drying procedure. On the one hand, the short dry approach gets the drying process faster than the long one. On the other hand, the PANI volume is non-homogeneous: as a consequence of the fast solvent evaporation, evident ink lumps are formed (Fig. 3.17a).



(a) Zoom on some devices, short dry. PANI lumps highlighted by red circles.

(b) Zoom on some devices, long dry.

Fig. 3.17 Comparison between short and long dry procedures, *w2000* geometry. Pictures taken from optical microscope.

Furthermore, the area of the printed pattern in the two cases of study has been evaluated through *ImageJ*® software. These values were processed in order to get the mean value and the standard deviation, according to the aspect ratio of the devices channel and comparing the two drying procedures (see Table 3.6, 3.7 and 3.8). As summarized in Fig. 3.18, the printed area is larger in the short dry case than in the long dry one, as a result of the random motion of the solvent during its evaporation. Moreover, the greater error bars in this case justifies the greater variability of the evaluated areas and so the electrical performances, for the same device geometry, are meant to be not repeatable and really different from each other (see section 4.1). Furthermore, this morphological variability becomes more and more significant when the channel width increases, since for *w2000* devices the area to be printed is wider than in *w500* and *w250* ones. Therefore, the short dry effects become more and more evident with larger channel sizes. Instead, the long dry approach results in lower printed area, with more repeatable values (justified by a smaller error bar) and a more stable trend in the plot.

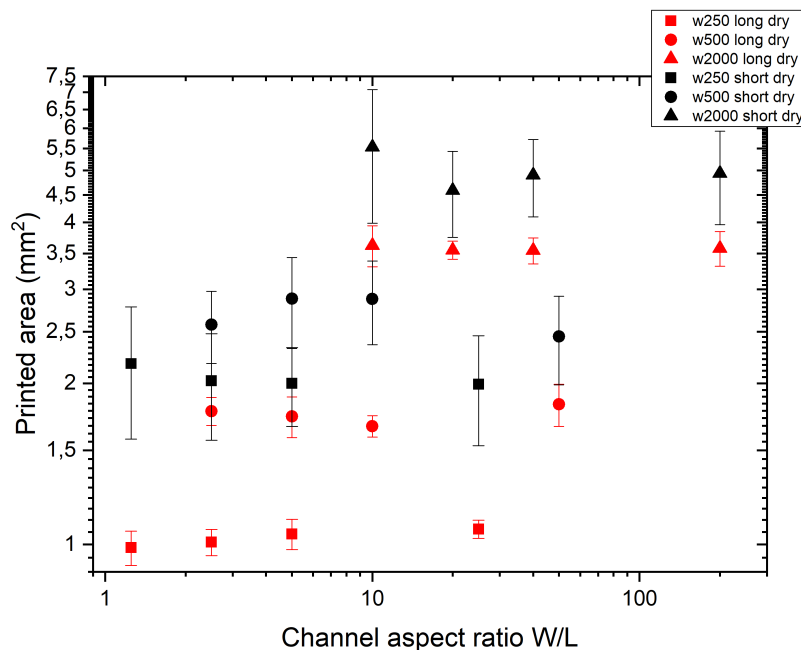


Fig. 3.18 Printed area as function of the channel aspect ratio, comparison between short dry procedure (in black) and long dry one (in red). The graph is reported in logarithmic scale.

Aspect ratio $\frac{W}{L}$	25	5	2.5	1.25
A mean value (mm^2), short dry	1.993	1.999	2.022	2.178
A standard deviation (mm^2), short dry	0.463	0.336	0.456	0.604
A mean value (mm^2), long dry	1.068	1.047	1.011	0.987
A standard deviation (mm^2), long dry	0.042	0.068	0.0057	0.073

Table 3.6 Printed area A values for $w250$ geometry, a comparison between short dry and long dry procedures. In both cases, the number of devices under test is 12 per each aspect ratio (the number of chips corresponds to 3).

Aspect ratio $\frac{W}{L}$	50	10	5	2.5
A mean value (mm^2), short dry	2.449	2.876	2.882	2.576
A standard deviation (mm^2), short dry	0.462	0.511	0.555	0.396
A mean value (mm^2), long dry	1.828	1.664	1.736	1.774
A standard deviation (mm^2), long dry	0.165	0.076	0.151	0.107

Table 3.7 Printed area A values for $w500$ geometry, a comparison between short dry and long dry procedures. In both cases, the number of devices under test is 12 per each aspect ratio (the number of chips corresponds to 3).

Aspect ratio $\frac{W}{L}$	200	40	20	10
A mean value (mm^2), short dry	4.940	4.903	4.590	5.532
A standard deviation (mm^2), short dry	0.981	0.809	0.837	1.548
A mean value (mm^2), long dry	3.577	3.545	3.552	3.624
A standard deviation (mm^2), long dry	0.266	0.198	0.139	0.319

Table 3.8 Printed area A values for $w2000$ geometry, a comparison between short dry and long dry procedures. In both cases, the number of devices under test is 12 per each aspect ratio (the number of chips corresponds to 3).

Chapter 4

Results and discussion

In this chapter, the results of the electrical characterization tests, executed at CNR-IMEM on the fabricated devices, are described. Moreover, the behaviour of short-dried and long-dried samples is compared, underlining their differences. Finally, the definition of neuromorphic properties is reported from biology and the results of the related tests on organic memristive devices are summarized.

4.1 Electrical characterization

4.1.1 Experimental setup

The final part of this activity was carried out at CNR-IMEM in Parma and consisted in the electrical characterization of the devices under study.

The experimental setup is shown in Fig. 4.1: micromanipulators were used to contact the two gold electrodes of the organic memristive device, namely the drain and source terminals. The drain contact (i.e. the top metal pad, see Fig. 4.2) is connected to the power supply, while the source is grounded (i.e. the bottom metal pad, see Fig. 4.2), closing the circuit. It is worth noticing that these measurements are performed in liquid electrolyte, through *ad hoc* LabView® codes controlling the electrical test set up (National Instruments®PXIe-1073 and two Source Measure Unit (SMU) PXIe-4139 and PXIe-4138). The electrolyte here is, as already explained in chapter 2, *HCl* 1 M. For the correct working mechanism of these devices, a third electrode is needed for the measurements and it is a *reference* electrode, or also called gate, characterized by a silver wire. Proper chambers, made of Polydimethylsiloxane (*PDMS*), were realized to confine the electrolyte to the devices channels. Basically, these chambers were fabricated by starting from a mold, which is obtained by a Plexiglass (*PMMA*) layer, submitted to a LASER marker slider machine, available at ChiLab, in order to get the mold shape. DOW SYLGARD 184 *PDMS* is obtained by mixing the elastomer with the cross-linker, with a 10:1 ratio. After that, the liquid *PDMS* is deposited in the mold and annealed in a oven at 90°C for 2-3 hours. In the meanwhile, the dies are put on a heating plate at 80°C for some minutes. Finally, the chambers are attached on the dies surface, using *PDMS* as a pasting material and performing a further annealing either on the heating plate or in a oven at 90°C for 1 hour. As a result, the channels can be exposed to the electrolyte and the gate contact can be dipped in it, positioning the wire at a certain distance from the channel, in order to avoid any contact with PANI.

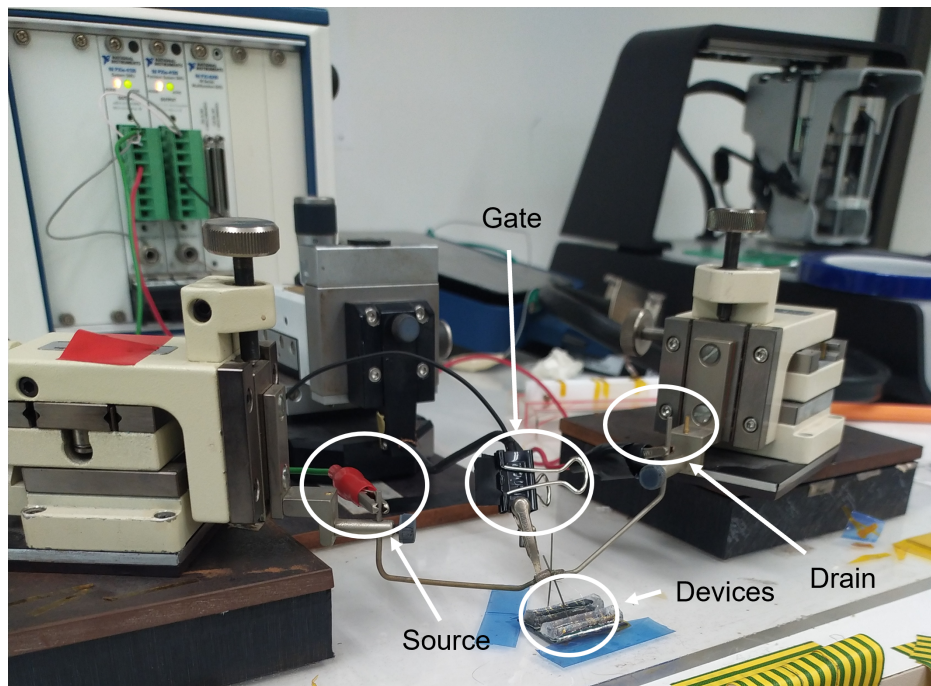


Fig. 4.1 Experimental setup of the electrical characterization tests.

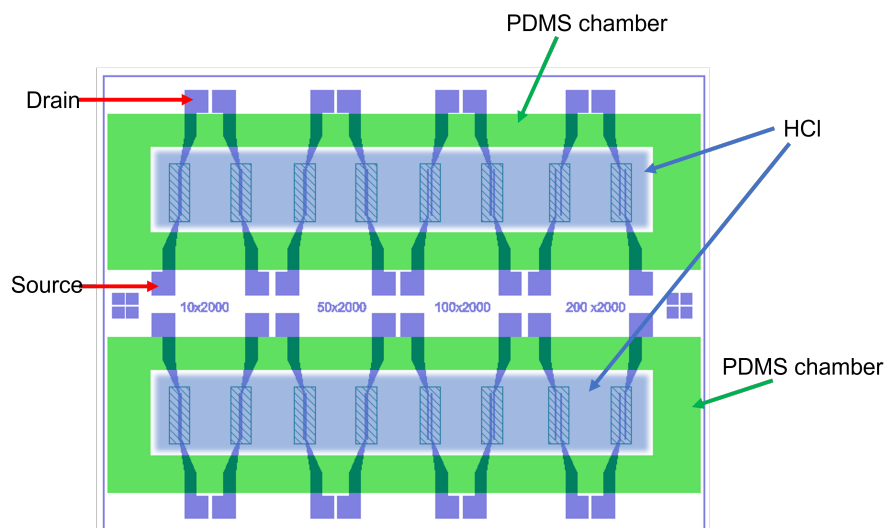


Fig. 4.2 Drain and Source contacts positions on the square metal pads (violet colour refers to gold). The green rectangles refer to *PDMS* chambers, while the blue ones refer to *HCl*. Snapshot adapted from CleWin software.

4.1.2 Hysteresis

Once the device is connected to the instrumentation, the measurements can start. The first element that can be analyzed is the hysteresis loop in the i - v characteristics. The stimulus provided by the instrumentation is a triangular voltage sweep between source and drain V_{DS} . The instrumentation returns the plot of the current flowing between drain and source I_{DS} (Fig. 4.3) and the one from the gate I_G . I_{DS} includes both electronic and ionic current contributions. I_G , instead, represents the ionic contribution only due to the polymer redox reactions [10]. In fact, for the latter, one can observe the presence of two current peaks, one positive and one negative (Fig. 4.4). The first one corresponds to the point for which the PANI oxidation rate is maximum (i.e. the channel is switched on), while the second one corresponds to the point for which the PANI reduction rate is maximum (i.e. the channel is switched off).

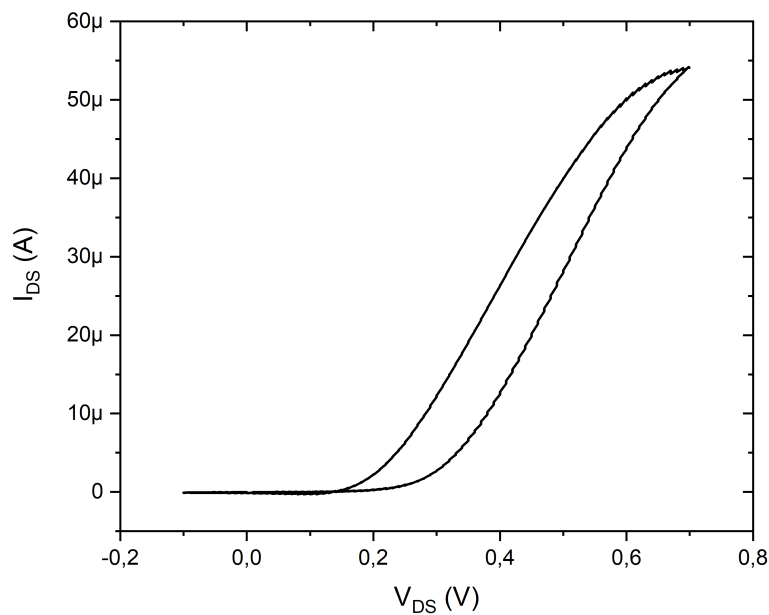


Fig. 4.3 Example of a I_{DS} - V_{DS} curve. Short dried device, $W \times L = 250 \times 10$. Scan rate at 50 mV/s.

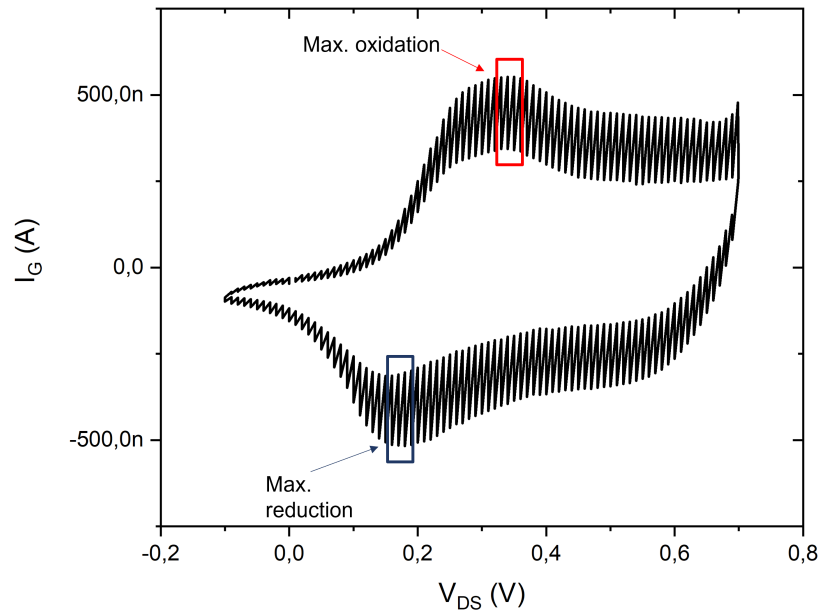


Fig. 4.4 Example of a I_G - V_{DS} curve. Short dried device, $W \times L = 250 \times 10$. Scan rate at 50 mV/s.

However, these data cannot provide information about the electrical conduction in the channel. This is the reason why, in order to get only the electronic current contribution flowing in the device channel, the difference between I_{DS} and I_G is evaluated: it is the so called *differential current* I_{diff} .

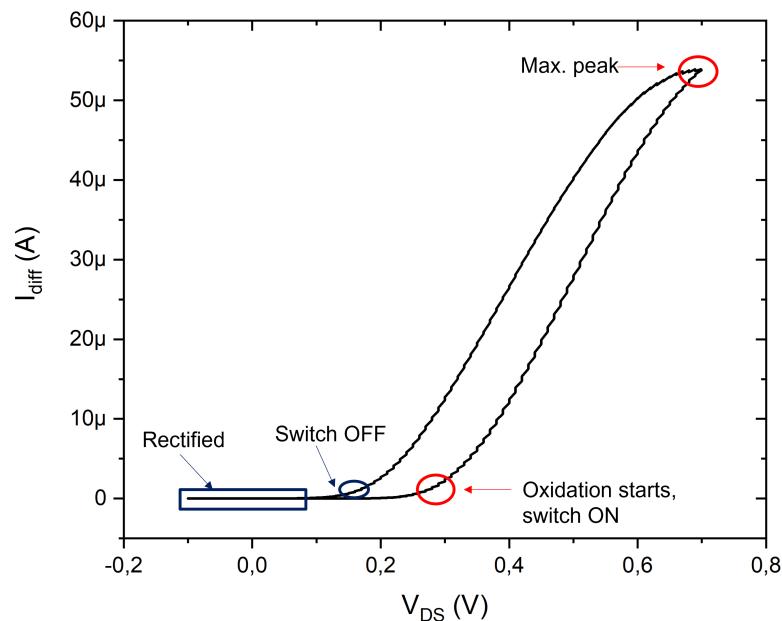


Fig. 4.5 Example of a I_{diff} - V_{DS} curve. Short dried device, $W \times L = 250 \times 10 \mu m$. Scan rate at 50 mV/s.

As one can see in Fig. 4.5, a hysteresis loop is present: I_{diff} evolution provides information about what happens to the polymer when a voltage drop is applied. At $V_{DS} = 0$ V, the voltammetric cycle starts. Up to 0.2-0.25 V, there is very low conduction: the polymer is still in its insulating form (leucoemeraldine) and a rectified trend of the current is dominant. The situation changes around 0.3 V, where the conduction increases up to a maximum value at 0.7 V. There, from the electrochemical point of view, the polymer is oxidizing. The sweep does not go over this voltage value, otherwise PANI becomes again insulating, since it assumes the pernigraniline form and the resistance values increases again, lowering the current. Afterwards, the voltage starts to decrease and the channel conductance gets lower and lower. Once the voltage drop goes below 0.2 V about, the polymer behaves again like an insulator. The minimum value chosen for the voltage sweep in these tests is -0.1 V, so that the memristive device can achieve a high resistance state and be completely switched off. Comparing the electrical behaviours, twin devices obtained with different drying procedures behaves similarly on each other (Fig. 4.6): the hysteresis loop is located in the positive range of the graph and a well defined rectification is present in the negative one, the switch on occurs around 0.3 V and the switch off around 0.2 V. These trends are in agreement with already reported devices realized by means of Langmuir-Schaefer techniques [103] suggesting that inkjet method is a valid deposition technique for realizing

organic memristive devices. The main difference is in the conduction order of magnitude, which varies according to the device and the dry procedure.

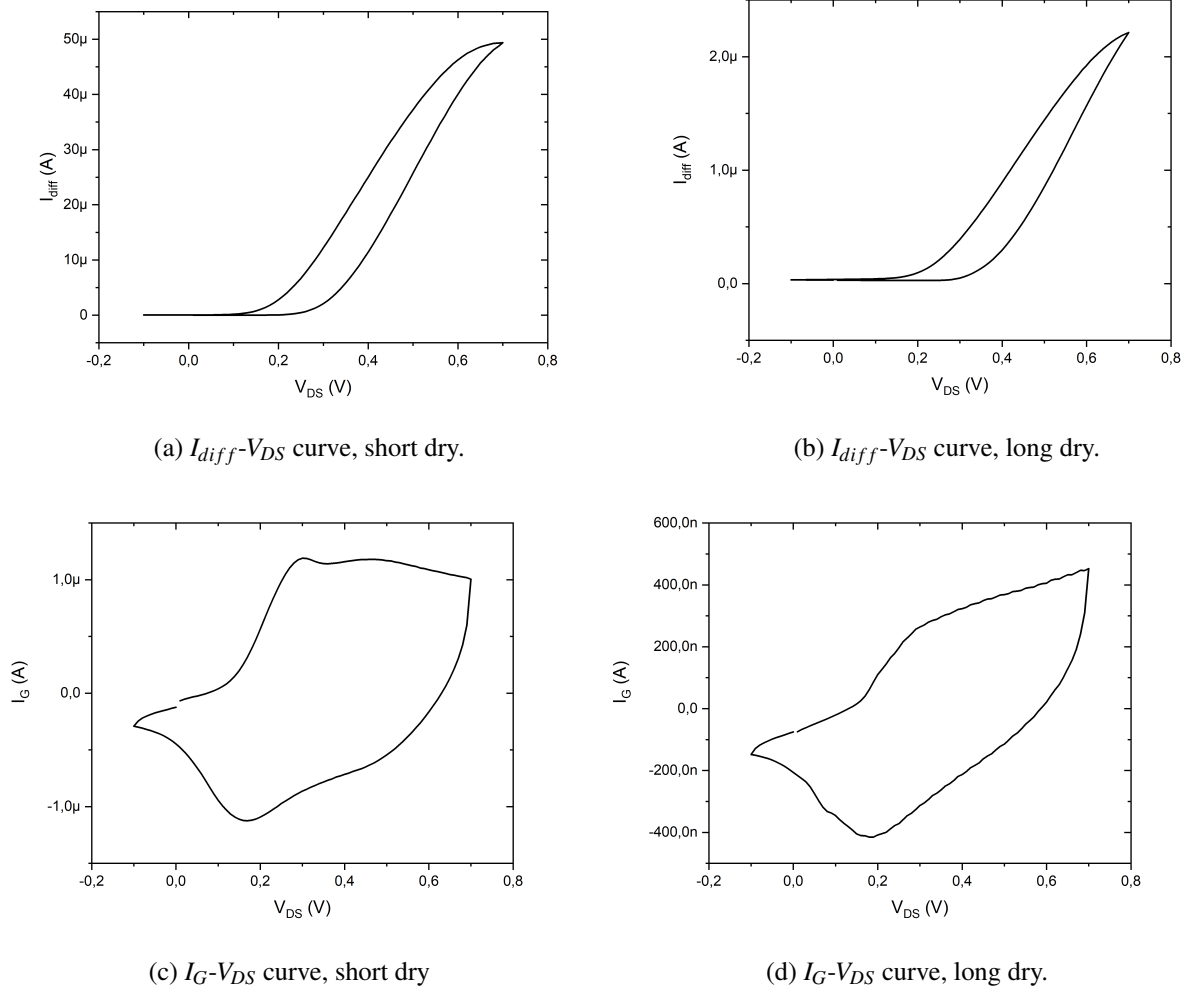


Fig. 4.6 $W \times L = 250 \times 10 \mu m$. Scan rate at 200 mV/s.

The stimulus can be provided with different *scan rates*: the scan rate is the velocity (and so the working frequency) at which a single voltage point is applied during the sweep or, in other words, a single corresponding current value is acquired. It is measured in mV/s . The higher the scan rate, the faster the acquisition. However, the acquisition frequency plays a significant role in the channel response. In this respect, for each device on a single chip and per each geometry, as well as for both drying procedure cases, the hysteresis curves were acquired at 3 different scan rates:

- 10 voltammetric cycles at 200 mV/s ;
- 3 voltammetric cycles at 100 mV/s ;
- 5 voltammetric cycles at 50 mV/s .

More than one cycle on the same device was needed to get the channel response stable. Decreasing the scan rate, the values of the differential current get higher (Fig. 4.7), because a slower acquisition allows PANI to have more time for the redox reaction. In fact, by looking at the ionic current (Fig. 4.8), the area defined by the hysteresis loop is wider at higher scan rates. It is associated with the combination of two factors: i) *pseudocapacitance*⁵ of the polymer, its capability to store charge during the redox reaction with the electrolyte and ii) the size of the diffusion layer above the PANI surface depending upon the voltage scan rate used⁶. From a mathematical point of view, the larger the scan rate, the lower the ionic current intensity and larger is the differential current, since it is difference between I_{DS} and I_G , is expected to be lower for larger scan rates. This demonstrates how the electrochemical properties of the polymer influence significantly the electrical response of the organic memristor.

⁵Conducting polymers are able to store charge through the switching between two doping states, p-doping and n-doping respectively, according to the presence or not of electrolyte ions in the backbones of the polymer. During oxidation (p-doping, charging process), the polymer becomes polycation and attracts electrolyte anions to intercalate into the backbone for charge neutrality conditions. During reduction (n-doping, discharging process), the polymer becomes polyanion and is doped with electrolyte cations [104].

⁶During a slow voltage scan the diffusion layer will grow much further from the polymer in comparison to a fast scan, generating a smaller flux and a smaller current to the electrode surface.

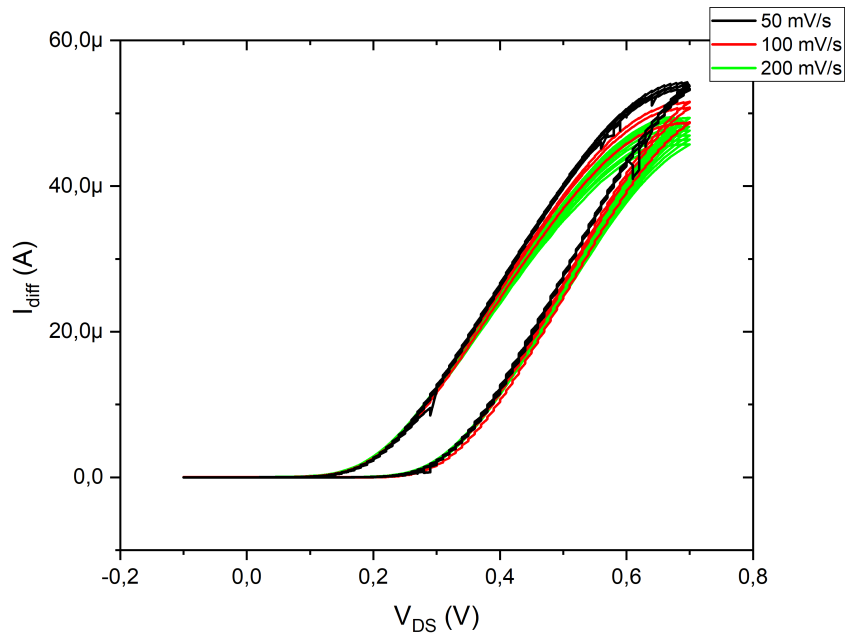


Fig. 4.7 Example of a I_{diff} - V_{DS} curve at different scan rates. Short dried device, $W \times L = 250 \times 10 \mu m$.

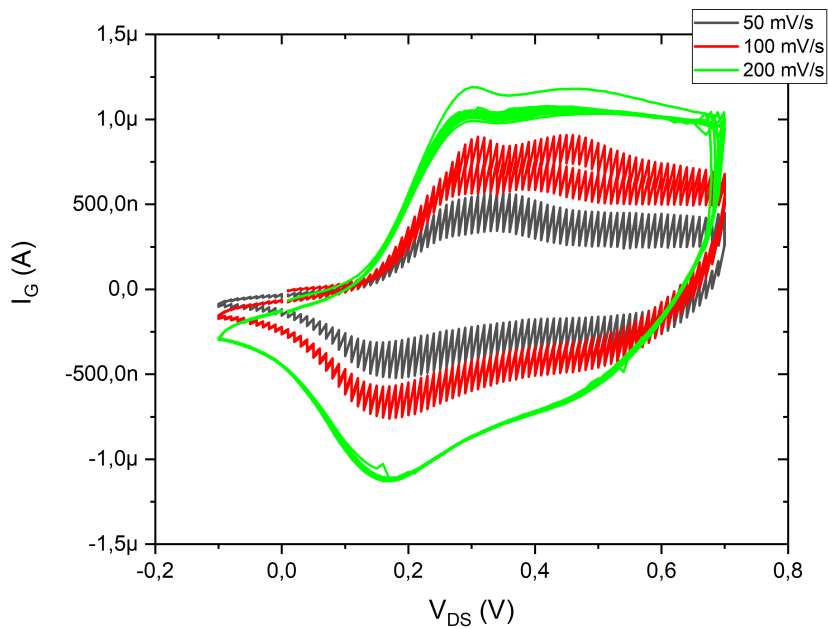


Fig. 4.8 Example of a I_G - V_{DS} curve at different scan rates. Short dried device, $W \times L = 250 \times 10 \mu m$.

Another item to be considered is the geometry factor. To this aim, a comparison can be done from the extraction of the minimum and maximum value of conductance from the hysteresis of the $I_{diff}-V_{DS}$ curves. The minimum conductance G_{min} was evaluated in the range of 0.05-0.2 V, while the maximum one G_{max} in the range of 0.5-0.6 V. For a single device, the mean value and the standard deviation was computed over the number of the voltammetric cycles per each scan rate. In Fig. 4.9, a typical behaviour is reported. G_{min} and G_{max} values show a stable trend as function of the scan rate and the gap between the two conductance (or resistance) states is almost constant. This means that the device is stable for different stimulus frequencies.

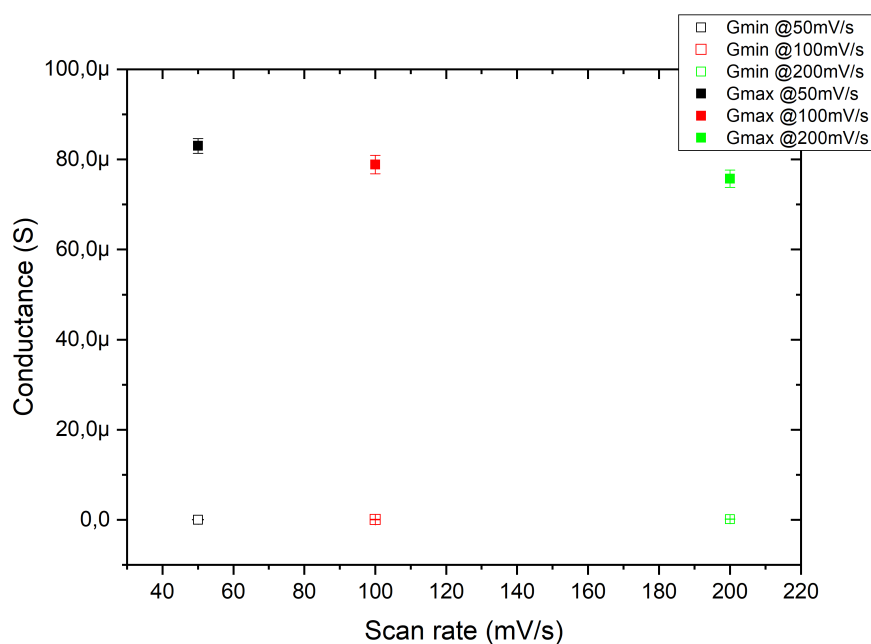


Fig. 4.9 Example of G_{min} and G_{max} at different scan rates. Short dried device, $W \times L = 250 \times 10 \mu m$.

However, it is worthwhile to mention that devices with same channel aspect ratio may develop quite different $i-v$ (an example is illustrated in Fig. 4.10) characteristics probably due to the short dry procedure that, as already discussed in subsection 3.2.4, may affect dramatically the PANI channel formation. In fact, as summarized in Fig. 4.11, comparing the mean values of the G_{max} for device obtained with long and short drying procedure, it's clearly visible that these latter show the larger variability of electrical performances. This observation suggests a close connection between the variability of PANI volume and the variability of the electrical performances, expressed by wide error bar in the graph. The predictable geometry factor incidence is shown in Fig. 4.12a-b-c. At fixed channel width but varying the channel length, the performances of

long dried devices change drastically. In addition, one expected devices with $\frac{W}{L} = 200$ as the most performing ones: the reasons why a lower conduction is observed in this case (Fig. 4.13) may be due to either the polymer aging or the different polymeric chains organization along the channel during the dry phase. In this respect, investigations are still under study. An evident difference can be seen in Fig. 4.14, where twin devices (shortly and longly dried) are compared. According to these considerations, the short drying procedure influences negatively the device behaviour and an unpredictable trend can be observed from the maximum conductance G_{max} values as function of the channel aspect ratio $\frac{W}{L}$. In the case of long dry approach, instead, the conductance values extracted from the I_{diff} - V_{DS} curves are more repeatable and, as expected, the conduction increases with the channel aspect ratio.

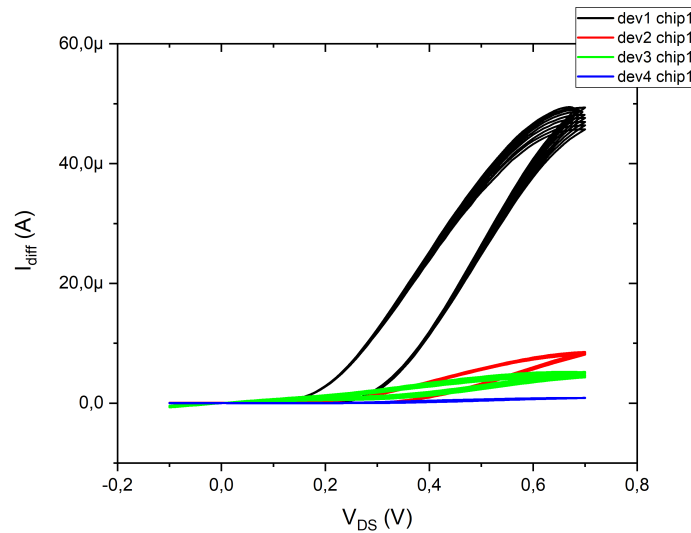


Fig. 4.10 I_{diff} - V_{DS} curves of devices with channel geometry $W \times L = 250 \times 10 \mu m$, at scan rate of 200 mV. Short dry procedure case.

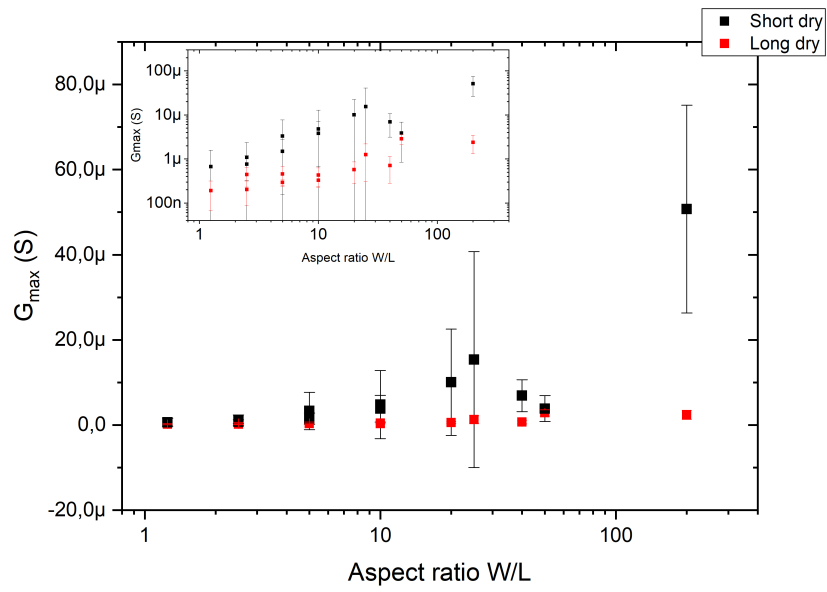
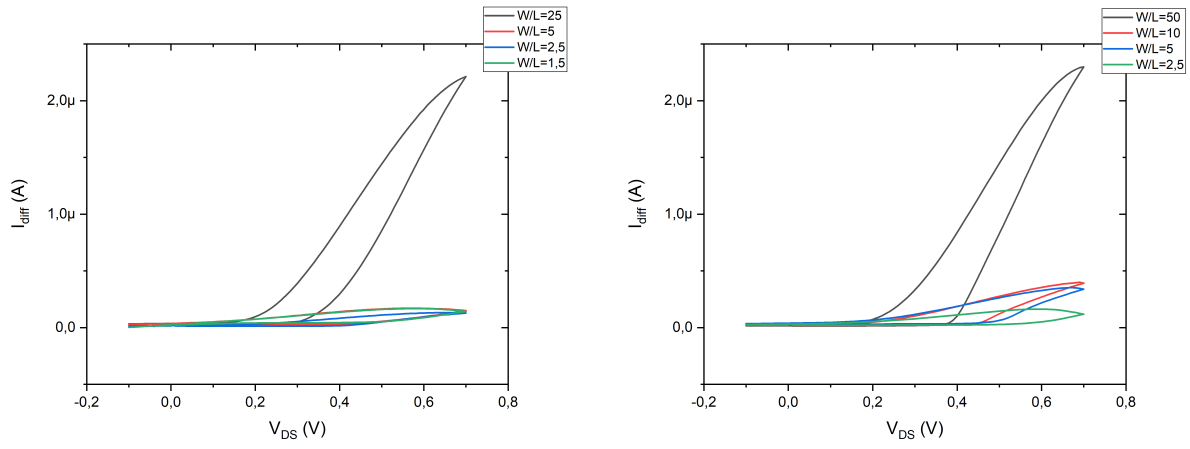
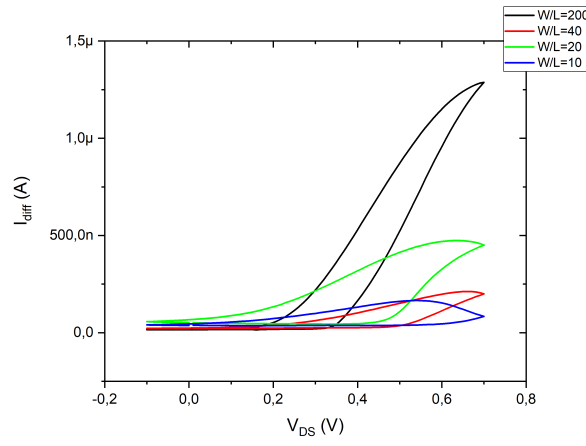


Fig. 4.11 G_{max} mean values extracted from the hysteresis curves, as function of the channel aspect ratio $\frac{W}{L}$. Short dry vs long dry procedure. Scan rate at 200 mV/s. Main graph in semi logarithmic scale, inset graph in logarithmic scale.

(a) $w250$.(b) 500 .(c) 2000 .Fig. 4.12 $I_{diff} - V_{DS}$ hysteresis curves, comparison among long dried devices.

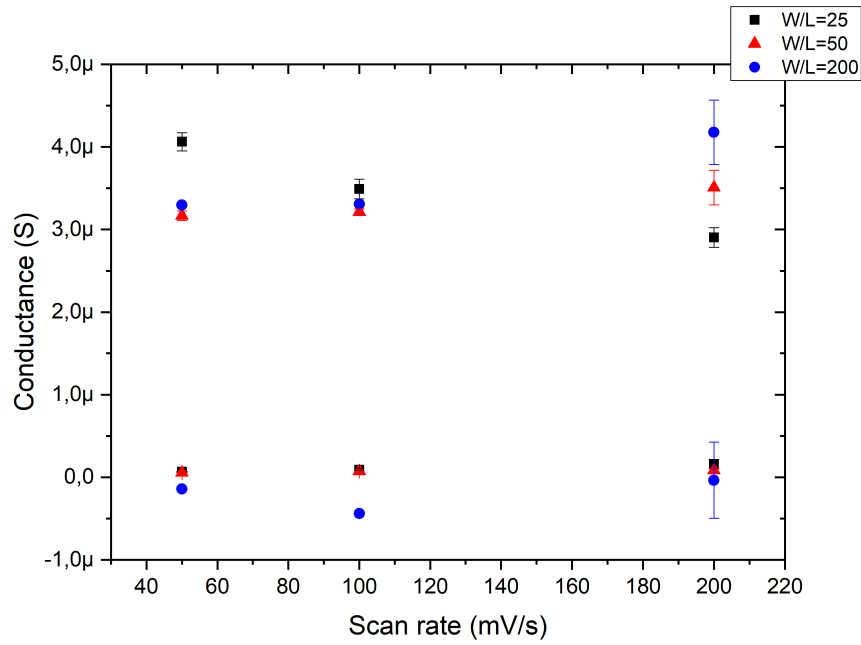


Fig. 4.13 G_{min} and G_{max} at different scan rates, comparison among long dried devices with the highest aspect ratio.

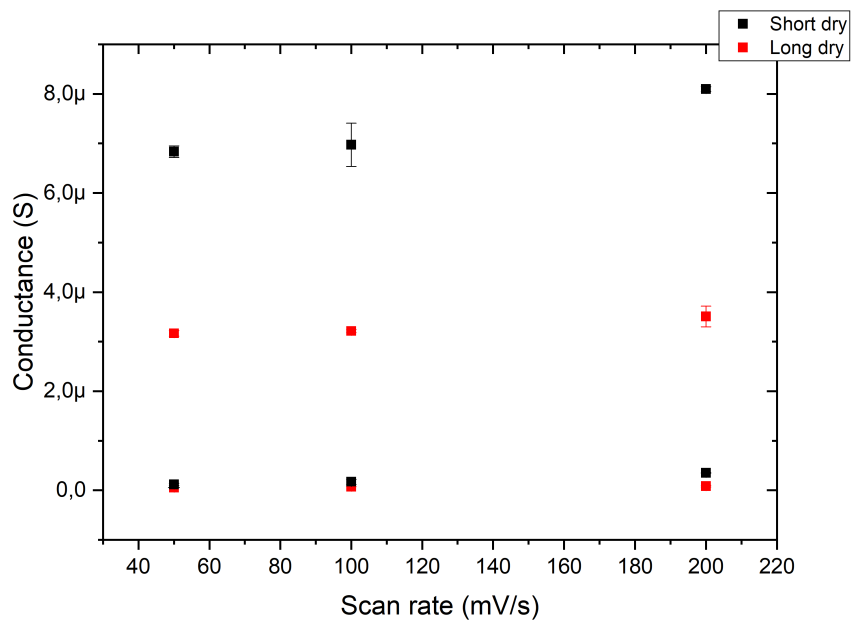


Fig. 4.14 G_{min} and G_{max} at different scan rates, $W \times L = 10 \times 500 \mu m$ long vs short dry case.

4.1.3 Kinetics in voltage and time

Another test includes the excitation of these devices with voltage pulses. This refers to the study of kinetics in voltage and time. Kinetics in voltage consists of exciting the devices with the voltage pulses, whose amplitude is gradually incremented. As reported in Fig. 4.15, the pulses are four and applied for 5 s. The values of the pulses amplitude are 0.4 V, 0.5 V, 0.6 V and 0.7 V, as set/writing voltage values. Before and after each pulse peak, a voltage value of $V_{DS}=0.3$ V is applied for 1 s, as value of pre and post stimulus. Such value is chosen because it is in the middle between the oxidation peak (typically at 0.35-0.4 V) and the reduction one (typically at 0.2-0.25 V). In other words, it does not perturb the measurements, without overwriting the device. After the reading, the voltage goes down to 0.05 V for 5 s, in order to switch off completely the channel (reset, erasing).

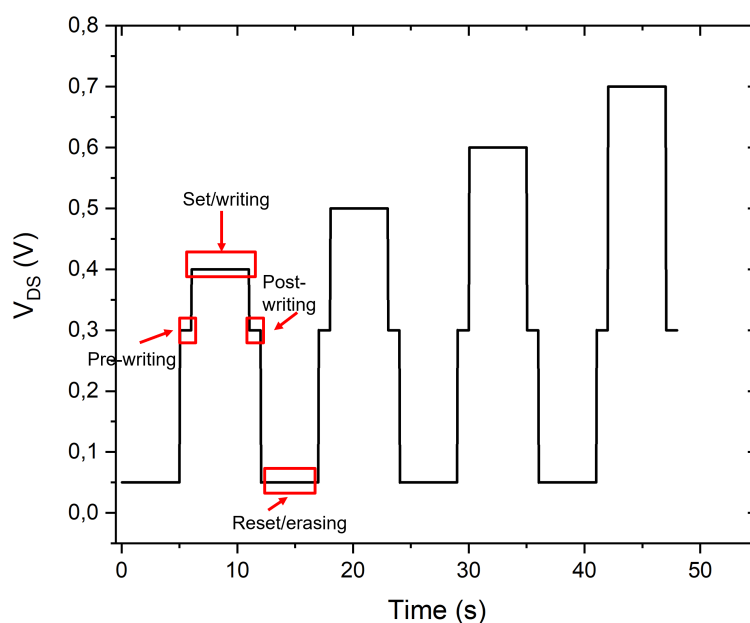


Fig. 4.15 Kinetics in voltage, V_{DS} pulses train signal plot.

An example of a good device response is the one in Fig. 4.16: current peaks are observable, corresponding to the writing pulse values. To reach the maximum current value, there is a transient because of the PANI slow oxidation kinetics: the polymer needs a certain amount of time, dependent on its resistance, to fully complete the reaction and to store completely the charge. On the opposite, after the writing, the discharge occurs with a transient, followed by a

complete switch off of the channel, before exciting the device again. The maximum height of the peaks increases with the amplitude of the voltage pulses, since a larger voltage amplitude implies a greater PANI oxidation. Moreover, the pre and post writing current values show a difference among each other that becomes more and more significant at larger V_{DS} : it is the result of the PANI oxidation, which becomes more and more effective at greater V_{DS} values. In other words, the conductance (or resistance) of the polymer is not a constant value, but it is function of the applied voltage pulse in this case, as expected by one of the internal state variable of the memristance function.

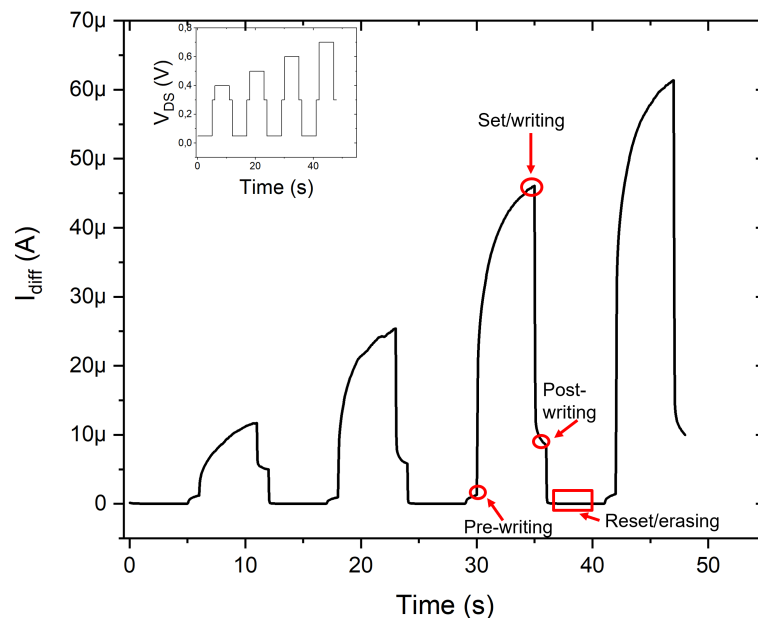


Fig. 4.16 Kinetics in voltage, example of I_{diff} plot. On the top-left side, a inset graph of the input V_{DS} pulses. Short dried device, $W \times L = 250 \times 10$.

For kinetics in time, the V_{DS} pulses have a fixed amplitude, but their temporal width is gradually increased (Fig. 4.17a). Two voltage values were chosen, one at $V_{DS} = 0.4$ V and another one at $V_{DS} = 0.7$ V, in order to see how the response changes at low and high voltage drops. The pulses are 7 in this case and each pulse peak has a different width: 0.05 s, 0.1 s, 0.15 s, 0.2 s, 0.25 s, 0.5 s and 1 s, respectively. The pre and post writing voltage ($V_{DS} = 0.3$ V) are applied for 1 s, while the reset one ($V_{DS} = 0.05$ V) is applied for 5 s.

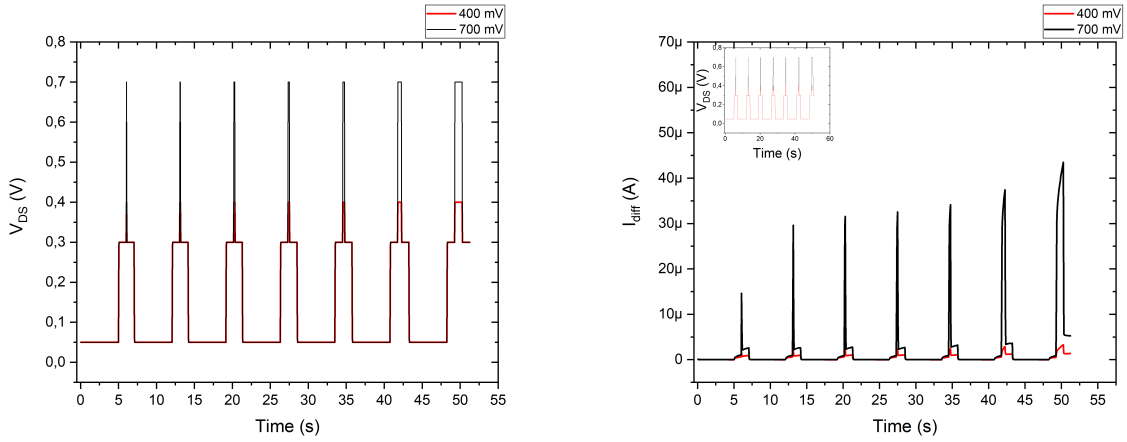
(a) V_{DS} pulses train signal curves.(b) I_{diff} plot, shortly dried $W \times L = 250 \times 10 \mu m$ device.

Fig. 4.17 Kinetics in time.

An example of device response is illustrated in Fig. 4.17b: for both V_{DS} amplitudes, the I_{diff} peak height increases as the V_{DS} pulse width increases. On the one hand, to reach the maximum current value, there is a transient during the writing phase, because of the PANI kinetics already mentioned before. On the other hand, after the writing, the discharge occurs with a transient, followed by a complete switch off of the channel, before exciting the device again. Furthermore, the pre and post-writing current values show a difference among each other that becomes more and more relevant at longer and higher V_{DS} pulses: it is the result of the PANI oxidation, which becomes more and more effective when V_{DS} pulses are promoted by a higher voltage bias and applied for a longer time⁷. In other words, the conductance (or resistance) of the polymer is not a constant value, but it is function of the duration of the applied voltage pulse in this case. This latter, together with the voltage amplitude, is a internal state variable of the memristance function.

⁷From the pre and post-writing current values, G_{pre} and G_{post} values can be extracted respectively, in order to evaluate the synaptic weight variation as function of the V_{DS} pulse amplitude and time width (the related discussion is reported in subsection 4.1.6).

4.1.4 Endurance

The endurance is a significant figure of merit for memory and neuromorphic applications. It indicates the maximum number of writing cycles that a device, within a neural network for instance, is able to perform until reaching the breakdown condition. The higher the endurance, the higher the device reliability and usability. The endurance test was set in such a way that one pulse was defined as follows:

- reset voltage (i.e. $V_{DS} = 0.05$ V) for 1 s;
- pre and post writing voltage (i.e. $V_{DS} = 0.3$ V) for 0.5 s;
- writing voltage (i.e. $V_{DS} = 0.7$ V) for 1 s;

The current values to be considered are the pre and post writing (or reading) ones: the pre-writing corresponds to the OFF current I_{OFF} , while the post-writing one to the ON current I_{ON} . The endurance was tested on those devices with the best performances, for both short and long dry cases. Concerning the first one, in Fig. 4.18a an example is reported: the device channel is working for 2000 cycles at least. The two conduction states are quite separated.

It is worth adding that the peaks observable in both I_{ON} and I_{OFF} contributions are due to the periodic electrolyte re-filling in the PDMS chambers. This was necessary because the liquid electrolyte tends to evaporate at atmospheric environment conditions.

In the second case, the best devices showed a stable response for 2000 cycles at least, with a $\frac{I_{ON}}{I_{OFF}}$ ratio increasing with the channel aspect ratio (Fig. 4.18b-c). The values of ON and OFF currents and the $\frac{I_{ON}}{I_{OFF}}$ ratios are compared among the so tested devices in Table 4.1. The larger the $\frac{I_{ON}}{I_{OFF}}$ ratio, the greater the separation between the two resistance states and the lower the so-called *misclassification* problem. In general, the latter refers to the scarce capability of classifying two elements, in this case the two resistance state values. Moreover, the normal distribution curves are expected to get closer to each other and, in the worst case, to cross to each other. These results are promising, since these devices would be able to work at larger writing cycles conditions, without being deteriorated.

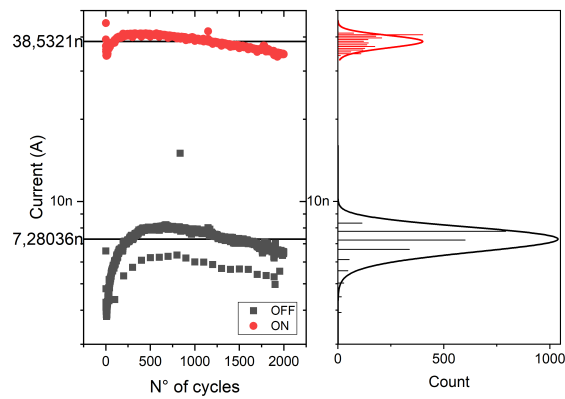
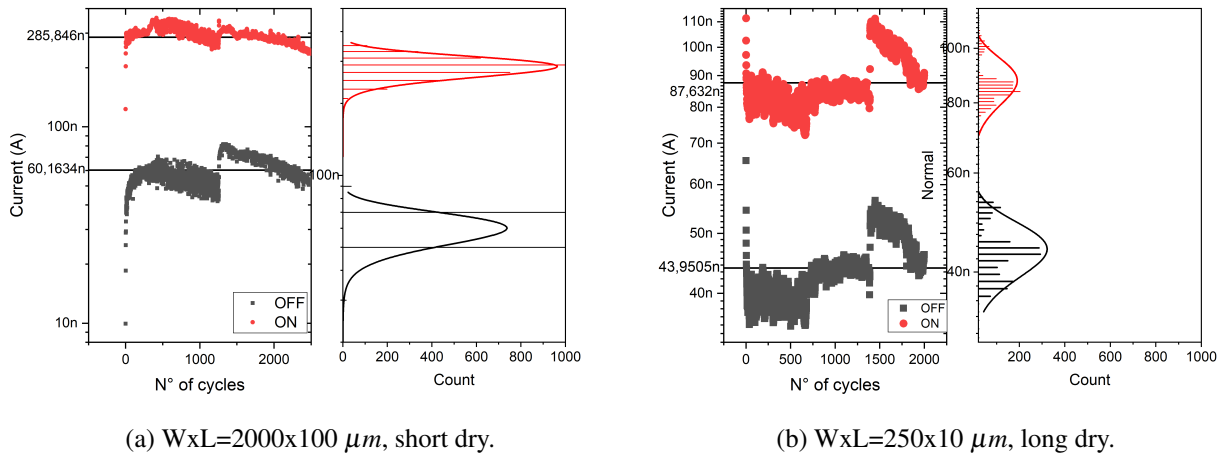


Fig. 4.18 Endurance test results: on the left-hand side, I_{ON} and I_{OFF} current contribution vs the number of writing cycles in semi logarithmic scale. On the right-hand side, I_{ON} and I_{OFF} normal distributions are reported.

Channel sizes $W \times L$ (μm)	I_{ON} (nA)	I_{OFF} (nA)	$\frac{I_{ON}}{I_{OFF}}$
2000x100 (short dry)	285.846	60.134	4.753
250x10 (long dry)	87.632	43.951	1.994
2000x10 (long dry)	38.532	7.28	5.293

Table 4.1 $\frac{I_{ON}}{I_{OFF}}$ ratio comparison.

4.1.5 Neuromorphic properties: definitions

Mimicking biological synapses implies the investigation of their neuromorphic properties. In human brain, synapses can be considered as a cleft: they allow the communication of a neuron with another specific one. This happens only according to several neuro-biological algorithms among which the most famous is the Hebbian rule ("NEURONS THAT FIRE TOGETHER WIRE TOGETHER"). However, a relevant importance must be also attributed to the integrative role of neurons since they govern the integral of the signal sent to the cleft by the synapses and if it overcomes a certain threshold value [10], the signal can be transmitted to the receiver neuron. In this activity, the attention was focused on:

- *Synaptic weight variation*, which corresponds to the electrical resistance (or conductance) variation of the synapse, occurring when neurons are communicating to each other by sending electrical pulse signals (i.e. spikes);
- *Long-Term Potentiation (LTP)*, which is a synaptic strength enhancement, as a result of a long and continuous electrical stimulus in the hippocampus and neocortex;
- *Long-Term Depression (LTD)*, which is a synaptic strength reduction, as the opposite mechanism of LTP [105].

In the next subsections, the results related to the investigation of these properties are reported and discussed.

4.1.6 Neuromorphic properties: the synaptic weight variation

In this study, the equivalent synaptic weight variation was evaluated from the kinetics in voltage and time respectively. Once the pre and post conductance G_{pre} and G_{post} values have been extracted from the pre and post-writing currents, the synaptic weight variation $\frac{\Delta G}{G}$ can be computed as follows:

$$\frac{\Delta G}{G} = \frac{G_{post} - G_{pre}}{G_{pre}} \quad (4.1)$$

Typically, this is the starting point for characterizing neuromorphic properties in these devices. Interpreting in this light the results of the kinetics in voltage (Fig. 4.19), a larger V_{DS} pulse amplitude corresponds to a larger synaptic weight variation, since the difference between the post and pre-writing current values becomes more and more significant, as already discussed previously. From the fast dried devices, one can observe the variability among the ones with same channel dimensions. These results confirm how the PANI thickness variability plays a key role in the equivalent synaptic response of organic memristors.

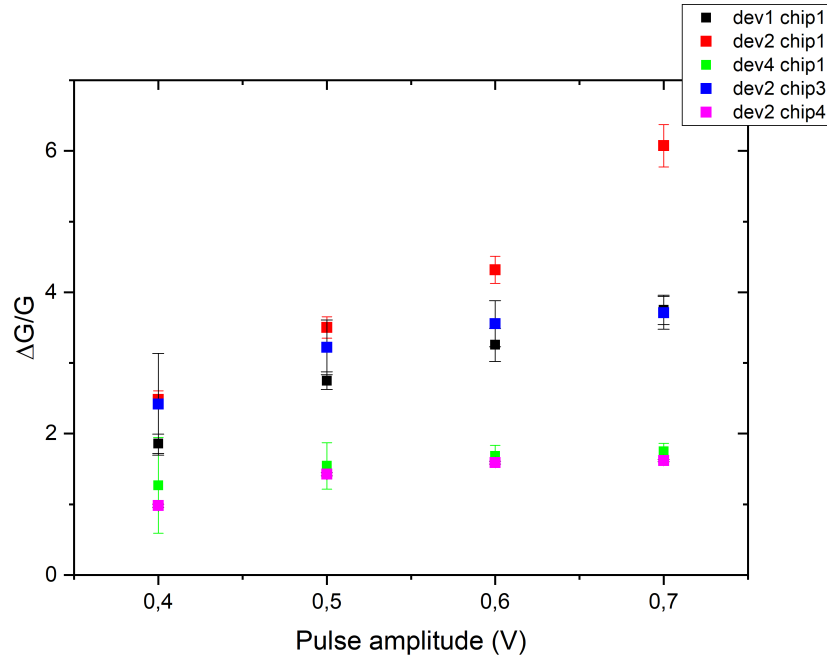
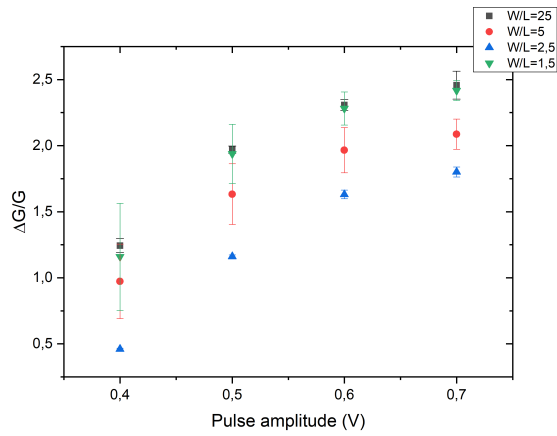
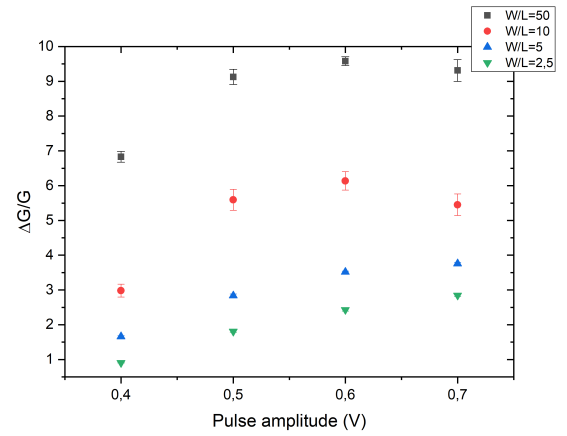
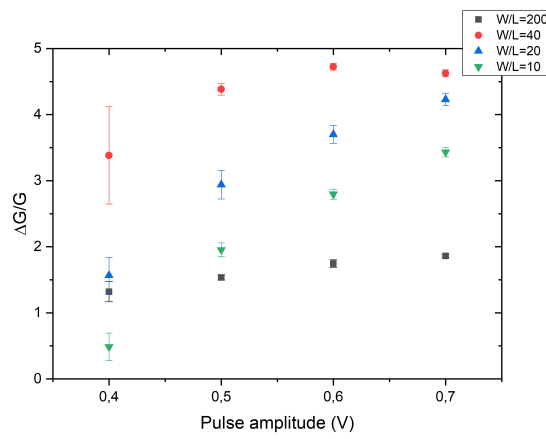
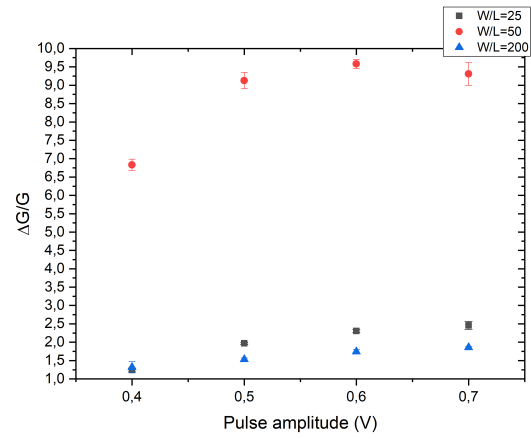


Fig. 4.19 Kinetics in voltage, $\frac{\Delta G}{G}$ vs V_{DS} pulse amplitude plot. Comparison among devices with same aspect ratio (in this case $W \times L = 500 \times 10 \mu m$).

In the respect of long dried devices, Fig. 4.20 show the variation of the equivalent synaptic response according to the different channel sizes. The conductance values, in $w250$ and $w500$ devices, show a increase with the $\frac{W}{L}$ aspect ratio of the channel. However, looking at the $w2000$ devices, the one with channel dimensions $W \times L = 2000 \times 10 \mu m$ is not so performing, compared to the other devices with equal channel length L (Fig. 4.20d). As already observed in the analysis of the hysteresis curves, this might be the consequence of the polymer aging, or the polymeric ink distribution during the dry phase. For what concerns the results coming from the kinetics in time study about the short dried devices (Fig. 4.21a-b) and the long dried ones (Fig. 4.22a-b-c-d), a wider V_{DS} pulse increases the synaptic weight variation. Considerations done for the kinetics in voltage results of $W \times L = 2000 \times 10 \mu m$ channel sized device can be similarly added to the kinetics in time ones of the same device (Fig. 4.22d). These results confirm once more that the two drying procedures return memristive devices with similar synaptic performances. The evolution of the synaptic weights with the pulse amplitude and with the pulse duration follow a very similar trend, regardless the aspect ratio or the drying procedure.

(a) *w250*.(b) *w500*.(c) *w2000*.

(d) The highest channel aspect ratios

Fig. 4.20 Kinetics in voltage, $\frac{\Delta G}{G}$ vs V_{DS} pulse amplitude plot. Comparison among long dried devices.

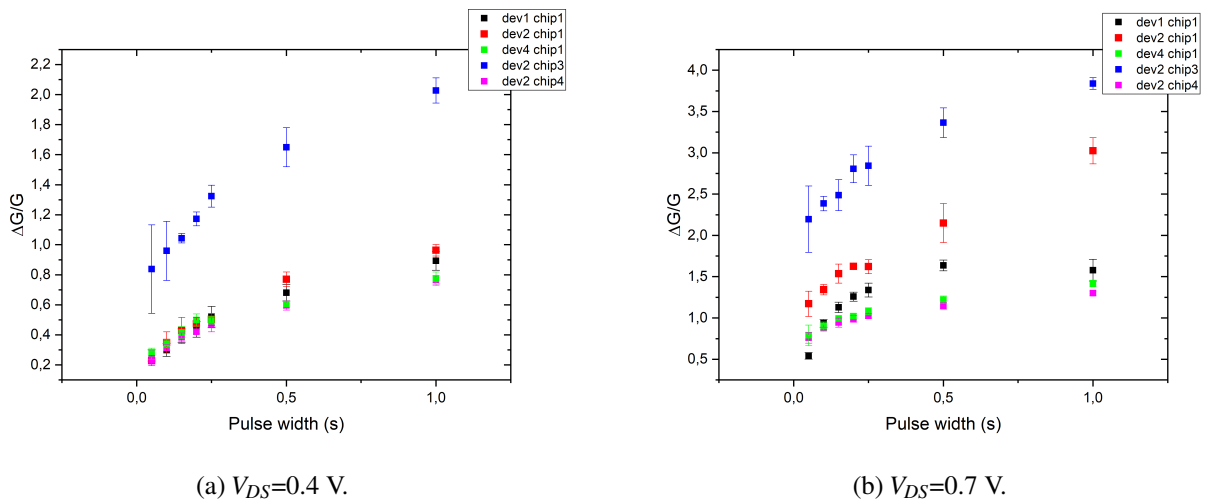


Fig. 4.21 Kinetics in time, $\frac{\Delta G}{G}$ vs V_{DS} pulse width plot. Comparison among shortly dried devices with same aspect ratio (in this case $W \times L=500 \times 10 \mu m$).

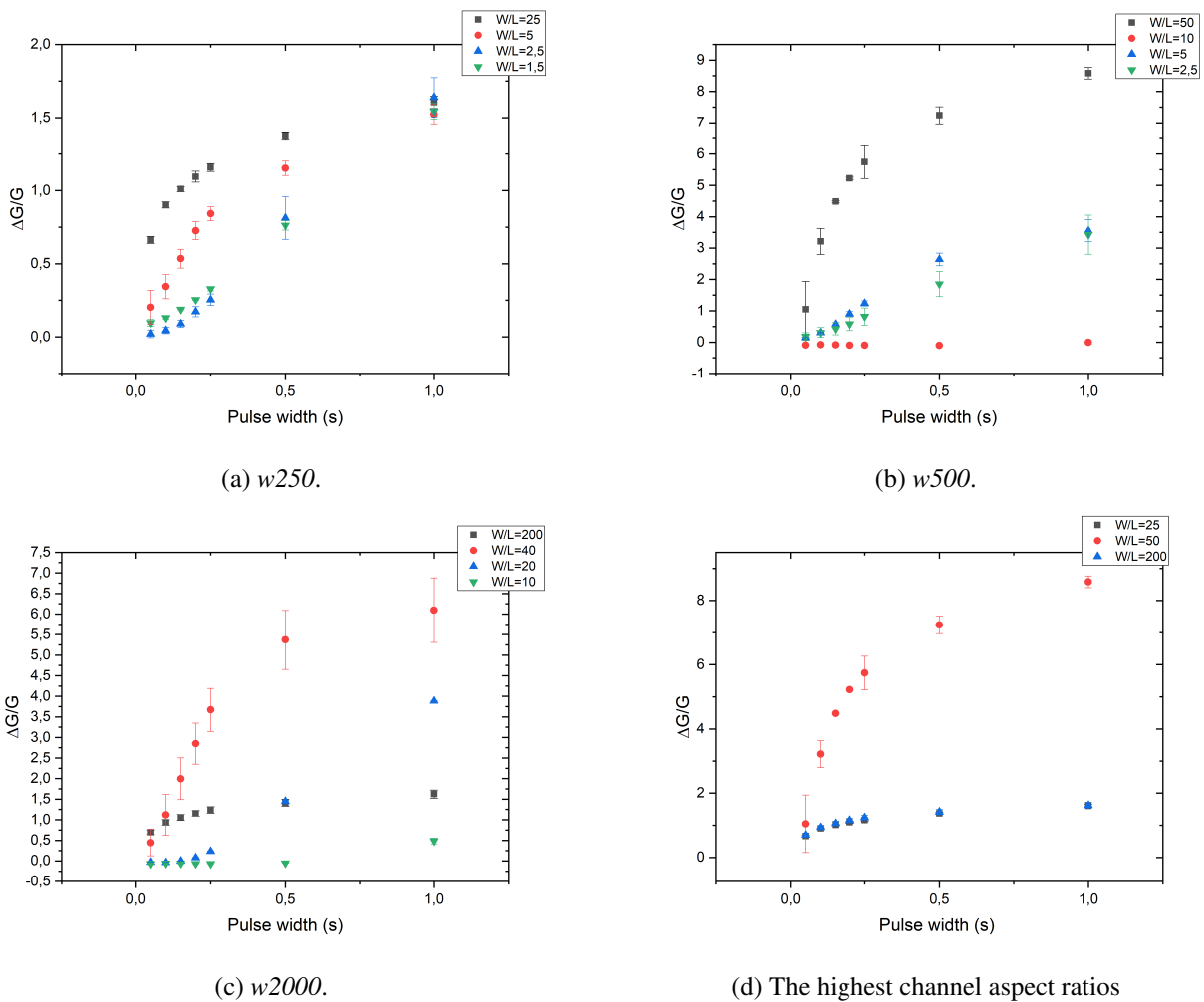


Fig. 4.22 Kinetics in time, $\frac{\Delta G}{G}$ vs V_{DS} pulse amplitude plot. Comparison among long dried devices. $V_{DS}=0.7$ V.

4.1.7 Neuromorphic properties: LTP and LTD

For LTP and LTD, the measurements were carried out by imposing a increasing number of V_{DS} pulses (in sequence: [1;5;10;30;50;100] pulses), whose width is fixed to 100 ms. On the one hand, for LTP the pulses amplitude is fixed to $V_{DS}=0.7$ V (see Fig. 4.23a), since at this voltage drop PANI reaches the maximum conductance value (i.e. potentiation), because of its oxidation. Pre and post-writing voltages are fixed to $V_{DS}=0.3$ V, as in the previously discussed tests, for 1 s. Finally, the reset is imposed through a voltage drop equal to $V_{DS}=0.05$ V for 5 s. On the other hand, for LTD the pulses amplitude is fixed to $V_{DS}=-0.1$ V (see Fig. 4.23b), since at this voltage drop PANI gets completely reduced (i.e. depression). Pre and post-writing voltages are fixed to $V_{DS}=0.3$ V, for 1 s. The reset is imposed through a voltage drop equal to $V_{DS}=0.7$ V for 5 s, as the opposite case of LTP. For the analysis, from the reading current values (before and after the writing pulse) G_{pre} and G_{post} values were extracted, the synaptic weight variation $\frac{\Delta G}{G}$ was computed and the mean value and standard deviation were calculated over the number of performed cycles (5 in this case).

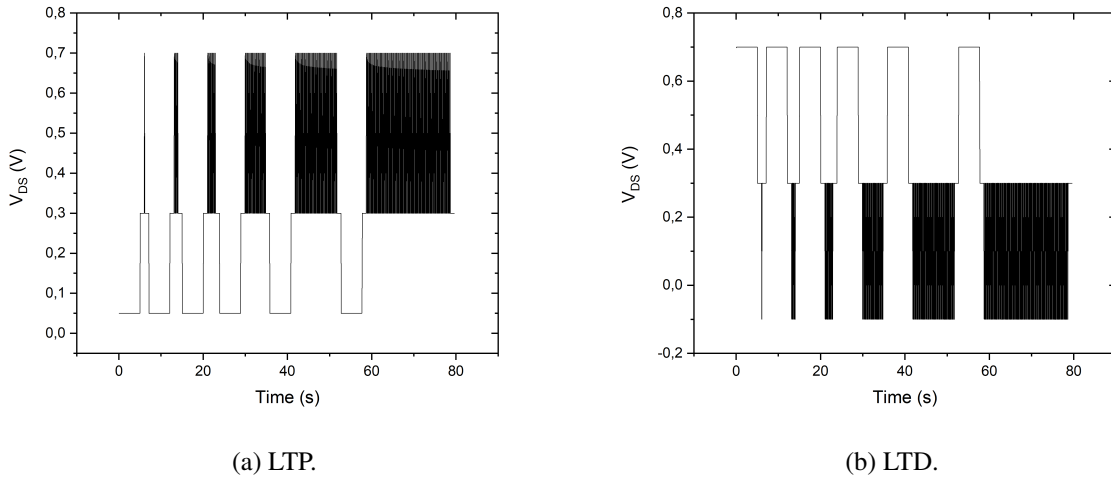


Fig. 4.23 V_{DS} pulses adopted for the measurements.

On the one hand, devices with same geometry and dry procedure, but with different aspect ratio, were chosen for these tests (Fig. 4.24a-b). On the other hand, twin devices, but submitted to a different dry procedure were compared (Fig. 4.25a). Regardless the chosen geometry and the selected drying procedure, all devices show a similar trend. In LTP, the higher the number of pulses the higher is the $\frac{\Delta G}{G}$. In LTD, instead, the higher the number of pulses the lower is the $\frac{\Delta G}{G}$, with more and more negative values, since G_{pre} becomes more and more significant with respect

to G_{post} . Furthermore, in both LTP and LTD cases, the trend reaches the saturation, but it cannot be referred to a sigmoidal one. In fact, also a single pulse of 100 ms implies a synaptic weight variation, the plot does not start at the origin of the plane. Finally, one can state:

- in both LTP and LTD, for both fast and slowly dried devices, the feedback is good, with different values according to the polymer volume and channel sizes;
- for LTP, increasing the number of positive V_{DS} pulses, the synaptic strength increases and the device channel allows a higher and higher electrical conduction (potentiation);
- for LTD, increasing the number of negative V_{DS} pulses, the synaptic strength decreases and the device channel allows a lower and lower electrical conduction (depression);
- as expected, the device geometry factor influences both the LTP and LTD;
- as shown in Fig. 4.25b-c-d-e, a confirm of what in the previous subsections was suggested: $w2000$ devices do not provide more performing results than $w500$ devices, according to the geometry factor. Nevertheless, the causes are subject to study and further improvements as the aim of future work perspectives;
- independently on the dry procedure and the devices under test, the results are promising, with potentialities within an ANN hardware realization.

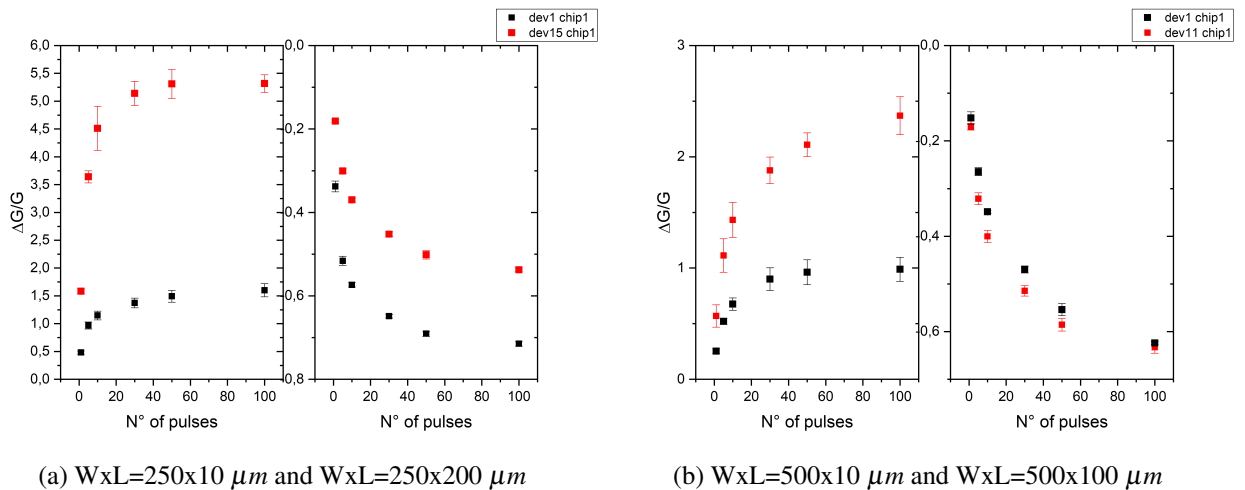


Fig. 4.24 On the left-hand side, LTP plot comparing the performances of short dried devices. On the right-hand side, LTD plot of the same compared devices.

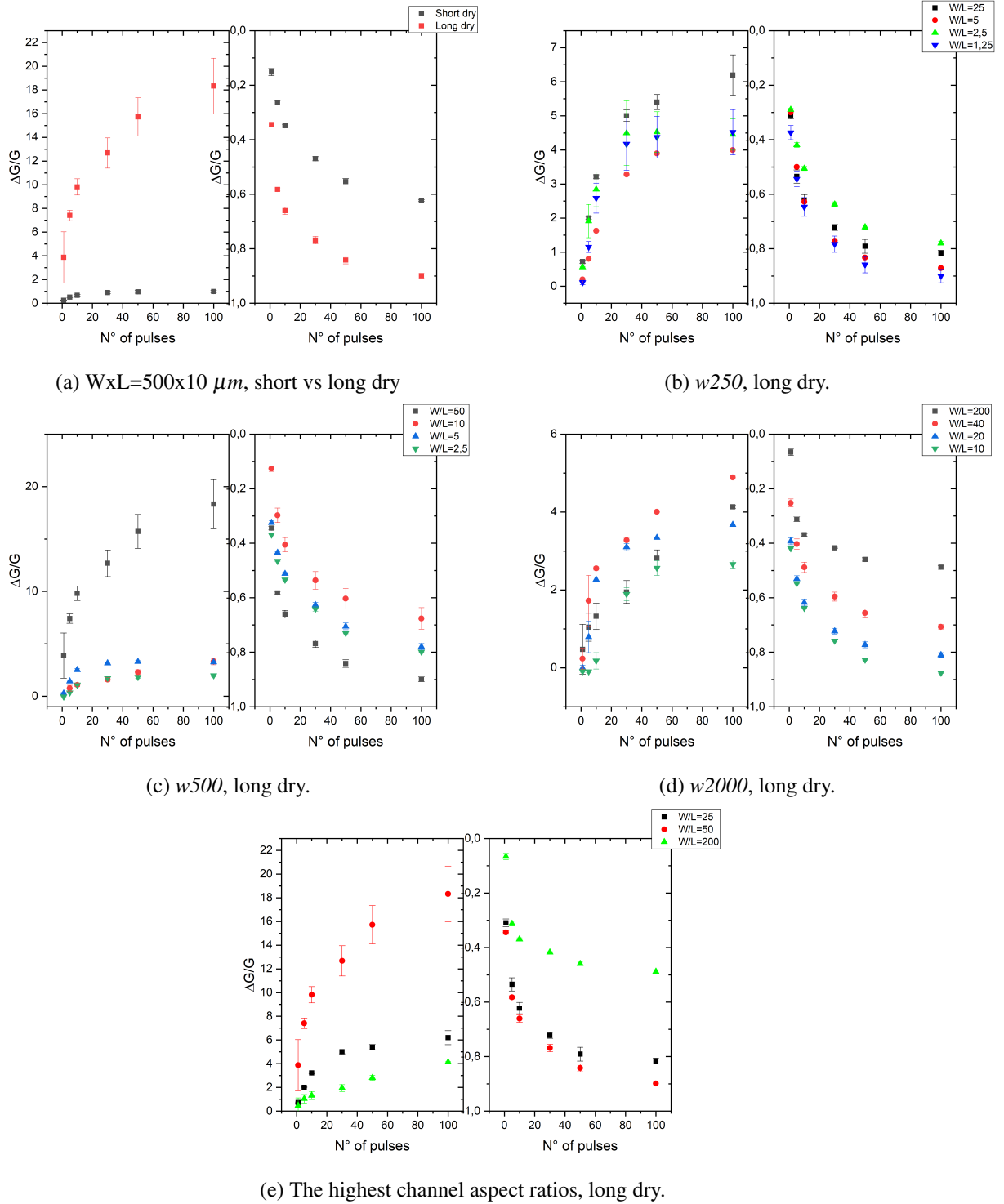


Fig. 4.25 On the left-hand side, LTP plot comparing the performances of different devices. On the right-hand side, LTD plot of the same compared devices.

Chapter 5

Conclusions and future perspectives

In this thesis activity, the realization of organic memristors has been proposed. Their fabrication included standard cleanroom process steps (metal deposition, etching, photolithography and so forth). PANI, the polymer used as active material for these devices, was deposited on the channel by inkjet printing. Therefore, inkjet printing process was optimized. In this respect, the optimization started from the ink synthesis. Three concentrations were tested, in order to find the best one in terms of both printability (avoiding the nozzle clogging problem for instance) and conduction properties of the printed PANI layer. Thus, the best ink concentration to be printed was the one at $500 \mu\text{g/ml}$. Further tests were focused on how the number of printed layers influences the channel conduction. Five printed layers were found to be feasible for appreciable electrical performances, in combination with the ink solution concentration.

To increase the process throughput, the devices layout was optimized, for all the three channel geometries of interest. As a result, the total number of devices per single chip was increased from 8 to 16. The next step was the investigation and optimization of inkjet printer parameters, which were the ones defining the voltage signal waveform (for the ink drop ejection) and the spot ones (for the correct printed pattern). Their proper combination lead to good printed patterns, characterized by a uniform layers on the channel area.

The drying procedure was analyzed, by comparing two main solutions. The first one was a fast and short drying process, consisting of exposing the samples to heat, provided by a heater plate at 80°C . The second one was a slow and long dry process, where the samples were left

to ambient temperature (25°C typically). The morphological analysis was conducted on the samples submitted to these two procedures. Comparing them, the fast drying process affected negatively the quality of the printed patterns, with a non homogeneous PANI volume and the formation of polymer lumps. In the long dried case, the pattern was uniform, without polymer lumps creation. These results found a confirm in the electrical characterization tests.

In fact, a significant variability was observed in the electrical response of devices with the same channel aspect ratio, while for long-dried memristors the variability was much less relevant. From the *i-v* hysteresis curves the maximum and minimum conductance values were extracted as function of the scan rate. The best devices showed a stable behaviour in that case, with a constant gap between low and high conductance states. Moreover, the maximum conductance was studied as function of the channel aspect ratio: as expected, the most conductive devices were the ones with the highest channel aspect ratio, since the conductance is directly proportional to it. After that, the kinetics in voltage and time were investigated, showing the non-linear behaviour of these devices: the resistance is not a constant quantity, but it varies according to two internal state variables. They are the applied voltage amplitude and its time width. The higher and longer the writing voltage pulse, the larger will be the equivalent synaptic weight variation, which can be evaluated as the difference between the post and pre-writing conductance values (or high and low conductance state values).

Endurance tests were carried out to evaluate the long-term stability of organic memristors, really important within a neuromorphic system: for the best devices, a stable electrical response was observed up to 2000 writing cycles at least, for both short and long dry cases.

Neuromorphic properties, such as Long-Term Potentiation (LTP) and Long-Term Depression (LTD), were studied in organic memristive devices with different channel sizes and for both dry procedures. It was observed how, in LTP, the increase of the number of positive voltage pulses lead to an increase in the electrical conduction. In LTD, the increase of negative voltage pulses lead to a decrease in the electrical conduction.

In the whole electrical characterization activity part, the most performing devices were the *w500* ones, even though the expectations were on the *w2000* ones, according to the direct proportionality of the conductance with the channel aspect ratio. In this respect, further consideration are still under study.

As suggested in chapter 2, before the so discussed thesis activity, PANI was deposited through the Langmuir-Schaefer technique for instance. Comparing this latter with inkjet printing, the performances, from the conduction and functional point of view, are quite similar. Nevertheless, the great advantage of inkjet printing is a dramatical reduction of process time, with higher process throughput and its user-independence.

In the next future, further improvement of the ink synthesis procedure can be done, for example by investigating new solvents, followed by an additional amelioration of the inkjet printing process. Nevertheless, it might be interesting to test inkjet-printed devices into neural networks, focusing on their behaviour in neuromorphic systems architectures.

References

- [1] Georgios Ch. Sirakoulis Leon O. Chua and Andrew Adamatzky. *Handbook Of Memristor Networks*. Springer, 2019. doi: 10.1007/978-3-319-76375-0.
- [2] Alexandre Yasuo Yamamoto. *Memristor engineering: modeling, fabrication and characterization*. PhD thesis, Texas AM University, 2019.
- [3] J. Joshua Yang, Isao H. Inoue, Thomas Mikolajick, and Cheol Seong Hwang. Metal oxide memories based on thermochemical and valence change mechanisms. *MRS Bulletin*, 37: 131–137, 2 2012. doi: 10.1557/MRS.2011.356.
- [4] Damien Querlioz Bipin Rajendran Sabina Spiga, Abu Sebastian. *Memristive Devices for Brain-Inspired Computing: From Materials, Devices, and Circuits to Applications - Computational Memory, Deep Learning, and Spiking Neural Networks*. Electronic and Optical Materials. Woodhead Publishing, 1st edition, 2020. doi: 10.1016/C2017-0-04786-9.
- [5] Mahyar Shahsavari and Pierre Boulet. Memristor nanodevice for unconventional computing: review and applications. 3 2017. doi: 10.48550/arxiv.1703.00331.
- [6] Lei Yuan, Shuzhi Liu, Weilin Chen, Fei Fan, and Gang Liu. Organic memory and memristors: from mechanisms, materials to devices. *Advanced Electronic Materials*, 7 (11):2100432, 2021. doi: 10.1002/aelm.202100432.
- [7] Hyongsuk Kim, Maheshwar Pd Sah, Changju Yang, Tams Roska, and Leon O. Chua. Memristor bridge synapses. *Proceedings of the IEEE*, 100:2061–2070, 2012. doi: 10.1109/JPROC.2011.2166749.
- [8] Anteo Smerieri. *An organic memristor as the building block for bio-inspired adaptive networks*. PhD thesis, Parma University, 2011.
- [9] Bansi Malhotra, Chetna Dhand, Rajamani Lakshminarayanan, Neeraj Dwivedi, Sachin Mishra, Pratima Solanki, Venkatesh Mayandi, Roger Beuerman, and Seeram Ramakrishna. Polyaniline-based biosensors. *Nanobiosensors in Disease Diagnosis*, 4:25, 07 2015. doi: 10.2147/NDD.S64841.
- [10] Victor Erokhin. *Fundamentals of Organic Neuromorphic Systems*. Springer, 1st edition, 2022. doi: 10.1007/978-3-030-79492-7.

- [11] Justin Lemarchand, Nathalie Bridonneau, Nicolas Battaglini, Florent Carn, Giorgio Mattana, Benoit Piro, Samia Zrig, and Vincent Noël. Challenges and prospects of inkjet printed electronics emerging applications : A chemist point of view. *Angewandte International Edition A Journal of the Gesellschaft Deutscher Chemiker Chemie*, 2022. doi: 10.1002/anie.202200166.
- [12] Samiei Nasim. Recent trends on applications of 3d printing technology on the design and manufacture of pharmaceutical oral formulation: a mini review. *Beni-Suef University Journal of Basic and Applied Sciences*, 9, 05 2020. doi: 10.1186/s43088-020-00040-4.
- [13] Alan Faulkner-Jones and Wenmiao (Will) Shu. Biological cell printing technologies. *Nanotechnology Perceptions*, 8:35–57, 03 2012. doi: 10.4024/N02FA12A.ntp.08.01.
- [14] Soleimani gorgani Atasheh. *Printing on polymers: fundamentals and applications*. 2016. doi: 10.1016/C2014-0-02411-2.
- [15] Terence G. Henares, Kentaro Yamada, Koji Suzuki, and Daniel Citterio. *Inkjet Printing of Biomolecules for Biorecognition*, pages 197–235. Springer International Publishing, Cham, 2015. doi: 10.1007/978-3-319-17061-9_8.
- [16] Elahe Jabari, Farzad Liravi, and Ehsan Toyserkani. 2d printing of graphene: a review. *2D Materials*, 08 2019. doi: 10.1088/2053-1583/ab29b2/meta.
- [17] Leila Salucci. Process optimization and experimental measurements of organic electrochemical transistors for in liquid biosensing. Master’s thesis, Politecnico di Torino, 2018.
- [18] MicroFab Technologies. Technotes 99-03, . URL <http://microfab.com/images/pdfs/technote99-03.pdf>.
- [19] Leon O. Chua. Memristor—the missing circuit element. *IEEE Transactions on Circuit Theory*, 18:507–519, 1971. doi: 10.1109/TCT.1971.1083337.
- [20] María García Fernández. Memristor-based neuromorphic computing—design and simulation of a neural network based on memristor technology. Master’s thesis, Delft University of Technology, 2020.
- [21] Leon Chua. If it’s pinched it’s a memristor. *Semiconductor Science and Technology*, 29, 10 2014. doi: 10.1088/0268-1242/29/10/104001.
- [22] Jacopo Secco. *Memristor Platforms for Pattern Recognition Memristor Theory, Systems and Applications*. PhD thesis, Politecnico di Torino, 2017.
- [23] Richard Stanley Williams. How we found the missing memristor. In *Chaos, CNN, memristors and beyond*, pages 483–489. World Scientific, 2013. doi: 10.1142/9789814434805_0038.
- [24] Robert Duncan Stewart Richard Stanley Williams B. Dmitri Strukov, S. Gregory Snider. The missing memristor found. *Nature*, 453, 5 2008. doi: 10.1038/nature06932.

- [25] Baker Mohammad, Maguy Abi Jaoude, Vikas Kumar, Dirar Mohammad Al Homouz, Heba Abu Nahla, Mahmoud Al-Qutayri, and Nicolas Christoforou. State of the art of metal oxide memristor devices. *Nanotechnology Reviews*, 5(3):311–329, 2016. doi: 10.1515/ntrev-2015-0029.
- [26] Zhongrui Wang, Huaqiang Wu, Geoffrey W. Burr, Cheol Seong Hwang, Kang L. Wang, Qiangfei Xia, and J. Joshua Yang. Resistive switching materials for information processing. *Nature Reviews Materials 2020 5:3*, 5:173–195, 1 2020. doi: 10.1038/S41578-019-0159-3.
- [27] Julie Grollier, Damien Querlioz, KY Camsari, Karin Everschor-Sitte, Shunsuke Fukami, and Mark D Stiles. Neuromorphic spintronics. *Nature electronics*, 3(7):360–370, 2020. doi: 10.1038/s41928-019-0360-9.
- [28] Radu Berdan, Takao Marukame, Kensuke Ota, Marina Yamaguchi, Masumi Saitoh, Shosuke Fujii, Jun Deguchi, and Yoshifumi Nishi. Low-power linear computation using nonlinear ferroelectric tunnel junction memristors. *Nature Electronics*, 3(5):259–266, 2020. doi: 10.1038/s41928-020-0405-0.
- [29] André Chanthbouala, Vincent Garcia, Ryan O Cherifi, Karim Bouzehouane, Stéphane Fusil, Xavier Moya, Stéphane Xavier, Hiroyuki Yamada, Cyrile Deranlot, Neil D Mathur, et al. A ferroelectric memristor. *Nature materials*, 11(10):860–864, 2012. doi: 10.1038/nmat3415.
- [30] Yoeri Van De Burgt, Armantas Melianas, Scott Tom Keene, George Malliaras, and Alberto Salleo. Organic electronics for neuromorphic computing. *Nature Electronics*, 1:386–397, 7 2018. doi: 10.1038/s41928-018-0103-3.
- [31] Gang Liu, Cheng Wang, Wenbin Zhang, Liang Pan, Chaochao Zhang, Xi Yang, Fei Fan, Yu Chen, and Run-Wei Li. Organic biomimicking memristor for information storage and processing applications. *Advanced Electronic Materials*, 2(2), 2016. doi: 10.1002/aelm.201500298.
- [32] Hea-Lim Park and Tae-Woo Lee. Organic and perovskite memristors for neuromorphic computing. *Organic Electronics*, 98:10.1016/j.orgel.2021.106301, 2021.
- [33] Shahar Kvatinsky, Dmitry Belousov, Slavik Liman, Guy Satat, Nimrod Wald, Eby G. Friedman, Avinoam Kolodny, and Uri C. Weiser. Magic—memristor-aided logic. *IEEE Transactions on Circuits and Systems II: Express Briefs*, 61(11):895–899, 2014. doi: 10.1109/TCSII.2014.2357292.
- [34] Kyung Min Kim and Richard Stanley Williams. A family of stateful memristor gates for complete cascading logic. *IEEE Transactions on Circuits and Systems I: Regular Papers*, 66(11):4348–4355, 2019. doi: 10.1109/TCSI.2019.2926811.
- [35] Muhammad Khalid, Sana Mukhtar, Mohammad Jawaid Siddique, and Sumair Faisal Ahmed. Memristor based full adder circuit for better performance. *Transactions on Electrical and Electronic Materials*, 20(5):403–410, 2019. doi: 10.1007/s42341-019-00135-5.

- [36] Divya Mahajan, Matheen Musaddiq, and Earl E. Swartzlander. Memristor based adders. In *2014 48th Asilomar Conference on Signals, Systems and Computers*, pages 1256–1260, 2014. doi: 10.1109/ACSSC.2014.7094661.
- [37] Mohammed F. Tolba, Mohammed E. Fouda, Haneen G. Hezayyin, Ahmed H. Madian, and Ahmed G. Radwan. Memristor fpga ip core implementation for analog and digital applications. *IEEE Transactions on Circuits and Systems II: Express Briefs*, 66(8):1381–1385, 2019. doi: 10.1109/TCSII.2018.2882496.
- [38] Jason Cong and Bingjun Xiao. mrfpga: A novel fpga architecture with memristor-based reconfiguration. In *2011 IEEE/ACM International Symposium on Nanoscale Architectures*, pages 1–8, 2011. doi: 10.1109/NANOARCH.2011.5941476.
- [39] Jeff Sun. Cmos and memristor technologies for neuromorphic computing applications. URL <http://www.eecs.berkeley.edu/Pubs/TechRpts/2015/EECS-2015-219.html>.
- [40] M. Amimul; Zhou Zhen; Shen Fangyang; Yi Yang An, Hongyu; Ehsan. Monolithic 3d neuromorphic computing system with hybrid cmos and memristor-based synapses and neurons. *Integration, the VLSI Journal*, 65, 3 2019. doi: 10.1016/j.vlsi.2017.10.009.
- [41] Jose M Cruz-Albrecht, Timothy Derosier, and Narayan Srinivasa. A scalable neural chip with synaptic electronics using cmos integrated memristors. *Nanotechnology*, 24(38): 384011, 2013. doi: 10.1088/0957-4484/24/38/384011/meta.
- [42] Madankumar Sampath, Pravin S. Mane, and C. K. Ramesha. Hybrid cmos-memristor based fpga architecture. In *2015 International Conference on VLSI Systems, Architecture, Technology and Applications (VLSI-SATA)*, pages 1–6, 2015. doi: 10.1109/VLSI-SATA.2015.7050461.
- [43] Fuxi Cai, Justin M Correll, Seung Hwan Lee, Yong Lim, Vishishtha Bothra, Zhengya Zhang, Michael P Flynn, and Wei D Lu. A fully integrated reprogrammable memristor-cmos system for efficient multiply-accumulate operations. *Nature Electronics*, 2(7): 290–299, 2019. doi: 10.1038/s41928-019-0270-x.
- [44] Amirali Amirsoleimani, Fabien Alibart, Victor Yon, Jianxiong Xu, M Reza Pazhouhandeh, Serge Ecoffey, Yann Beilliard, Roman Genov, and Dominique Drouin. In-memory vector-matrix multiplication in monolithic complementary metal-oxide-semiconductor-memristor integrated circuits: Design choices, challenges, and perspectives. *Advanced Intelligent Systems*, 2(11), 2020. doi: 10.1002/aisy.202000115.
- [45] Can Li, Yunning Li, Hao Jiang, Wenhao Song, Peng Lin, Zhongrui Wang, J. Joshua Yang, Qiangfei Xia, Miao Hu, Eric Montgomery, Jiaming Zhang, Noraica Dávila, Catherine E. Graves, Zhiyong Li, John Paul Strachan, Richard Stanley Williams, Ning Ge, Mark Barnell, and Qing Wu. Large memristor crossbars for analog computing. In *2018 IEEE International Symposium on Circuits and Systems (ISCAS)*, pages 1–4, 2018. doi: 10.1109/ISCAS.2018.8351877.
- [46] Zhong Sun, Giacomo Pedretti, Elia Ambrosi, Alessandro Bricalli, Wei Wang, and Daniele Ielmini. Solving matrix equations in one step with cross-point resistive arrays. *Proceedings*

- of the National Academy of Sciences*, 116(10):4123–4128, 2019. doi: 10.1073/pnas.1815682116.
- [47] Anil Korkmaz, Chaoyi He, Linda P. B. Katehi, R. Stanley Williams, and Samuel Palermo. Design of tunable analog filters using memristive crossbars. In *2021 IEEE International Symposium on Circuits and Systems (ISCAS)*, pages 1–5, 2021. doi: 10.1109/ISCAS51556.2021.9401275.
- [48] Shawkat Ali, Arshad Hassan, Gul Hassan, Jinho Bae, and Chong Hyun Lee. Memristor-capacitor passive filters to tune both cut-off frequency and bandwidth. In *2017 25th Optical Fiber Sensors Conference (OFS)*, pages 1–4, 2017. doi: 10.1117/12.2264963.
- [49] Chithra Liz Palson, Deepti Das Krishna, Jimson Mathew, Babita Roslind Jose, Marco Ottavi, and Vishal Gupta. Memristor based adaptive impedance and frequency tuning network. *Proceedings - 2018 13th IEEE International Conference on Design and Technology of Integrated Systems In Nanoscale Era, DTIS 2018*, pages 1–2, 5 2018. doi: 10.1109/DTIS.2018.8368553.
- [50] Yasmin Halawani, Baker Mohammad, Mahmoud Al-Qutayri, and Said F. Al-Sarawi. Memristor-based hardware accelerator for image compression. *IEEE Transactions on Very Large Scale Integration (VLSI) Systems*, 26:2749–2758, 12 2018. doi: 10.1109/TVLSI.2018.2835572.
- [51] Roberto Marani, Gennaro Gelao, and Anna Gina Perri. A review on memristor applications. *International Journal of Advances in Engineering and Technology (IJAET)*, 2015. doi: 10.48550/arXiv.1506.06899.
- [52] Arpita Sinha, Manjari S. Kulkarni, and Christof Teuscher. Evolving nanoscale associative memories with memristors. In *2011 11th IEEE International Conference on Nanotechnology*, pages 860–864, 2011. doi: 10.1109/NANO.2011.6144623.
- [53] Arturo Sarmiento-Reyes and Marco A. Zamudio Hernández. Image edge detection with a memristive grid: a massive parallel approach. In *2020 IEEE 11th Latin American Symposium on Circuits Systems (LASCAS)*, pages 1–4, 2020. doi: 10.1109/LASCAS45839.2020.9068991.
- [54] Zoha Pajouhi and Kaushik Roy. Image edge detection based on swarm intelligence using memristive networks. *IEEE Transactions on Computer-Aided Design of Integrated Circuits and Systems*, 37(9):1774–1787, 2018. doi: 10.1109/TCAD.2017.2775227.
- [55] Shunsuke Yamamoto, Anastasios G. Polyravas, Sanggil Han, and George G. Malliaras. Correlation between transient response and neuromorphic behavior in organic electrochemical transistors. *Advanced Electronic Materials*, 8, 4 2022. doi: 10.1002/AELM.202101186.
- [56] Chetna Dhand, Maumita Das, Monika Datta, and BD Malhotra. Recent advances in polyaniline based biosensors. *Biosensors and Bioelectronics*, 26(6):2811–2821, 2011. doi: 10.1016/j.bios.2010.10.017.

- [57] Silvia Battistoni, Victor Erokhin, Nicola Cornella, Tatiana Berzina, Paolo Macchi, and Salvatore Iannotta. Analysis of pani biocompatibility with neuronal cells. *2015 International Conference on Memristive Systems, MEMRISYS 2015*, 1 2016. doi: 10.1109/MEMRISYS.2015.7378403.
- [58] Victor Erokhin, Gerard David Howard, and Andrew Adamatzky. Organic memristor devices for logic elements with memory. *International Journal of Bifurcation and Chaos*, 22, 12 2012. doi: 10.1142/S0218127412502835.
- [59] Sambhu Bhadra, Dipak Khastgir, Nikhil K. Singha, and Joong Hee Lee. Progress in preparation, processing and applications of polyaniline. *Progress in Polymer Science (Oxford)*, 34:783–810, 8 2009. doi: 10.1016/j.progpolymsci.2009.04.003.
- [60] Nirmala Kumari Jangid, Sapana Jadoun, and Navjeet Kaur. A review on high-throughput synthesis, deposition of thin films and properties of polyaniline. *European Polymer Journal*, 125, 2 2020. doi: 10.1016/J.EURPOLYMJ.2020.109485.
- [61] Shlomo Magdassi. *The Chemistry of Inkjet Inks*. 2009. doi: 10.1142/6869.
- [62] Stephen D Hoath. *Fundamentals of Inkjet Printing*. 2016. doi: 10.1002/9783527684724.
- [63] Alessio Bucciarelli, Chandrakanth Reddy Chandraiahgari, Andrea Adami, Viviana Muloni, and Leandro Lorenzelli. Precise dot inkjet printing thought multifactorial statistical optimization of the piezoelectric actuator waveform. *Flexible and Printed Electronics*, 5, 10 2020. doi: 10.1088/2058-8585/ABBB7E.
- [64] Zhaoyao Zhan, Jianing An, Yuefan Wei, Van Thai Tran, and Hejun Du. Inkjet-printed optoelectronics. *Nanoscale*, 9:965–993, 1 2017. doi: 10.1039/C6NR08220C.
- [65] Andreas C. Fischer, Matti Mäntysalo, and Frank Niklaus. Inkjet printing, laser-based micromachining, and micro–3d printing technologies for mems. *Handbook of Silicon Based MEMS Materials and Technologies*, pages 531–545, 1 2020. doi: 10.1016/B978-0-12-817786-0.00021-9.
- [66] Niels Quack, J. Sadie, Vivek Subramanian, and Ming C. Wu. Through silicon vias and thermocompression bonding using inkjet-printed gold nanoparticles for heterogeneous mems integration. *2013 Transducers and Eurosensors XXVII: The 17th International Conference on Solid-State Sensors, Actuators and Microsystems, TRANSDUCERS and EUROSENSORS 2013*, pages 834–837, 2013. doi: 10.1109/TRANSDUCERS.2013.6626896.
- [67] Yanfei Xu, Ingolf Hennig, Dieter Freyberg, Andrew James Strudwick, Matthias Georg Schwab, Thomas Weitz, and Kitty Chih-Pei Cha. Inkjet-printed energy storage device using graphene/polyaniline inks. *Journal of Power Sources*, 248:483–488, 2014. doi: 10.1016/j.jpowsour.2013.09.096.
- [68] Bongjun Kim, Michael L. Geier, Mark C. Hersam, and Ananth Dodabalapur. Inkjet printed circuits on flexible and rigid substrates based on ambipolar carbon nanotubes with high operational stability. *ACS Applied Materials and Interfaces*, 7:27654–27660, 12 2015. doi: 10.1021/ACSAMI.5B07727/SUPPL_FILE/AM5B07727_SI_001.PDF.

- [69] Hyojin Ko, Jumi Lee, Yongjun Kim, Byeongno Lee, Chan-Hee Jung, Jae-Hak Choi, Oh-Sun Kwon, and Kwanwoo Shin. Active digital microfluidic paper chips with inkjet-printed patterned electrodes. *Advanced Materials*, 26:2335–2340, 4 2014. doi: 10.1002/ADMA.201305014.
- [70] Jumana Abu-Khalaf, Razan Saraireh, Saleh Eisa, Ala’aldeen Al-Halhouli, et al. Experimental characterization of inkjet-printed stretchable circuits for wearable sensor applications. *Sensors*, 18(10), 2018.
- [71] Alaaldeen Al-Halhouli, Hala Qitouqa, Abdallah Alashqar, and Jumana Abu-Khalaf. Inkjet printing for the fabrication of flexible/stretchable wearable electronic devices and sensors. *Sensor Review*, 38(4):438–452, 2018. doi: 10.1108/SR-07-2017-0126.
- [72] Li-Wei Lo, Hongyang Shi, Haochuan Wan, Zhihao Xu, Xiaobo Tan, and Chuan Wang. Inkjet-printed soft resistive pressure sensor patch for wearable electronics applications. *Advanced Materials Technologies*, 5(1), 2020. doi: 10.1002/admt.201900717.
- [73] Ana Moya, Gemma Gabriel, Rosa Villa, and F. Javier del Campo. Inkjet-printed electrochemical sensors. *Current Opinion in Electrochemistry*, 3(1):29–39, 2017. doi: 10.1016/j.coelec.2017.05.003.
- [74] Francisco Molina-Lopez, Danick Briand, Nico F de Rooij, and Maria Smolander. Fully inkjet-printed parallel-plate capacitive gas sensors on flexible substrate. In *SENSORS, 2012 IEEE*, pages 1–4. IEEE, 2012. doi: 10.1109/ICSENS.2012.6411148.
- [75] Karl Crowley, Aoife Morrin, Roderick L. Shepherd, Marc In Het Panhuis, Gordon G. Wallace, Malcolm R. Smyth, and Anthony J. Killard. Fabrication of polyaniline-based gas sensors using piezoelectric inkjet and screen printing for the detection of hydrogen sulfide. *IEEE Sensors Journal*, 10:1419–1426, 2010. doi: 10.1109/JSEN.2010.2044996.
- [76] Karl Crowley, Aoife Morrin, Malcolm R. Smyth, Anthony J. Killard, Roderick Shepherd, Marc In Het Panhuis, and Gordon G. Wallace. Fabrication of chemical sensors using inkjet printing and application to gas detection. *Proceedings of IEEE Sensors*, pages 13–16, 2008. doi: 10.1109/ICSENS.2008.4716371.
- [77] Fausta Loffredo, Gianbattista Burrasca, Luigi Quercia, and Dario Della Sala. Gas sensor devices obtained by ink-jet printing of polyaniline suspensions. *Macromolecular Symposia*, 247:357–363, 2 2007. doi: 10.1002/MASY.200750141.
- [78] Alexander Bietsch, Jiayun Zhang, Martin Hegner, Hans Peter Lang, and Christoph Gerber. Rapid functionalization of cantilever array sensors by inkjet printing. *Nanotechnology*, 15(8):873, 2004. doi: 10.1088/0957-4484/15/8/002.
- [79] Vítor Correia, C. Caparros, C. Casellas, L. Francesch, J.G. Rocha, and S. Lanceros-Mendez. Development of inkjet printed strain sensors. *Smart Materials and Structures*, 22(10), 2013. doi: 10.1088/0964-1726/22/10/105028.
- [80] Saleem Khan, Shawkat Ali, Arshad Khan, Moaaz Ahmed, Bo Wang, and A Bermak. Inkjet printing of multi-stripes based deflection monitoring sensor on flexible substrate. *Sensors and Actuators A: Physical*, 323, 2021. doi: 10.1016/j.sna.2021.112638.

- [81] Pengyu Zhou, Yaozhong Liao, Yehai Li, Dongyue Pan, Wuxiong Cao, Xiongbin Yang, Fangxin Zou, Li-min Zhou, Zhong Zhang, and Zhongqing Su. An inkjet-printed, flexible, ultra-broadband nanocomposite film sensor for in-situ acquisition of high-frequency dynamic strains. *Composites Part A: Applied Science and Manufacturing*, 125, 2019. doi: 10.1016/j.compositesa.2019.105554.
- [82] Keun Young Shin, Jin Yong Hong, and Jyongsik Jang. Micropatterning of graphene sheets by inkjet printing and its wideband dipole-antenna application. *Advanced Materials*, 23: 2113–2118, 5 2011. doi: 10.1002/ADMA.201100345.
- [83] Sangkil Kim, Benjamin Cook, Taoran Le, James Cooper, Hoseon Lee, Vasileios Lakafosis, Rushi Vyas, Riccardo Moro, Maurizio Bozzi, Apostolos Georgiadis, et al. Inkjet-printed antennas, sensors and circuits on paper substrate. *IET microwaves, antennas & propagation*, 7(10):858–868, 2013. doi: 10.1049/iet-map.2012.0685.
- [84] Madhusudan Singh, Hanna M. Haverinen, Parul Dhagat, and Ghassan E. Jabbour. Inkjet printing-process and its applications. *Advanced Materials*, 22:673–685, 2 2010. doi: 10.1002/ADMA.200901141.
- [85] Sebastian Nau, Christoph Wolf, Karl Popovic, Alexander Blümel, Francesco Santoni, Alessio Gagliardi, Aldo di Carlo, Stefan Sax, and Emil JW List-Kratochvil. Inkjet-printed resistive switching memory based on organic dielectric materials: From single elements to array technology. *Advanced Electronic Materials*, 1(1-2), 2015. doi: 10.1002/aelm.201400003.
- [86] Bernard Huber, Jacob Schober, A. Kreuzer, Michael Kaiser, Andréas Ruediger, and Christina Schindler. Inkjet-printed resistive memory cells for transparent electronics. *Microelectronic Engineering*, 194:85–88, 2018. doi: 10.1016/j.mee.2018.03.006.
- [87] Giovanni Vescio, Gemma Martín, Albert Crespo-Yepes, Sergi Claramunt, Daniel Alonso, Julian Lopez-Vidrier, Sonia Estrade, Marc Porti, Rosana Rodriguez, Francesca Peiro, et al. Low-power, high-performance, non-volatile inkjet-printed hfo₂-based resistive random access memory: from device to nanoscale characterization. *ACS applied materials & interfaces*, 11(26):23659–23666, 2019. doi: 10.1021/acsami.9b01731.
- [88] Sungjune Jung, Antony Sou, Enrico Gili, and Henning Sirringhaus. Inkjet-printed resistors with a wide resistance range for printed read-only memory applications. *Organic electronics*, 14:699–702, 2013. doi: 10.1016/j.orgel.2012.12.034.
- [89] Iulia Salaoru, Salah Maswoud, and Shashi Paul. Inkjet printing of functional electronic memory cells: a step forward to green electronics. *Micromachines*, 10(6), 2019. doi: 10.3390/mi10060417.
- [90] Hongrong Hu, Alexander Scholz, Surya Abhishek Singaraju, Yushu Tang, Gabriel Cadilha Marques, and Jasmin Aghassi-Hagmann. Inkjet-printed bipolar resistive switching device based on ag/zno/au structure. *Applied Physics Letters*, 119, 9 2021. doi: 10.1063/5.0058526.

- [91] Mikko Nelo, Marcin Sloma, Jaakko Kelloniemi, Jarkko Puustinen, Teuvo Saikkonen, Jari Juuti, Juha Hä Kkinen, Malgorzata Jakubowska, and Heli Jantunen. Inkjet-printed memristor: Printing process development. *Japanese Journal of Applied Physics*, 2013. doi: 10.7567/JJAP.52.05DB21.
- [92] Georgii A. Illarionov, Denis S. Kolchanov, Oleg A. Kuchur, Mikhail V. Zhukov, Ekaterina Sergeeva, Vladimir V. Krishtop, Alexandr V. Vinogradov, and Maxim I. Morozov. Inkjet assisted fabrication of planar biocompatible memristors. *RSC Advances*, 9:35998–36004, 11 2019. doi: 10.1039/C9RA08114C.
- [93] Nataša Samardžić, Marijana Mionić, Bojan Dakić, Heinrich Hofmann, Staniša Dautović, and Goran Stojanović. Analysis of quantized electrical characteristics of microscale tio2 ink-jet printed memristor. *IEEE Transactions on Electron Devices*, 62:1898–1904, 6 2015. doi: 10.1109/TED.2015.2421283.
- [94] Brian Derby. Bioprinting: inkjet printing proteins and hybrid cell-containing materials and structures. *Journal of Materials Chemistry*, 18:5717–5721, 11 2008. doi: 10.1039/B807560C.
- [95] Nicolaos Scoutaris, Steven Ross, and Dennis Douroumis. Current trends on medical and pharmaceutical applications of inkjet printing technology. *Pharmaceutical Research* 2016, 33:1799–1816, 5 2016. doi: 10.1007/S11095-016-1931-3.
- [96] Ryan D Boehm, Philip R Miller, Justin Daniels, Shane Stafslie, and Roger J Narayan. Inkjet printing for pharmaceutical applications. *Materials Today*, 17(5):247–252, 2014. doi: 10.1016/j.mattod.2014.04.027.
- [97] MicroFab Technologies. A basic ink-jet setup, . URL <http://microfab.com/a-basic-ink-jet-microdispensing-setup>.
- [98] Yu Feng Liu, Yen Fang Pai, Ming Hsu Tsai, and Weng Sing Hwang. Investigation of driving waveform and resonance pressure in piezoelectric inkjet printing. *Applied Physics A: Materials Science and Processing*, 109:323–329, 11 2012. doi: 10.1007/S00339-012-7099-8/FIGURES/9.
- [99] MicroChemicals. Technietch™aci2 the former gold etchant or au etch. URL https://www.microchemicals.com/products/etching_mixtures/technietchtmaci2gold_etchant.html.
- [100] John W. Essam. Percolation theory. *Reports on Progress in Physics*, 43(7):833–912, 1980. doi: 10.1088/0034-4885/43/7/001.
- [101] Paula C Rodrigues, Gabriel P de Souza, Joaquim D Da Motta Neto, and Leni Akcelrud. Thermal treatment and dynamic mechanical thermal properties of polyaniline. *Polymer*, 43(20):5493–5499, 2002. doi: 10.1016/S0032-3861(02)00401-9.
- [102] George Wypych. *Handbook of Odors in Materials*. William Andrew, 2012. ISBN 9781895198515; 1895198518.

-
- [103] Silvia Battistoni, Alessio Verna, Simone Luigi Marasso, Matteo Cocuzza, and Victor Erokhin. On the interpretation of hysteresis loop for electronic and ionic currents in organic memristive devices. *Physica Status Solidi (A) Applications and Materials Science*, 217, 9 2020. doi: 10.1002/pssa.201900985.
- [104] Huanhuan Wang, Jianyi Lin, and Ze Xiang Shen. Polyaniline (pani) based electrode materials for energy storage and conversion. *Journal of science: Advanced materials and devices*, 1(3):225–255, 2016. doi: 10.1016/j.jsamd.2016.08.001.
- [105] Timothy VP Bliss and Sam F Cooke. Long-term potentiation and long-term depression: a clinical perspective. *Clinics*, 66:3–17, 2011. doi: 10.1590/S1807-59322011001300002.